

Remote Sensing of Suspended Sediment Dynamics in the Arctic Nearshore Zone

Konstantin Paul Klein

Dissertation

Zur Erlangung des akademischen Grades
'doctor rerum naturalium' (Dr. rer. nat.)
in der Wissenschaftsdisziplin 'Fernerkundung'

eingereicht als kumulative Arbeit an der
Mathematisch-Naturwissenschaftlichen Fakultät
der Universität Potsdam

angefertigt am
Alfred-Wegener-Institut
Helmholtz Zentrum für Polar- und Meeresforschung

Potsdam, Februar 2022

Hauptbetreuer: Prof. Dr. Hugues Lantuit

Zweitbetreuerin: Dr. Birgit Heim

GutachterInnen: Prof. Dr. Astrid Bracher, Prof. Simon Bélanger

ABSTRACT

The Arctic nearshore zone plays a key role in the carbon cycle. Organic-rich sediments get eroded off permafrost affected coastlines and can be directly transferred to the nearshore zone. Permafrost in the Arctic stores a high amount of organic matter and is vulnerable to thermo-erosion, which is expected to increase due to climate change. This will likely result in higher sediment loads in nearshore waters and has the potential to alter local ecosystems by limiting light transmission into the water column, thus limiting primary production to the top-most part of it, and increasing nutrient export from coastal erosion. Greater organic matter input could result in the release of greenhouse gases to the atmosphere. Climate change also acts upon the fluvial system, leading to greater discharge to the nearshore zone. It leads to decreasing sea-ice cover as well, which will both increase wave energy and lengthen the open-water season. Yet, knowledge on these processes and the resulting impact on the nearshore zone is scarce, because access to and instrument deployment in the nearshore zone is challenging.

Remote sensing can alleviate these issues in providing rapid data delivery in otherwise non-accessible areas. However, the waters in the Arctic nearshore zone are optically complex, with multiple influencing factors, such as organic rich suspended sediments, colored dissolved organic matter (cDOM), and phytoplankton. The goal of this dissertation was to use remotely sensed imagery to monitor processes related to turbidity caused by suspended sediments in the Arctic nearshore zone. *In-situ* measurements of water-leaving reflectance and surface water turbidity were used to calibrate a semi-empirical algorithm which relates turbidity from satellite imagery. Based on this algorithm and ancillary ocean and climate variables, the mechanisms underpinning nearshore turbidity in the Arctic were identified at a resolution not achieved before.

The calibration of the Arctic Nearshore Turbidity Algorithm (ANTA) was based on *in-situ* measurements from the coastal and inner-shelf waters around Herschel Island Qikiqtaruk (HIQ) in the western Canadian Arctic from the summer seasons 2018 and 2019. It performed better than existing algorithms, developed for global applications, in relating turbidity from remotely sensed imagery. These existing algorithms were lacking validation data from permafrost

affected waters, and were thus not able to reflect the complexity of Arctic nearshore waters. The ANTA has a higher sensitivity towards the lowest turbidity values, which is an asset for identifying sediment pathways in the nearshore zone. Its transferability to areas beyond HIQ was successfully demonstrated using turbidity measurements matching satellite image recordings from Adventfjorden, Svalbard. The ANTA is a powerful tool that provides robust turbidity estimations in a variety of Arctic nearshore environments.

Drivers of nearshore turbidity in the Arctic were analyzed by combining ANTA results from the summer season 2019 from HIQ with ocean and climate variables obtained from the weather station at HIQ, the ERA5 reanalysis database, and the Mackenzie River discharge. ERA5 reanalysis data were obtained as domain averages over the Canadian Beaufort Shelf. Nearshore turbidity was linearly correlated to wind speed, significant wave height and wave period. Interestingly, nearshore turbidity was only correlated to wind speed at the shelf, but not to the *in-situ* measurements from the weather station at HIQ. This shows that nearshore turbidity, albeit being of limited spatial extent, gets influenced by the weather conditions multiple kilometers away, rather than in its direct vicinity. The large influence of wave energy on nearshore turbidity indicates that freshly eroded material off the coast is a major contributor to the nearshore sediment load. This contrasts results from the temperate and tropical oceans, where tides and currents are the major drivers of nearshore turbidity. The Mackenzie River discharge was not identified as a driver of nearshore turbidity in 2019, however, the analysis of 30 years of Landsat archive imagery from 1986 to 2016 suggests a direct link between the prevailing wind direction, which heavily influences the Mackenzie River plume extent, and nearshore turbidity around HIQ. This discrepancy could be caused by the abnormal discharge behavior of the Mackenzie River in 2019.

This dissertation has substantially advanced the understanding of suspended sediment processes in the Arctic nearshore zone and provided new monitoring tools for future studies. The presented results will help to understand the role of the Arctic nearshore zone in the carbon cycle under a changing climate.

ZUSAMMENFASSUNG

Der arktische Nahküstenbereich spielt eine wichtige Rolle im Kohlenstoffkreislauf. Küsten, die Permafrostböden aufweisen, sind sehr anfällig für Thermoerosion, wodurch Sediment und unzersetzte, organische Überreste in den Arktischen Ozean gelangen können. Durch den Klimawandel ist davon auszugehen, dass Thermoerosion in Zukunft größere Erosionsraten hervorrufen wird. Permafrostböden enthalten große Mengen organischer Überreste, die nach dem Auftauen von Mikroorganismen zersetzt werden, wodurch Treibhausgase in die Atmosphäre gelangen können. Erhöhte Sedimentmengen in den Küstengewässern verhindert außerdem das Eindringen elektromagnetischer Strahlung in die Wassersäule, wodurch die auf Photosynthese basierte Primärproduktion in tieferen Wasserschichten stark reduziert wird. Durch den Klimawandel transportieren Flüsse in der Arktis mehr Frischwasser und Sediment in die Nahküstenbereiche, und erhöhte Temperaturen verringern die Meereisausdehnung. All diese Prozesse können das Ökosystem des arktischen Nahküstenbereiches nachhaltig verändern, allerdings ist das Verständnis von Interaktionen untereinander und deren Resultate begrenzt, da sich die Datensammlung in arktischen Nahküstenbereichen sehr herausfordernd gestaltet.

Fernerkundungsmethoden bieten die Möglichkeit der vergleichsweise unkomplizierten Datenaufnahme nur schwer erreichbarer Regionen wie dem arktischen Nahküstenbereich. Arktische Küstengewässer sind allerdings optisch komplex, und Wasserinhaltsstoffe wie Sediment, organische Überreste, gelöstes Material und Plankton erschweren genaue Analysen. Das Ziel dieser Dissertation ist es, Satellitenbilder zu analysieren und Sedimentdynamiken zu identifizieren, die die Wassertrübung beeinflussen. In einem empirischen Algorithmus wird die von der Wasseroberfläche reflektierte elektromagnetische Strahlung genutzt, um die Wassertrübung zu berechnen. Zusammen mit einer Sammlung von Wetterdaten und anderen Umwelteinflüssen wurden Mechanismen identifiziert, die die Wassertrübung arktischer Küstengewässer beeinflussen.

Die Kalibrierung des Algorithmus zur Berechnung der Wassertrübung (ANTA) wurde mit Messungen aus den Küstengewässern in der Nähe von Herschel Island Qikiqtaruk (HIQ) auf dem Kanadischen Beaufortschelf durchgeführt. Seine Anwendung führt verglichen mit bereits

existierenden Algorithmen zu besseren Ergebnissen, die für den weltweiten Gebrauch vorgesehen sind. Für die Kalibrierung dieser Algorithmen wurden keine Messungen arktischer Nahküstenbereiche genutzt, wodurch die optische Komplexität nur unzureichend wiedergegeben werden kann. Der ANTA ist besser geeignet, um Transportwege von Sediment an der Wasseroberfläche zu identifizieren, weil nahezu klare Gewässer mit höherer Genauigkeit klassifiziert werden. Messungen aus dem Adventfjord in Spitzbergen zeigen, dass der ANTA auch außerhalb der Kanadischen Beaufortsee akkurate Ergebnisse produziert, was ihn zu einem wichtigen Werkzeug zukünftiger Untersuchungen arktischer Nahküstenbereiche macht.

Um Prozesse zu identifizieren, die die Wassertrübung in arktischen Küstengewässern beeinflussen, wurden ANTA-Ergebnisse aus dem Sommer 2019 von HIQ, Messungen der Wetterstation auf HIQ, Wetter- und Klimamodellierungen des Kanadischen Beaufortschelfes und Abflussdaten des Mackenzie genutzt. Die Wassertrübung korreliert linear mit der Windgeschwindigkeit, der Wellenhöhe und der Wellenperiodendauer. Es ist beachtenswert, dass die Wassertrübung nur mit der Windgeschwindigkeit auf dem Beaufortschelf, nicht aber mit der Windgeschwindigkeit auf HIQ korreliert. Dies zeigt, dass weit entfernte Prozesse großen Einfluss auf die Wassertrübung in arktischen Küstengewässern haben können, obwohl die Wassertrübung selber nur ein kleines Gebiet beeinflusst. Der große Einfluss von Wellenenergie auf die Wassertrübung unterstreicht sowohl die Wirksamkeit von Erosion als auch, dass kürzlich erodiertes Sediment einen erheblichen Anteil der Sedimentfracht im Nahküstenbereich ausmacht. Dies unterscheidet den Arktischen Ozean von den gemäßigten und tropischen Ozeanen, wo Gezeiten und Strömungen die größten Einflüsse auf die Wassertrübung im Nahküstenbereich sind. Die vom Mackenzie transportierten Sedimente haben keinen Einfluss auf die Wassertrübung um HIQ im Sommer 2019, allerdings zeigt die Analyse des dreißigjährigen Bildarchives der Landsat-Satelliten, dass die Windrichtung, welche maßgeblichen Einfluss auf die Verteilung der transportierten Sedimente nimmt, ein wichtiger Faktor sein kann. Diese Diskrepanz könnte jedoch auch dem untypischen Abflussverhalten des Mackenzie im Jahr 2019 geschuldet sein.

Diese Dissertation hat maßgeblichen Anteil am derzeitigen Verständnis der Prozesse im dynamischen Nahküstenbereich des Arktischen Ozeans. Die vorgestellten Methoden und

erlangten Ergebnisse werden helfen, in zukünftigen Studien die Rolle des arktischen Nahküstenbereiches im Kohlenstoffkreislauf zu analysieren und quantifizieren.

ALLGEMEINVERSTÄNDLICHE ZUSAMMENFASSUNG

Die arktischen Küstengewässer spielen eine wichtige Rolle im Zuge der Klimaerwärmung, allerdings wissen wir noch nicht, wie groß diese Rolle wirklich ist. In Küstengewässern treffen Land und Ozean aufeinander, und die daraus resultierenden Wechselwirkungen sind komplex. Warmes Ozeanwasser beschleunigt bei Kontakt das Abtauen der dauerhaft gefrorenen Permafrostböden, die dadurch destabilisiert werden und schließlich durch Wellen abgetragen werden können. Durch diesen Prozess, Erosion genannt, gelangen nicht nur große Mengen Sediment (Bestandteile der abgetragenen Küste) in die Küstengewässer, sondern auch abgestorbene Pflanzenüberreste, die im Dauerfrost nicht zersetzt werden konnten. Nach dem Abtauen beginnen Mikroorganismen mit der Zersetzung, wodurch Treibhausgase entstehen können, die das Klima weiter erwärmen.

Das menschliche Auge ist in der Lage, die Farbe von Wasser zu erkennen und unser Gehirn kann daraus Rückschlüsse zur Wasserqualität ziehen. So gilt gelblich-braunes Wasser allgemein als dreckig, was nichts anderes bedeutet, als dass sich eine große Menge Sediment im Wasser befindet. Als Wissenschaftler wollen wir aber nicht nur wissen, ob Wasser dreckig ist, sondern wie dreckig es ist. Dafür haben wir Berechnungen entwickelt, die uns die Sedimentmenge im Wasser errechnet, sofern wir die Farbe des Wassers kennen. Basis dieser Berechnungen sind Messungen, die einmalig im arktischen Küstenbereich durchgeführt wurden, und jetzt dauerhaft genutzt werden können.

Satellitenbilder, die z.B. auch für Navigationsdienste wie Google Maps genutzt werden, erlauben uns, die Wasserfarbe in deutlich größeren Bereichen zu analysieren. Satellitenbilder haben außerdem den Vorteil, dass Wissenschaftler nicht in entlegene Bereiche wie den arktischen Nahküstenbereich reisen müssen, um die Wasserfarbe zu messen. Satelliten sind dagegen in der Lage, regelmäßig in kurzen Abständen Aufnahmen desselben Gebiets zu machen, welche analysiert werden können. Die oben erwähnten Berechnungen können auch mit Satellitenbildern durchgeführt werden, und sind die bislang genauesten ihrer Art. Wir konnten außerdem feststellen, dass durch Erosion abgetragenes Material einen beachtlichen Anteil an der Sedimentmenge in arktischen Küstengewässern ausmacht. Dadurch könnten größere

Mengen Treibhausgase in die Atmosphäre gelangen, was wiederum das Klima erwärm und die Erosion beschleunigen würde.

TABLE OF CONTENTS

Abstract	i
Zusammenfassung	iii
Allgemeinverständliche Zusammenfassung	vii
Table of Contents	ix
List of Figures	xii
List of Tables	xv
Funding	xvi
Chapter 1 Introduction	1
1.1 Scientific Background	1
1.1.1 Arctic Climate Change	1
1.1.2 The Arctic Nearshore Zone	2
1.1.3 Ocean Color Remote Sensing	4
1.2 Objectives	6
1.3 Study Area	6
1.4 Methods	7
1.4.1 Field Sampling	7
1.4.2 Data Processing	8
1.4.3 Satellite Imagery Processing	9
1.5 Thesis Structure	9
1.6 Author Contributions	10
Chapter 2 Long-Term High-Resolution Sediment and Sea Surface Temperature Spatial Patterns in Arctic Nearshore Waters retrieved using 30-year Landsat Archive Imagery	13
2.1 Abstract	13
2.2 Introduction	14

2.3	Material and Methods	16
2.3.1	Regional Setting	16
2.3.2	Landsat Images Acquisition and Processing	19
2.3.3	Landsat Turbidity Retrieval	24
2.3.4	Transects in the nearshore zone	24
2.3.5	Wind Data	26
2.4	Results	26
2.4.1	Brightness Temperature	26
2.4.2	Surface Reflectance and Turbidity Mapping	28
2.4.3	Gradients in the nearshore zone	31
2.5	Discussion	34
2.6	Conclusion	38
	Appendix A	40

Chapter 3	The Arctic Nearshore Turbidity Algorithm (ANTA) - A Multi Sensor Turbidity Algorithm for Arctic Nearshore Environments	43
3.1	Abstract	43
3.2	Introduction	43
3.3	Methods	46
3.3.1	Regional setting	46
3.3.2	<i>In-situ</i> sampling	48
3.3.3	Optical data processing	49
3.3.4	Algorithm tuning	51
3.3.5	Satellite imagery processing	51
3.4	Results and Discussion	53
3.4.1	Turbidity and SPM	53
3.4.2	ANTA performance	54
3.4.3	Comparison with the Dogliotti et al., (2015) algorithm	57
3.4.4	Test and transfer of the ANTA	60
3.5	Conclusion	62

Chapter 4 Drivers of Turbidity and its Seasonal Variability in the Nearshore Zone of Herschel Island Qikiqtaruk (western Canadian Arctic)	65
4.1 Abstract	65
4.2 Introduction	66
4.3 Methods	68
4.3.1 Study Area	68
4.3.2 Satellite Imagery	68
4.3.3 In-situ data	69
4.3.4 Reanalysis data	70
4.4 Results and Discussion	70
4.4.1 Time Series Analysis	70
4.4.2 Drivers of turbidity	75
4.5 Conclusion	77
Chapter 5 Synthesis	79
5.1 Applicability of Remote Sensing Algorithms in the Arctic Nearshore Zone	80
5.2 Drivers of Nearshore Turbidity	81
5.3 Spatial Variations of Nearshore Turbidity	83
5.4 Challenges and Outlook	84
List of Acronyms	i
Bibliography	iii
Danksagung	xv
Eidesstattliche Erklärung	xvii

LIST OF FIGURES

- Figure 1-1 Effects of thawing and erosion of permafrost on Arctic nearshore zones. Sediments are supplied to the nearshore zone by rivers or coastal erosion, where they can be transferred to greenhouse gases, kept in suspension by waves and currents, exported offshore, or deposited at the seafloor. Adapted, after Fritz et al., 2017. _____ 3
- Figure 1-2 High turbidity in the nearshore zone caused by different drivers. (a) High turbidity caused by longshore drift. The red arrow indicates the origin of the suspended sediment from around the island. Photograph taken by Juliane Wolter. (b) Coastal erosion causes sediment supply to nearshore waters. Warm ocean water caused thermo-erosion along the shoreface (red arrow). Photograph taken by Michael Krautblatter. (c) Waves (red arrow) cause resuspension of formerly deposited sediment. Photograph was taken directly at the shoreline by Michael Krautblatter. (d) A retrogressive thaw slump discharges sediment into nearshore waters. Events of high thermo-erosion can cause substantial amounts of sediment being discharged (Weege, 2016). The red arrow indicates a small fan-like feature, where the thaw stream hits the nearshore zone. Photograph taken by Michael Krautblatter. _____ 4
- Figure 1-3 (a) Location of the study area close to the northernmost border of Canada and the USA. (b) Herschel Island Qikiqtaruk, located on the Canadian Beaufort Shelf. Red dots indicate sampling locations during field expeditions 2018 and 2019. The red area marks the study area in chapter 5. _____ 7
- Figure 2-1 Map of the study area. Upper right: Location of the study area (white rectangle) near the northernmost border of Canada and the USA. Main map: Location of the study area in the region of the Yukon Coast, with the Mackenzie Delta in the east, the Yukon Coastal Plain forming the mainland part and HIQ in the west. Bathymetry of the Canadian Beaufort Shelf is indicated by different shades of blue (Federal publications Inc: Nautical charts of the Beaufort Sea, 1998-2016). Upper left: close-up to the study area with indicated geographical locations (Burn and Hattendorf, 2011). A Landsat 5 (TM) true color (band composition 321) image is underlain by a hill-shaded 2 m DEM. _____ 17
- Figure 2-2 Windrose diagram showing wind direction and speed frequency during the sea ice-free period. Data was acquired for 1995 – 2016 from the weather station at Simpson Point, HIQ. Data provided by (Government of Canada, 2018), figure modified after (Radosavljevic et al., 2015). _____ 18
- Figure 2-3 Comparison between RS (red) and RRS (red) data products in coastal and inner shelf waters around HIQ. (a) Landsat TM image recorded on September 12th, 2011, and (b) Landsat OLI image, recorded on August 8th, 2016. _____ 21
- Figure 2-4 Transects in the nearshore zone of HIQ that were used to facilitate the interpretation of gradients of water turbidity, RS (red), and water temperature. The black arrow indicates the starting point and the direction of the alongshore transect. Background image shows a Landsat 5 (TM) true color (band composition 321) image. _____ 25

- Figure 2-5 Mean BT from Landsat thermal infrared channels, for (a) changing wind conditions, (b) steady NW wind conditions and (c) steady ESE wind conditions. Prevailling wind conditions are indicated with arrows in the center of each picture. The number of used scenes per wind condition are listed in Table 2-1. Red areas indicate areas of high BT, white areas indicate land surface areas. Mean BT is highest in (c) and lowest in (b). Bathymetry is indicated by black lines (Federal publications Inc: Nautical charts of the Beaufort Sea, 1998-2016). Note the very cold BT in (c) at the NW coast of HIQ and the large contrast to the SE coast and Workboat Passage. The calculated standard deviation for each image is given in Appendix A. _____ 27
- Figure 2-6 Mean RS (red), that was used as proxy for turbidity, for (a) changing wind conditions, (b) steady NW wind conditions and (c) steady ESE wind conditions. Prevailling wind conditions are indicated with arrows in the center of each picture. The number of used scenes per wind condition are listed in Table 2-1. Red areas indicate areas of high turbidity, white areas indicate land surfaces or areas of failed atmospheric correction. Bathymetry is indicated by black lines (Federal publications Inc: Nautical charts of the Beaufort Sea, 1998-2016). Turbidity is highest in (c) and lowest in (b). Note the similar dispersal patterns in (a) and (b) compared to (c). The calculated standard deviation for each image is given in Appendix A. _____ 29
- Figure 2-7 Mean Landsat retrieved turbidity after (Dogliotti et al., 2015) for (a) changing wind conditions, (b) steady NW wind conditions and (c) steady E wind conditions. Prevailling wind conditions are indicated with arrows in the center of each picture. The number of used scenes per wind condition are listed in Table 2-1. Red areas indicate areas of high turbidity, white areas indicate land surfaces or areas of failed atmospheric correction. Bathymetry is indicated by black lines (Federal publications Inc: Nautical charts of the Beaufort Sea, 1998-2016). Turbidity is highest in (c) and similar in (a) and (b). _____ 30
- Figure 2-8 (a) Comparison between the maximum turbidity and RS (red) values observed along the coast of HIQ. The blue line represents the Dogliotti et al. (2015) (Dogliotti et al., 2015) turbidity model, the green line the corresponding RS (red) value. (b) Correlation between the RS (red) and turbidity values in the nearshore zone. The red line represents the best exponential fitting function. The values were extracted at points along a transect starting at Simpson Point and moving clockwise (Figure 2-4). _____ 31
- Figure 2-9. Transects perpendicular to the coastline of HIQ to quantify the gradients from the nearshore to the offshore. (a) Mean BT during NW wind conditions. (b) Mean BT during ESE wind conditions. (c) Mean RS (red) during NW wind conditions. (d) Mean RS (red) during ESE wind conditions. (e) Mean turbidity during NW wind conditions. (f) Mean turbidity during ESE wind conditions. Different coastal orientations are indicated by different colors. The position of each transect line is displayed in Figure 2-4. _____ 33
- Figure 2-10. Volumetric coastal erosion at HIQ based on DEM elevation changes from 2000-2011 (Obu et al., 2016). _____ 36
- Figure 3-1 (a) Location of the study area on the Canadian Beaufort Shelf, near the northernmost border of Canada and the USA. (b) Close-up to Herschel Island Qikuqtaruk. Sampling transects during the 2019 field campaign are indicated by red dots. _____ 47
- Figure 3-2 (a) Location of Adventfjorden, a small sidearm of the Isfjorden system on the west coast of Svalbard. (b) Close-up of Adventfjorden, with the sampling grid indicated by red dots. _____ 48

Figure 3-3 In-situ measured spectra of water leaving reflectance ($R_{RS}*\pi$) that were used for the calibration of the turbidity algorithm. Spectra were measured using two TriOS Ramses hyperspectral radiometers above the water surface.	50
Figure 3-4 (a) Turbidity and SPM measurements from 2018 and 2019 including error bars and (b) zoom into the lower value range. The turbidity error was assigned to 10 % of the measurement, which is the margin of error of the turbidity meter as provided by the manufacturer. SPM error was calculated as the standard deviation of triplicate samples.	54
Figure 3-5 Application of the ANTA to different satellite data recorded at June 19th, 2019 (table 1): (a) Landsat 8, (b) Sentinel 2A, (c) Sentinel 3A, (d) Sentinel 3B.	56
Figure 3-6 Scatterplot between Landsat 8 and Sentinel 2 derived turbidity. 3000 randomly generated points in the extent of Figures 5 a and b (excluding land areas) were used for the comparison. The regression line is linear ($R^2=0.89$, $y=0.87x + 1.94$) and shows the overestimation of Sentinel 2 derived turbidity below 10 FNU.	57
Figure 3-7 Comparison of the ANTA to the results presented in Klein et al., (2019) applying the Dogliotti et al., (2015) algorithm	59
Figure 3-8 Scatterplot comparing the different turbidity algorithms shown in Figure 7.	60
Figure 3-9 Application of the ANTA to Sentinel 2 imagery in Adventfjorden with in-situ turbidity measurements from the FreshFate sampling plotted in squares	61
Figure 3-10 Scatterplot comparing in-situ turbidity sampled in Adventfjord and Sentinel 2 derived turbidity values (ANTA)	62
Figure 4-1 (a) Location of the study area close to the northernmost border of Canada and the USA. (b) Herschel Island Qikiqtaruk, located on the Canadian Beaufort Shelf. The area of interest is highlighted in red.	69
Figure 4-2 Time series of satellite imagery from the summer season 2019.	71
Figure 4-3 Overview of mean turbidity in the area of interest over the summer season 2019.	73
Figure 4-4 Mean daily temperature from the weather station at HIQ between June 1 and September 30 (red) and daily Mackenzie River discharge measured at Arctic Red Tsiigehtchic for the same time period (blue). Black lines indicate the dates of satellite image recordings.	74
Figure 4-5 Correlation of possible drivers and nearshore turbidity. Parameters which were both measured by the HIQ weather station and downloaded in the ERA5 reanalysis dataset, (H) relates to the HIQ measurement and (R) to the ERA5 reanalysis dataset.	76
Figure 4-6 Rose diagram showing the dependence of nearshore turbidity on wind speed (reanalysis data from the shelf) and wind direction (in-situ data from HIQ).	77

LIST OF TABLES

Table 2-1 List of Landsat scenes used in this study. The data was acquired from the USGS earthexplorer. The wind direction and speed were retrieved from climate data from Environment Canada.. The extraction of wind direction is described in section 2.2. Changing wind direction refers to unsteady wind conditions.	23
Table 3-1 Calibration coefficients A [FNU] and C for multiple operative and historical satellite sensors to be used in their respective red and NIR wavelength spectral bands. Coefficients published by Dogliotti et al., 2015 and Nechad et al., 2016 are given as reference	52
Table 3-2 Specifications of the used satellite imagery	52

FUNDING

This dissertation was funded by a PhD Stipend from the Potsdam Graduate School (PoGS).

A research stay at the Laboratoire d’Oceanographie de Villefranche-sûr-Mer from September 23, 2019, to February 29, 2020, was funded by a short-term stipend from the German Academic Exchange Service (DAAD) under grant number 57438025.

This dissertation was part of the Nunataryuk project. It received funding under the European Union’s Horizon 2020 Research and Innovation Programme under grant agreement no. 773421.

1 INTRODUCTION

1.1 SCIENTIFIC BACKGROUND

1.1.1 Arctic Climate Change

The Arctic is disproportionately strong affected by climate change (Box et al., 2019; Serreze and Barry, 2011). This process is called Arctic amplification and has been, at least in theory, known for more than 100 years (Arrhenius, 1896). The resulting changes observed in the Arctic (areas north of 66 °N) are of global relevance because they feed back to the Earth climate system. Already, the Earth has warmed by roughly 1.1 K by 2021 compared to pre-industrial times (IPCC, 2021), which increases the risk to cross tipping points in the Earth climate system. Tipping points are crucial thresholds which have the ability to change the state of the Earth climate system enduringly. Understanding and studying ongoing changes observed in the Arctic is therefore crucial to the publication of accurate projections of the Earth's climate. These changes include, but are not limited to, glacier and ice sheet retreat, sea ice loss, and permafrost degradation. The focus of this introduction will be on sea ice loss and permafrost degradation because they relate directly to changes in the Arctic nearshore zone.

Sea ice loss in the Arctic has accelerated since 1990 (Walsh et al., 2017). This triggers an albedo feedback, as darker ocean surfaces absorb more energy than lighter ice surfaces (Serreze et al., 2007). The longer open water season in summer, the time of the year where the ocean is not covered by ice, results in higher primary production due to a longer phytoplankton growth season (Arrigo et al., 2008), which has the potential to alter the Arctic ecosystem structure. Decreasing sea ice extent also enhances coastal erosion by increasing fetch lengths and thus incoming wave energy (Solomon, 2005). Modelling approaches indicated that the increased fresh water input to the ocean from melting sea ice has the potential to disturb global thermohaline circulation (Peterson et al., 2006). Traditional hunting practices of indigenous communities are also impacted by sea ice loss, as polar bear health and abundance is reduced (Serreze et al., 2007).

Permafrost is experiencing dramatic degradation in the Arctic. The term permafrost describes a thermal condition of the ground, which stays below temperatures of 0 °C for two consecutive years. Permafrost covers roughly 15 % of the land surface on the northern hemisphere (Obu et al., 2019). It stores large amounts of Carbon (Hugelius et al., 2014), which can be transferred into greenhouse gases upon thawing (Tanski et al., 2019; Vonk et al., 2012), further enhancing climate warming. Permafrost is particularly vulnerable to increasing air temperatures, which can lead to thaw subsidence and/or thermokarst (Van Everdingen, 2005). Along coastlines, permafrost is exposed to thermal erosion caused by warm ocean water during summer (Lantuit and Pollard, 2008; McGillivray et al., 1993), which gets enhanced with reduced sea ice and longer open water periods (Serreze et al., 2007).

1.1.2 The Arctic Nearshore Zone

The nearshore zone is defined as the water area close to the coast shallower than 20 m. It is largely understudied in contrast to the coastal zone and the deeper ocean waters due to the traditional division between terrestrial and marine science (Fritz et al., 2017). Nearshore waters are difficult to access with large research vessels, which are traditionally used in oceanography, and permanent observing stations are rare. This is specifically true for the Arctic, where the ocean is covered with ice most time of the year.

Sediment input to Arctic nearshore and shelf areas rose remarkably during the past decades due to increased river discharge and higher coastal erosion (Ahmed et al., 2020; Jones et al., 2018; McClelland et al., 2006). The freshwater input to the Arctic Ocean rose by 14 % between 1980 and 2009 (Ahmed et al., 2020). The sedimentary export of the Mackenzie River rose by 50 % from 2003 to 2013 (Doxaran et al., 2015). Arctic coasts degrade at a mean annual rate of 0.5 m/a (Lantuit et al., 2013), however, at coasts with high ground ice content, this rate can be exceeded by an order of a magnitude (Cunliffe et al., 2019; Jones et al., 2018) and reach yearly rates of 22 m.

The Arctic nearshore zone plays a crucial role in the carbon cycle. The rising rates of coastal erosion and river discharge lead to a greater input of carbon into the nearshore zone. The carbon is then reworked in the water column because of incoming waves and resuspension (Jong et al., 2020, Figure 1). Deposition of sediment is rare due to wave energy, and storms have the

potential to resuspend formerly deposited material. At the water surface, organic rich sediments can directly be transferred into greenhouse gases (Tanski et al., 2019; Vonk et al., 2012). Sediment delivered to the nearshore zone increases water turbidity and thus light transmission into the water column. This limits primary production (Mangan et al., 2020), impacts local food webs (Dunton et al., 2006) and eventually the subsistence economy of the local population.

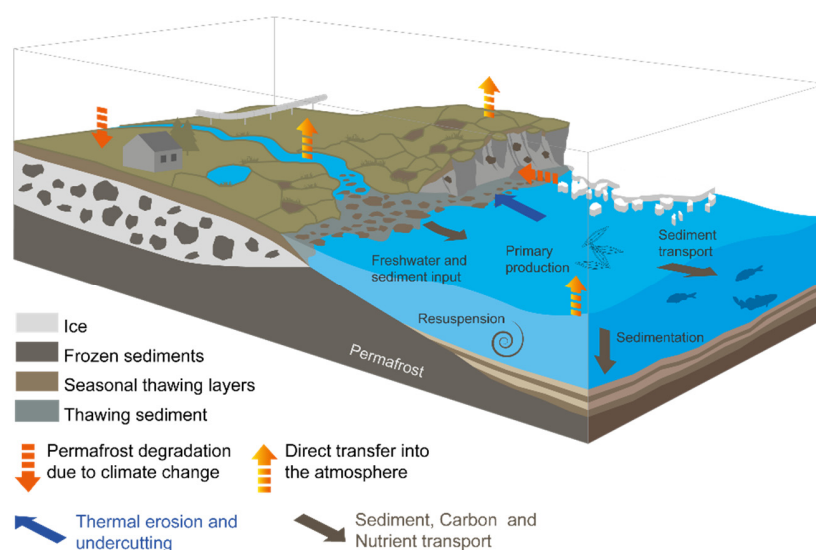


Figure 1-1 Effects of thawing and erosion of permafrost on Arctic nearshore zones. Sediments are supplied to the nearshore zone by rivers or coastal erosion, where they can be transferred to greenhouse gases, kept in suspension by waves and currents, exported offshore, or deposited at the seafloor. Adapted, after Fritz et al., 2017.

While the impacts of increased turbidity in Arctic nearshore waters are well studied, little knowledge exists about the mechanisms underpinning turbidity occurrence (Figure 1-2). They are generally assumed to be similar to the ones in the temperate and tropical ocean, which are tides and wave energy (Cartwright et al., 2021). However, tidal range in the Arctic is considerably lower compared to most other parts of the World's ocean and wave energy is lower than in the open Atlantic or Pacific oceans (Kulikov et al., 2018). In the Arctic other processes, such as the presence of permafrost, greatly contribute to the occurrence of turbidity.

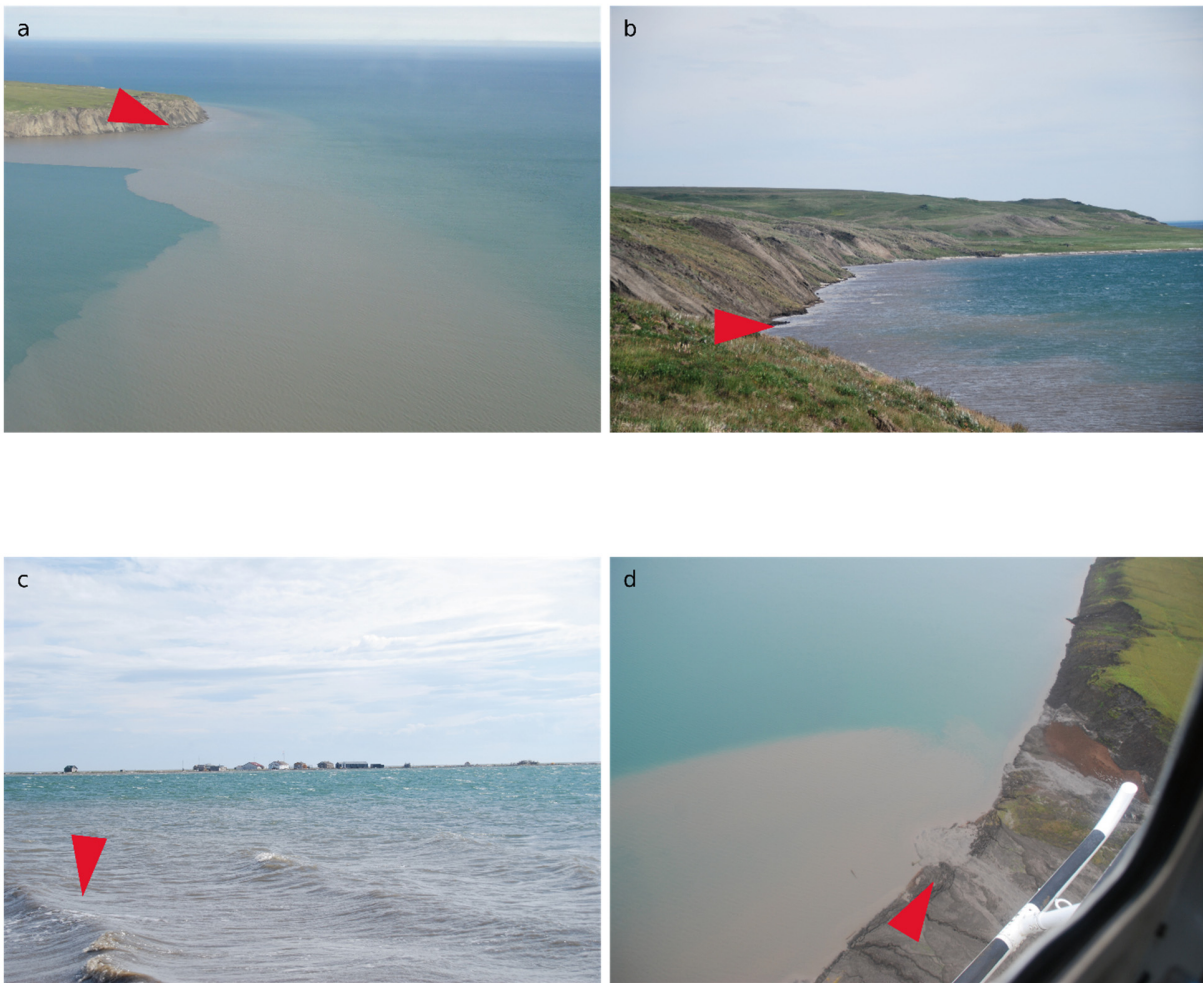


Figure 1-2 High turbidity in the nearshore zone caused by different drivers. (a) High turbidity caused by longshore drift. The red arrow indicates the origin of the suspended sediment from around the island. Photograph taken by Juliane Wolter. (b) Coastal erosion causes sediment supply to nearshore waters. Warm ocean water caused thermo-erosion along the shoreface (red arrow). Photograph taken by Michael Krautblatter. (c) Waves (red arrow) cause resuspension of formerly deposited sediment. Photograph was taken directly at the shoreline by Michael Krautblatter. (d) A retrogressive thaw slump discharges sediment into nearshore waters. Events of high thermo-erosion can cause substantial amounts of sediment being discharged (Weege, 2016). The red arrow indicates a small fan-like feature, where the thaw stream hits the nearshore zone. Photograph taken by Michael Krautblatter.

1.1.3 Ocean Color Remote Sensing

Remote sensing describes the detection of physical phenomena from a distance usually related to the reflection or emission of radiance. Thus, it is a powerful tool to gather scientific data

without the need of personal attendance at the sampling location. This is especially useful in remote areas such as the Arctic. Remote sensing has the capability to cover large areas, significantly enhancing the spatial resolution of most *in-situ* measurements. Remote sensing techniques cover a wide range of spatial, spectral, and temporal resolutions, including terrestrial, airborne, and spaceborne platforms. Remote sensing is still considered to be a relatively new science division, even though it has been successfully used since the middle of the 20th century.

Ocean color remote sensing utilizes air- and spaceborne platforms, and sensors which are able to detect electromagnetic radiation reflected at the water surface. This gets significantly limited by the spectral properties of water, which absorbs most radiation in near-infrared (NIR) and longer wavelengths. This means that reflected radiation in these wavelengths is completely caused by in-water constituents. This knowledge has been used to relate reflected radiation from the water surface to multiple in-water constituents in the past decades, such as chlorophyll-a concentration, or water turbidity.

Turbidity caused by suspended sediments is well correlated to the reflectance in the red and NIR part of the electromagnetic spectrum (Munday and Alföldi, 1979). Reflectance in the red part of the spectra is better correlated to lower suspended sediment concentrations, but saturates with increasing concentrations. On the other hand, the NIR reflectance is noisy over clear water, but accurate at higher suspended sediment concentrations. Retrieving turbidity from remotely sensed imagery drastically improved with the introduction of semi-empirical relationships (Nechad et al., 2009). A frequently used turbidity algorithm was published by Dogliotti et al., 2015, which uses a switching algorithm of red and NIR calculated turbidity to account for different turbidity ranges. Validation data from multiple estuarine environments, located in Europe and South America were used to calibrate the algorithm and make it a versatile instrument to resolve turbidity in coastal waters. Yet, permafrost affected nearshore waters are characterized by very high turbidity values and were not considered in the development of these algorithms, even though they represent one third of the world's coastlines (Lantuit et al., 2013).

1.2 OBJECTIVES

This dissertation aims to fill the gap outlined above by fostering the understanding of suspended sediment dynamics in the Arctic nearshore zone using remotely sensed imagery. The specific objectives are as follows:

1. Recalibrating existing turbidity algorithms, which relate the water leaving reflectance to surface water turbidity, to the optically complex waters in the Arctic nearshore zone.
2. Identifying drivers of nearshore turbidity over a whole summer season and its intra-seasonal variability.

1.3 STUDY AREA

Little research has been conducted in Arctic nearshore zones, and radiometric measurements are particularly scarce. To fill this gap and provide new validation data for remote sensing, most work for this dissertation was conducted in the coastal and innershelf waters of the Canadian Beaufort Shelf around Herschel Island Qikiqtaruk (HIQ, 69.4 °N, 139.1 °W, Figure 1-3) in the western Canadian Arctic. The area presents several advantages for the study of coastal turbidity and the retrieval of data in the nearshore zone: It is close to the Mackenzie River and its large sediment plume, it also features many coastal erosion features related to the presence of permafrost and it is fairly accessible in terms of logistics.

The Mackenzie River is the main freshwater source of the Canadian Beaufort Shelf, with a peak discharge of 35 000 m³/s during its freshet in May (O'Brien et al., 2006; Yang et al., 2015). It drains an area of ~1.8 million km², 75 % of which are affected by permafrost, and discharges around 325 km³ per year into the Arctic Ocean. Permafrost along the Canadian Yukon Coast has high ice content, which occupies 46 % of the ground volume (Mackay, 1971), making it especially vulnerable to thermo-erosion. Coastal erosion occurs only during the open water season, which typically spans from mid-June to early September (Solomon, 2005). The average coastal retreat rate is 0.68 m/a (Obu et al., 2016) and is thus higher than on average in the Arctic. Extreme events, however, can cause annual erosion rates of 15 m/a (Cunliffe et al., 2019; Lim et al., 2020).

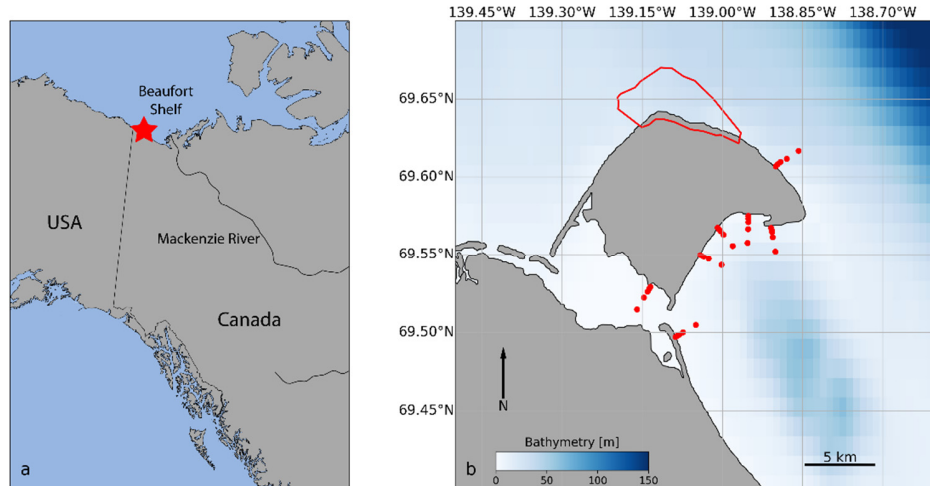


Figure 1-3 (a) Location of the study area close to the northernmost border of Canada and the USA. (b) Herschel Island Qikiqtaruk, located on the Canadian Beaufort Shelf. Red dots indicate sampling locations during field expeditions 2018 and 2019. The red area marks the study area in chapter 5.

The climate in the southern Beaufort Sea is characterized by long, cold winters, and short summers. The average annual temperature is $-8.4\text{ }^{\circ}\text{C}$ (Coch et al., 2018). The predominant wind directions are ESE and NW (Hill et al., 1991; Radosavljevic et al., 2015), with NW being the main storm direction in late summer and fall. During ESE wind conditions, the Mackenzie River can be distributed over large parts of the Canadian Beaufort Shelf, potentially reaching the nearshore zone of HIQ approximately 120 km west of the delta. Wind forcing further influences hydrodynamics such as currents (Hill et al., 1991) and upwelling (Williams et al., 2006).

1.4 METHODS

1.4.1 Field Sampling

Field sampling was conducted in the nearshore zone of HIQ during summer seasons 2018 and 2019. Water turbidity and suspended particulate matter (SPM) concentration were sampled during both campaigns. Water leaving reflectance was only measured during the 2019 campaign. Samples were taken in transects perpendicular to the coastline. 5 samples were taken per transect in distances of 50 m, 250 m, 500 m, 1000 m, and 2000 m to the coastline,

respectively. Transects were chosen in front of different morphological features of the coast to capture a wide variety of influences, including creeks and retrogressive thaw slumps discharging into the nearshore waters, eroding permafrost cliffs, and lagoons.

Water turbidity was sampled using a Hach 2100Qis turbiditymeter. Samples were taken at each sampling location off a Zodiac MKV HD coastal ship in pre-rinsed 10 ml glass vials at 5 cm water depth. Duplicates were sampled at each location and averaged. To retrieve SPM concentration, water samples were taken in pre-rinsed 1L Nalgene bottles and filtered in field camp through pre-weighed Whatman GF-F glass-microfiber filters right after the sampling. Back in the lab, filters were dried at 50°C for 5 days prior to re-weighing. Sediment mass was corrected for salt remnants based on the results presented in Neukermans et al., 2012. To calculate SPM concentration, sediment mass was divided by the volume of filtered sea-water. Triplicates were sampled at each location and averaged.

Water leaving reflectance (R_w) was measured using two separate TriOS RAMSES radiometers, on of each measuring irradiance (E , [$W/(m^2)$]) and radiance (L , [$W/(m^2*sr)$]) in the spectral range of 350-950 nm at a spectral resolution of 4 nm. Each measurement lasted for 5 minutes. Down-welling sky-irradiance was measured at the top-most location of the coastal ship for the whole 5 minutes. Radiance was measured as total upwelling (L_U) and sky radiance (L_D), respectively, for 2 minutes each, one after another. Radiance measures were conducted in 135 ° relative to the solar zenith angle and in nadir/zenith angles of 40 ° (Mobley, 1999).

1.4.2 Data Processing

Radiometric data were processed according to Ruddick et al., 2006. In short, measurements were not used for further analysis if (i) the inclination in either x or y direction was larger than 5°; or (ii) either L_D , L_U , or E_D differed by more than 25% to its neighboring scan; or (iii) the spectra were incomplete due to sensor malfunction. In total, quality requirements were met by measurements from 32 sampling locations. The first five consecutive instances of L_D , L_U , E_D were used to calculate remote sensing reflectance (R_{RS}) and R_w ($R_{RS}*\pi$) according to Mobley, 1999:

$$R_{RS} = (L_U - \rho * L_D)/E_D \quad (1)$$

The ρ value represents sky radiance reflectance and was set according to Mobley, 1999. A baseline correction as proposed in Knaeps et al., 2015 was conducted for measurements corresponding to turbidity measurements below 10 FNU by assuming the reflectance above 900 nm being zero (Jain and Singh, 2003) and using it as baseline. The five individual instances of R_{RS} were used to calculate means, medians, and standard deviations, before relating R_{RS} to R_w .

1.4.3 Satellite Imagery Processing

For this dissertation, satellite imagery recorded by Landsat 4/5 TM, Landsat 7 ETM+, Landsat 8 OLI, Sentinel 2 MSI, and Sentinel 3 OLCI were used. Landsat imagery was downloaded from the United States Geological Survey (USGS) Earth Explorer as Level 1T product (i.e. with georeferencing but without atmospheric correction). Sentinel imagery was downloaded from the European Space Agency (ESA) Copernicus Hub as Level 1C product, which is comparable to the USGS Level 1T product. Atmospheric correction towards R_w was performed using the ACOLITE software (Vanhellemont, 2019; Vanhellemont and Ruddick, 2021, 2018).

1.5 THESIS STRUCTURE

This cumulative dissertation includes an introduction (chapter 1), three original research papers, which are either published or are under review in international peer-reviewed journals (chapters 2, 3, and 4), and a synthesis of the results (chapter 5).

The study presented in chapter 2 investigates the potential of the Landsat long-term archive to resolve turbidity and sea surface temperature under seasonal changing wind conditions. It combines a well-established turbidity algorithm (Dogliotti et al., 2015) with regional wind data from HIQ in the western Canadian Arctic. This study demonstrates that the data extracted from the algorithm provide reasonable results but are not fully capable to resolve turbidity in complex Arctic nearshore environments. Based on this finding, the study presented in chapter 3 aims at introducing a new algorithm based on the one provided by Dogliotti et al. (2015) using field data collected in the nearshore zone of HIQ. Turbidity samples and imagery from another Arctic location (Adventfjorden, Svalbard) were used to demonstrate the transferability to Arctic nearshore zones beyond HIQ. The study in chapter 4 investigates drivers of nearshore turbidity

around HIQ and its intraseasonal variability. A time series of high-resolution satellite imagery from the summer season 2019 coupled with ocean and climate variables from a weather station on HIQ and the ERA5 reanalysis dataset, as well as the Mackenzie River discharge, were used to resolve fine scale dynamics and discriminate processes responsible for turbidity variability.

Chapter 2

Klein, K.P., Lantuit, H., Heim, B., Fell, F., Doxaran, D., Irrgang, A.M., 2019. Long-term high-resolution sediment and sea surface temperature spatial patterns in Arctic nearshore waters retrieved using 30-year Landsat archive imagery. *Remote Sens.* 11. <https://doi.org/10.3390/rs11232791>

Chapter 3

Klein, K.P., Lantuit, H., Heim, B., Doxaran, D., Juhls, B., Nitze, I., Walch, D., Poste, A., Søreide, J.E., 2021. The Arctic Nearshore Turbidity Algorithm (ANTA) - A multi sensor turbidity algorithm for Arctic nearshore environments. *Sci. Remote Sens.* 4. <https://doi.org/10.1016/j.srs.2021.100036>

Supplementary data for this publication is available online.

<https://doi.org/10.1016/j.srs.2021.100036>

Chapter 4

Klein, K.P., Lantuit, H., Rolph, R.J., 2022. Drivers of Turbidity and its Seasonal Variability in the Nearshore Zone of Herschel Island Qikiqtaruk (western Canadian Arctic). Manuscript under review in *MDPI Water* (Manuscript ID: water-1605625)

1.6 AUTHOR CONTRIBUTIONS

Chapter 2

Study design: **KPK**, HL, BH, FF; Data Acquisition: **KPK**, BH; Imagery Processing: **KPK**, BH, DD, FF; Interpretation of results: **KPK**, AMI, HL; Manuscript preparation: **KPK**, AMI.

Chapter 3

Study design: **KPK**, HL, BH; Field work HIQ: **KPK**; Data processing: **KPK**, DD; Algorithm development: **KPK**, DD, BJ, IN, Field work Adventfjorden: AP, JES, DW; Interpretation of results: **KPK**, HL, BH, AP; Manuscript preparation: **KPK**, BJ, AP.

Chapter 4

Study design: **KPK**, HL; Data acquisition: **KPK**, RJR; Data processing: **KPK**, RJR; Statistical analysis: **KPK**; Interpretation of results: **KPK**, HL; manuscript preparation: **KPK**.

2 LONG-TERM HIGH-RESOLUTION SEDIMENT AND SEA SURFACE TEMPERATURE SPATIAL PATTERNS IN ARCTIC NEARSHORE WATERS RETRIEVED USING 30-YEAR LANDSAT ARCHIVE IMAGERY

2.1 ABSTRACT

The Arctic is directly impacted by climate change. The increase in air temperature drives the thawing of permafrost and an increase in coastal erosion and river discharge. This leads to a greater input of sediment and organic matter into coastal waters, which substantially impacts ecosystems, the subsistence economy of the local population, and the climate due to the transformation of organic matter into greenhouse gases. Yet, the patterns of sediment dispersal in the nearshore zone are not well known, because ships do not often reach shallow waters and satellite remote sensing is traditionally focused on less dynamic environments. We use the extensive Landsat archive to investigate sediment dispersal patterns specifically on an exemplary Arctic nearshore environment, where field measurements are often scarce. Multiple Landsat scenes were combined to calculate means of sediment dispersal and sea surface temperature under changing seasonal wind conditions in the nearshore zone of Herschel Island Qikiqtaruk in the western Canadian Arctic since 1982. We use observations in the Landsat red and thermal wavebands, as well as a recently published water turbidity algorithm to relate archive wind data to turbidity and sea surface temperature. We map the spatial patterns of turbidity and water temperature at high spatial resolution in order to resolve transport pathways of water and sediment at the water surface. Our results show that these pathways are clearly related to the prevailing wind conditions, being ESE and NW. During easterly wind conditions, both turbidity and water temperature are significantly higher in the nearshore area. The extent of the Mackenzie River plume and coastal erosion are the main explanatory variables for sediment dispersal and sea surface temperature distributions in the study area. During

northwesterly wind conditions, the influence of the Mackenzie River plume is negligible. Our results highlight the potential of high spatial resolution Landsat imagery to detect small-scale hydrodynamic processes, but also show the need to specifically tune optical models for Arctic nearshore environments.

2.2 INTRODUCTION

Climate change is stronger in the Arctic than anywhere else on Earth (IPCC, 2013). It leads to multiple impacts on the biophysical system, including intensified permafrost thaw, increasing river discharge and stronger coastal erosion. This, in turn has the potential to mobilize large carbon pools stored in permafrost (Hugelius et al., 2014), to release greenhouse gases, such as carbon dioxide (CO_2) and methane (H_4) to the atmosphere (Romanovsky et al., 2010; Vonk et al., 2012) and to release carbon and nutrients directly into the nearshore zone (Fritz et al., 2017).

Due to enhanced coastal erosion and increased discharge from rivers, sedimentary inputs to the Arctic nearshore zone and shelf areas rose remarkably in the second half of the 20th century (Déry et al., 2009; Jones et al., 2009; McClelland et al., 2006). The annual discharge of the Mackenzie River rose by 22 % together with an increase of particulate export of 46 % from 2003 to 2015 (Doxaran et al., 2015; Yang et al., 2015). Arctic coasts are also actively eroding leading to an enhanced input of sediment (Lantuit et al., 2013). The mean annual rate of shoreline erosion of Arctic coasts is 0.5 m/a (Lantuit et al., 2012). Higher values up to 10 m/a occur at coasts with high ice content, near deltas of large rivers entering the Arctic Ocean (Mackenzie, Lena, Yenisei, Ob, Kolyma) (Lantuit et al., 2012).

Arctic nearshore zones, defined as areas shallower than 20 m, remain under-represented in Arctic oceanography, even though their proportion to the Arctic Ocean surface area is around five times larger compared to the rest of the world's nearshore area to the world's ocean (~7.5 % compared to ~1.5 %, (Fritz et al., 2017)). This is due to the remote location of the Arctic coasts, the dynamic nature of these environments and the challenging conditions for *in-situ* sensor deployment. However, the nearshore zone plays a crucial role in Arctic biogeochemical cycling and sometimes for local economy. Most of the sediment derived from erosion of coastal

permafrost settles in the nearshore zone or gets directly transferred into greenhouse gases (Fritz et al., 2017; Tanski et al., 2019).

Arctic shelves are the main locus of primary production (Arrigo et al., 2008), which is highly dependent on solar light penetration within the water column and thus sensitive to variations of water turbidity (Carmack and Wassmann, 2006). Fresh water input to Arctic shelves is for instance necessary for several species of amphidromous fishes that are central to the subsistence economy of indigenous communities (Carmack and Wassmann, 2006; Dunton et al., 2006). Yet, the exact patterns of sediment dispersal in the Arctic nearshore zone are not well known and shore-specific processes such as longshore drift or barrier island formation are often not captured by existing datasets.

Remote sensing observations have the potential to overcome these challenges and, at least partly, to monitor variations in sediment release associated with changing climate conditions. Yet, satellite sensors are limited either in spatial or temporal resolution, which means that higher temporal resolution is associated with coarser spatial resolution and *vice versa* (Hilker et al., 2009). So far, remote sensing of suspended sediments and organic matter (mainly phytoplankton) in seawater has been based on rather coarse (> 250 m) resolution sensors (e.g. SeaWiFs Sea-viewing Wide Field-of-view Sensor, MODIS Moderate-resolution Imaging Spectroradiometer, MERIS Medium Resolution Imaging Spectrometer), which cannot resolve shore-specific fine-scale processes (Vanhellemont and Ruddick, 2014). High spatial resolution sensors onboard Landsat (30m) and Sentinel 2 (10m) satellite platforms can potentially resolve these processes (Ritchie et al., 1990; Vanhellemont and Ruddick, 2015, 2014). The extensive Landsat archive, which contains spatially consistent data since 1982, can help to detect multi-year surface changes. Its high spatial resolution is also an asset to resolve small-scale surface current processes in the nearshore zone. However, as Landsat sensors were originally designed for land surface applications, the retrieval of suspended sediment information has been subject to many challenges (Doerffer et al., 1989).

In this study, we explore the potential of a new technique where multiple Landsat scenes are stacked to calculate ‘mean’ images for a thirty-year period. These images resolve turbidity and water temperature dispersal patterns at high spatial resolution in the nearshore zone. We applied

this technique in a study area around Herschel Island Qikiqtaruk, further on referred to as HIQ, in the western Canadian Arctic under seasonal changing wind conditions. HIQ was selected as a study site because it is impacted by large rates of coastal erosion (Obu et al., 2016) and is located in close vicinity to the Mackenzie River plume on the Canadian Beaufort Shelf (Doxaran et al., 2012). This allows us to map sediment dispersal and water temperature spatial patterns related to coastal erosion and freshwater input. The specific objectives are: (i) to characterize small-scale nearshore turbidity and water temperature dynamics and (ii) to identify areas where sediment and organic matter accumulate under the two prevailing wind conditions in the southern Beaufort Sea (ESE and NW). Landsat imagery from 1982 to 2016 was analyzed for that. We hypothesize that, depending on the wind direction, the nearshore zone of HIQ experiences very limited sediment and freshwater input from the Mackenzie Delta, despite its geographical vicinity.

2.3 MATERIAL AND METHODS

2.3.1 Regional Setting

The focus of this study is on the Beaufort Sea inner shelf waters around HIQ (69°36' N; 139°04' W, Figure 2-1). The study area was chosen because of its close proximity to the Mackenzie Delta, the presence of a strongly eroding coast (Couture et al., 2018; Lantuit and Pollard, 2008; Obu et al., 2016) and changing hydrodynamics of the Mackenzie River outflow (Yang et al., 2015). HIQ is located on the Canadian Beaufort Shelf, which covers less than 2 % of the Arctic coast shelf area (~64 000 km²) and which is narrow (~ 100 km) compared to the Eurasian shelves (O'Brien et al., 2006; Stein and MacDonald, 2014). The shelf has a gentle relief up to approximately 80 m water depth, where the shelf break is located. Notable exceptions are the Mackenzie Trough, an up to 300 m deep glacial valley located north east of HIQ, and several smaller underwater valleys with low relief (Stein and MacDonald, 2014).

HIQ is located approximately 120 km west of the Mackenzie River Delta. The Mackenzie River has been identified as the main fresh water and sediment source of the Canadian Beaufort Shelf (Doxaran et al., 2012; Holmes et al., 2002; O'Brien et al., 2006). Its ice-free season starts typically in mid-May with a peak discharge in early June (up to 25 000 m³/s) (Doxaran et al.,

2012; Mulligan et al., 2010). However, it is not unusual to find sea ice at the Canadian Beaufort Shelf until mid-July.

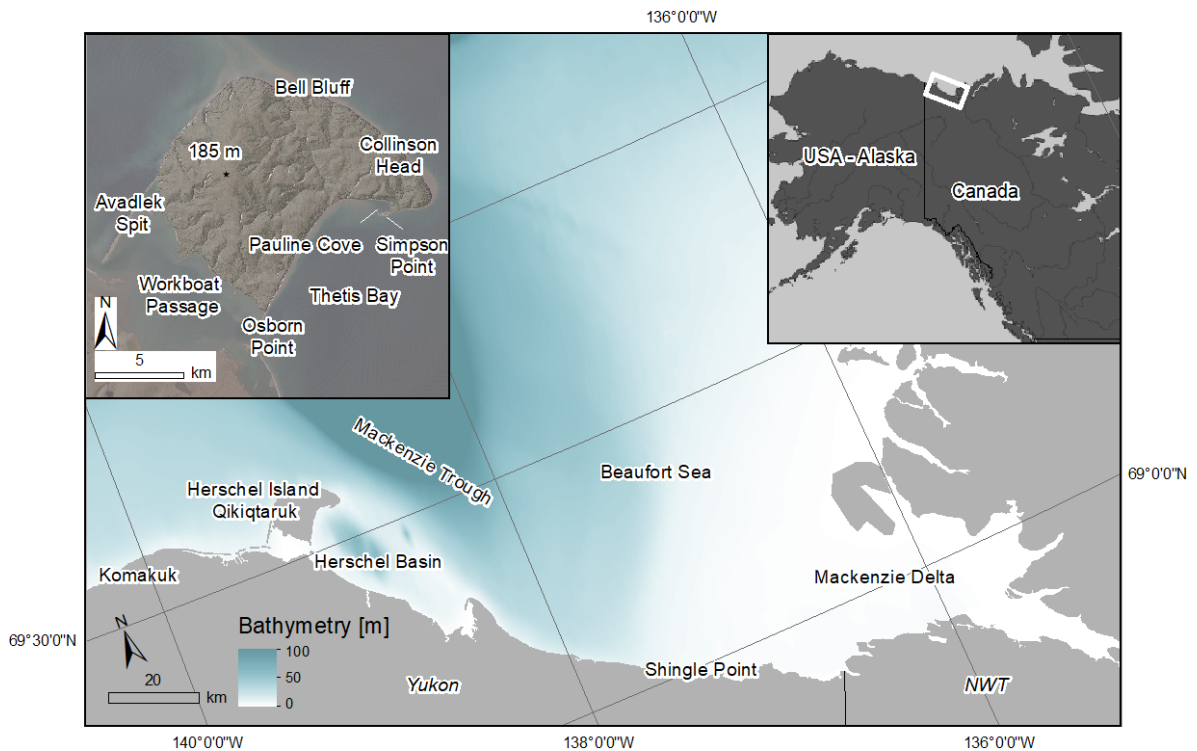


Figure 2-1 Map of the study area. Upper right: Location of the study area (white rectangle) near the northernmost border of Canada and the USA. Main map: Location of the study area in the region of the Yukon Coast, with the Mackenzie Delta in the east, the Yukon Coastal Plain forming the mainland part and HIQ in the west. Bathymetry of the Canadian Beaufort Shelf is indicated by different shades of blue (Federal publications Inc: Nautical charts of the Beaufort Sea, 1998-2016). Upper left: close-up to the study area with indicated geographical locations (Burn and Hattendorf, 2011). A Landsat 5 (TM) true color (band composition 321) image is underlain by a hill-shaded 2 m DEM.

HIQ is separated from the Canadian mainland by the shallow Workboat Passage (< 3 m deep, ca. 2 km wide) (Pelletier and Medioli, 2014). Data on water currents is scarce in the area, but maps based on shoreline morphology indicate that currents predominantly occur in the northern part of Workboat Passage. There, wave action and water currents caused a deepening of the sea floor to its maximum depth of 3 m (Pelletier and Medioli, 2014). The southern part of Workboat Passage is not affected by these currents and is assumed to be a major sediment sink for sediment coming in from the West and from mainland rivers (Pelletier and Medioli, 2014). The north coast of HIQ is erosional and is exposed to maximum wave energy in late summer, while the east coast lies in the lee side of the island and is thus less often affected by storm waves (Forbes,

1997; Hill et al., 1991). The coastal slopes are affected by excessive thermo-denudation and erosion processes, with several retrogressive-thaw-slumps and active-layer detachment slides (Lantuit and Pollard, 2008; Mackay, 1971; Obu et al., 2016).

The climate at HIQ and the southern Beaufort Sea is characterized by long, cold winters and short summers. Monthly mean temperatures vary from about -25 °C in winter (December-February) up to 10 °C during summer (July and August). The mean annual temperature is -9.4 °C (1995-2007) (Burn and Zhang, 2009; Giovando and Herlinveaux, 1981). During the open water season, the time of the year when the ocean water is not covered by ice, winds dominantly blow from ESE and NW directions. In August and September, when storms become more frequent, NW wind conditions are more common (Hill et al., 1991, Figure 2-2). Fetch lengths in the Beaufort Sea may extend 1000 km and significant wave heights may exceed 4 m during storms, thereby enhancing coastal erosion (Atkinson, 2005). However, the sedimentary input from coastal erosion to the Beaufort Sea is just approximately 2% of the sedimentary input of the Mackenzie River (1.8 Tg/a compared to 125 Tg/a) (Couture et al., 2018; Hill et al., 1991; Holmes et al., 2002; Radosavljevic et al., 2015).

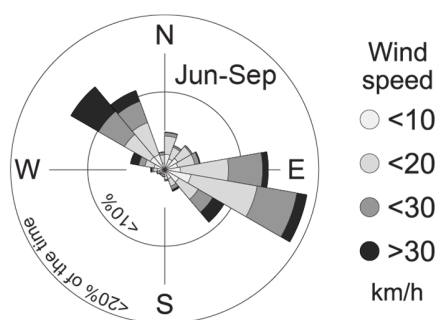


Figure 2-2 Windrose diagram showing wind direction and speed frequency during the sea ice-free period. Data was acquired for 1995 – 2016 from the weather station at Simpson Point, HIQ. Data provided by (Government of Canada, 2018), figure modified after (Radosavljevic et al., 2015).

2.3.2 Landsat Images Acquisition and Processing

In this work, the following Landsat data products are used:

- Level 1T data in the red and near infrared (NIR) channels are processed through the ACOLITE (Vanhellemont and Ruddick, 2014) atmospheric correction scheme to provide the remote sensing reflectance (R_{RS}) and the water turbidity.
- Level 1T data in the Thermal Infrared are used to derive brightness temperature at the top-of-atmosphere.
- In addition, we use the L2 surface reflectance (R_S) product as a means to quality control the ACOLITE-derived remote sensing reflectance (R_{RS}) values.

All Landsat data products were downloaded from the United States Geological Survey (USGS, USGS Earth Explorer). The dataset includes images from Thematic Mapper (TM) from 1982 to 2011, Enhanced Thematic Mapper + (ETM+) from 1999 to 2016 and Operational Land Imager/Thermal Infrared Sensor (OLI/TIRS) from 2013 to 2016. Images from ETM+ acquired after 2003 were mostly excluded, due to the failure of the scan line corrector (SLC) leading to data loss in the resulting imagery of ~23% (Storey et al., 2005). After 2003, only ETM+ image data from flight path 67 were used in this study, because the study area lies within the central part of the image, where the loss of data is minimal. Since the sea is covered by ice from October to May, only images recorded in June, July, August and September without significant sea ice and cloud coverage were considered.

The Surface Reflectance (dimensionless) data product was chosen for this study because it is a standardized atmospherically corrected product processed and provided by the USGS. Landsat TM and ETM+ sensors provide lower radiometric resolution data products compared to Landsat OLI (Vanhellemont and Ruddick, 2014). This results in low signal-to-noise ratios over clear water surfaces, which are darker than land surfaces (except for the blue part of the spectra) or turbid water surfaces. Landsat data products have widely been used for the qualitative retrieval of water column constituents in past decades (MacFarlane and Robinson, 1984). Generally, the water reflectance in the red part of the spectra is well correlated to the light backscattering by suspended sediments in the water column for low to moderate sediment concentrations

(Dogliotti et al., 2015). Previous studies have demonstrated that R_s atmospheric correction algorithms are successfully applied to highly turbid waters (Baughman et al., 2015; Doxaran et al., 2009; Fischer et al., 2017; Petus et al., 2014). However, this has not been tested with Landsat imagery yet.

The atmospheric correction of Landsat satellite data to generate the R_s data product was performed by the USGS according to (Masek et al., 2006). To assess the performance of the R_s (red) data product over water surfaces in contrast to the R_{RS} (red) data product, Landsat scenes processed towards the different reflectance algorithms were compared. These scenes were recorded on September 12, 2011 by Landsat TM and on August 8, 2016 by Landsat OLI over the Canadian Beaufort Shelf. Both scenes were downloaded as Level 1T data product without atmospheric correction and as Level 2 data product from the USGS. R_{RS} data products were computed from L1T products using the ACOLITE software (version 20170619.0) (Vanhellemont and Ruddick, 2014) and applying the exponential extrapolation algorithm with the two spectral bands in the short-wave infrared (SWIR) part of the spectra as recommended by the authors (Vanhellemont and Ruddick, 2015). The ACOLITE software has been selected because it provides a well-established and documented algorithm, which has been validated and tested in various turbidity settings (Novoa et al., 2017; Vanhellemont, 2019). 1500 point values were extracted from both reflectance products for both Landsat scenes within a wide range of reflectance values using value to point in the spatial analyst toolbox in ArcMap 10.4.1. The plots for comparison were compiled in Python. The comparison reveals that R_{RS} (red) and R_s (red) are well correlated for Landsat TM (Figure 2-3 a, $R^2=0.95$) and Landsat OLI (Figure 2-3 b, $R^2=0.99$). This means that the red wavelength S_R data products from both sensors can be used for qualitative investigations of turbidity and SPM. The striping visible in Figure 2-3 a results from the lower radiometric resolution of Landsat TM compared to Landsat OLI, which does not produce binned data. The R_s (red) values from both scenes are roughly three times higher (factor π) than the corresponding R_{RS} (red) value, which is due to that R_{RS} is water-leaving radiance divided by downwelling irradiance and R_s is upwelling radiance divided by downwelling radiance.

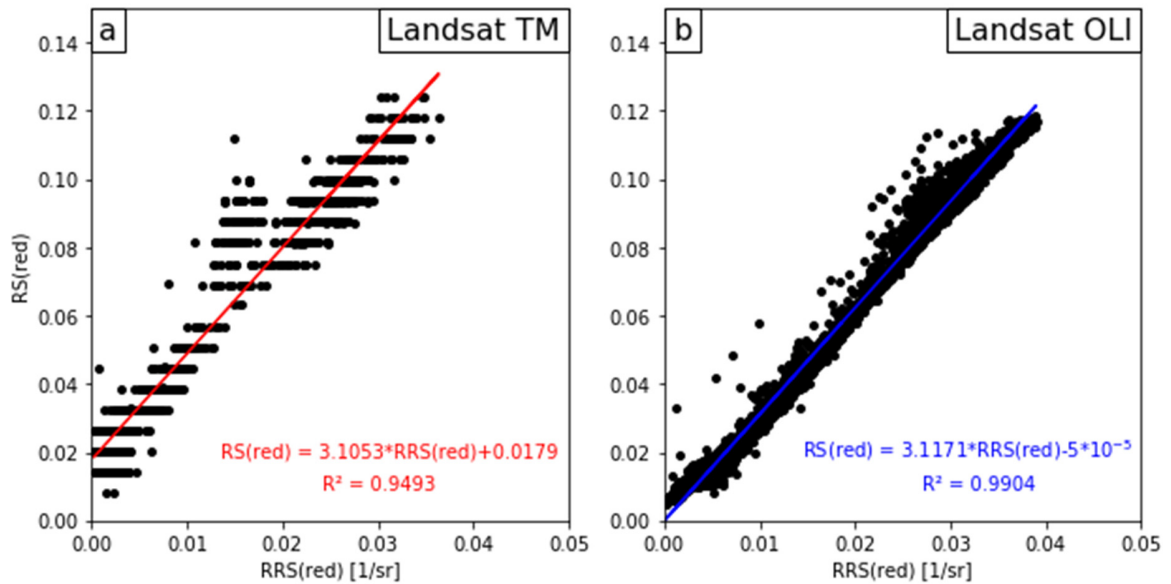


Figure 2-3 Comparison between R_S (red) and R_{RS} (red) data products in coastal and inner shelf waters around HIQ. (a) Landsat TM image recorded on September 12th, 2011, and (b) Landsat OLI image, recorded on August 8th, 2016.

The R_S (red) pre-processed images were classified using the USGS cloud cover and land use detection algorithm ‘cf-mask’ (Foga et al., 2017) to identify land, sea ice, clouds and cloud shadow. However, cloud shadows can not be fully masked as the spectral signature of thin clouds is too close to the one of sediment-loaded waters. The result is a raster image with (almost) only water surfaces (sea, lakes and rivers). A pre-defined area of interest (AOI) around HIQ was used for image processing and analysis to save computing resources. All scenes without artefacts and with matching wind conditions (see section 2.3.5) were used to calculate mean statistical parameters for visualization.

Landsat TM and ETM+ sensors contain the thermal band, band 6, divided into two, the low gain and high gain bands. The TM and ETM+ thermal band spatial resolutions (original pixel sizes) are respectively 120 m and 60 m, but both products are actually resampled to 30 m pixel resolution. The Landsat 8 platform carries the TIRS with the thermal high gain band 10 and low gain band 11 with 100 m original pixel resolution, also resampled to 30 m. Since TIRS band 10 showed higher accuracy than band 11 (Barsi et al., 2014), the high gain bands were used for all three sensors to assure better comparability of the results. Thermal Infrared image data from all Landsat satellites are not provided with an atmospheric correction by the USGS, thus they are

only available as L1T data product. According to Wukelic et al., 1989, the conversion from digital numbers (DN) to spectral radiance (L_λ) and then to brightness temperature (BT, [K]) is given by

$$L_\lambda = L_M \times DN + L_A \quad (2)$$

and

$$BT[K] = K_2 \times \left[\ln \left(\frac{K_1}{L_\lambda} + 1 \right) \right]^{-1} \quad (3)$$

With L_M and L_A [$W/(m^2 \cdot sr \cdot \mu m)$] being the radiance multiplier and radiance add, respectively, and K_1 [K], K_2 [$W/(m^2 \cdot sr \cdot \mu m)$] being thermal constants, which are all given by the Landsat Metafile (MTL). In order to retrieve a temperature in °C as unit,

$$BT[^\circ C] = BT[K] - 237.15 \quad (4)$$

was applied to the results of equation (2). Hereafter, BT always refers to BT [°C]. All calculations were made with ESRI ArcMap version 10.4.1.

Thirty-five images were used in total for the analysis (TM: 25; ETM+: 8; OLI: 2, Table 2-1). Several artefacts had to be manually masked from the images before further processing. These anomalies are caused by small sea ice floes or by small clouds and their shadows that were not recognized by the USGS cf-mask.

Furthermore, the USGS cf-mask did not always properly recognize small or narrow parts of water or land surfaces. This often resulted in false statistical calculations in Pauline Cove and, during ESE wind conditions, west of Avadlek Spit, while Avadlek Spit itself was often not recognized as land surface. These areas have been masked after applying the cf-mask.

All scenes with the same prevailing wind conditions (see section 2.3.5) were stacked together to calculate mean values for each pixel cell.

Table 2-1 List of Landsat scenes used in this study. The data was acquired from the USGS earthexplorer. The wind direction and speed were retrieved from climate data from Environment Canada. The extraction of wind direction is described in section 2.2. Changing wind direction refers to unsteady wind conditions.

Acquisition Date (YYYY-MM-DD)	Sensor	Path/Row	Wind direction	mean wind speed (km/h)
1986-09-14	TM	67/11	changing	18.08
1990-08-17	TM	66/11	ESE	35.17
1990-09-16	TM	68/11	NW	14.50
1990-09-25	TM	67/11	NW	17.50
1992-08-06	TM	66/11	ESE	27.58
1992-08-20	TM	68/11	changing	24.75
1992-08-29	TM	67/11	changing	21.33
1994-07-27	TM	66/11	changing	11.08
1994-08-12	TM	66/11	changing	9.42
1994-09-11	TM	68/11	ESE	23.83
1995-07-12	TM	68/11	ESE	27.92
1997-07-19	TM	66/11	ESE	21.33
1997-08-02	TM	68/11	NW	38.92
1998-07-13	TM	67/11	ESE	15.00
1998-07-22	TM	66/11	ESE	29.08
1999-08-08	TM	68/11	ESE	23.00
1999-08-10	TM	66/11	ESE	27.42
1999-09-02	TM	67/11	ESE	16.75
1999-09-10	ETM+	67/11	ESE	11.00
1999-09-18	TM	67/11	ESE	18.33
1999-09-26	ETM+	67/11	NW	38.33
2001-08-30	ETM+	67/11	changing	9.25
2002-09-11	ETM+	66/11	NW	14.42
2004-08-22	ETM+	67/11	ESE	21.42
2006-07-26	TM	68/11	ESE	29.33
2007-08-23	TM	67/11	changing	23.50
2008-06-30	ETM+	67/11	ESE	21.33
2009-07-27	TM	67/11	NW	11.08
2009-08-21	TM	66/11	changing	12.17
2009-09-05	ETM+	67/11	NW	10.92
2010-08-15	TM	67/11	ESE	19.58
2011-09-12	TM	66/11	changing	9.42
2013-07-15	OLI	66/11	ESE	18.00
2014-07-02	OLI	66/11	NW	16.50
2016-08-07	ETM+	67/11	ESE	24.83

2.3.3 Landsat Turbidity Retrieval

Since no specifically tuned optical algorithm (i.e., water reflectance vs. water turbidity relationship) for our study area exists, we considered a recently published globally applicable turbidity model designed by Dogliotti et al., 2015 and applied it to our dataset. Turbidity [FNU] is a well-known and easily measurable proxy for suspended sediment concentration in sediment transport applications (Gippel, 1995). It here refers to a measurement of water clarity, indicating how intensively light is scattered by suspended particles within the water column (Hussain et al., 2016). The general, semi-analytical turbidity algorithm was calibrated for Landsat TM, ETM+ and OLI imagery using a wide range of field data from coastal and estuarine environments in Europe and South America, based on a switching algorithm of red and NIR R_{RS} values (Dogliotti et al., 2015). The algorithm was applied to the Landsat scenes listed in Table 2-1 using the ACOLITE software (Vanhellemont and Ruddick, 2015, 2014), where turbidity (T) is calculated through:

$$T(\text{red or NIR}) = \frac{A_T^\lambda \rho_w(\lambda)}{(1 - \rho_w(\lambda)/C_T^\lambda)} \quad [\text{FNU}] \quad (5)$$

and

$$T = (1 - w) \times T(\text{red}) + w \times T(\text{NIR}) \quad (6)$$

with $R_w(\lambda)$ being the water reflectance ($R_w = \pi \times RRS$) at wavelength λ , A_T [FNU] and C_T [dimensionless] being wavelength dependent calibration coefficients, w being a weighing coefficient, $T(\text{red})$ being the modelled turbidity using R_{RS} (red), and $T(\text{NIR})$ being the turbidity modelled using R_{RS} (NIR) (Dogliotti et al., 2015). The R_{RS} (red) formula was used for $R_w < 0.05$ and the R_{RS} (NIR) formula was used for $R_w > 0.07$, with a linear blending (w) in the transition zone $0.05 \leq \rho_w \leq 0.07$ according to equation (5). The parameters A_T and C_T were calculated using non-linear least-square regression (Dogliotti et al., 2015).

2.3.4 Transects in the nearshore zone

In order to investigate the variations in Landsat derived water turbidity close to the coast, a transect of alongshore sampling points was generated starting at Simpson Point and moving

clockwise around HIQ (Figure 2-4). This line consists of points with a spacing of 250 m, resulting in 235 points in total. The distance of each point to the coastline is 75 m, meaning there are two pixels between the USGS-cf mask coastline and the sampling point to avoid mixing pixels of land and water. The value to point function in the spatial analyst toolbox in ArcMap 10.4.1 was used to extract R_s (red) and turbidity values at each point of the transect. The extracted points were plotted against each other using Python.

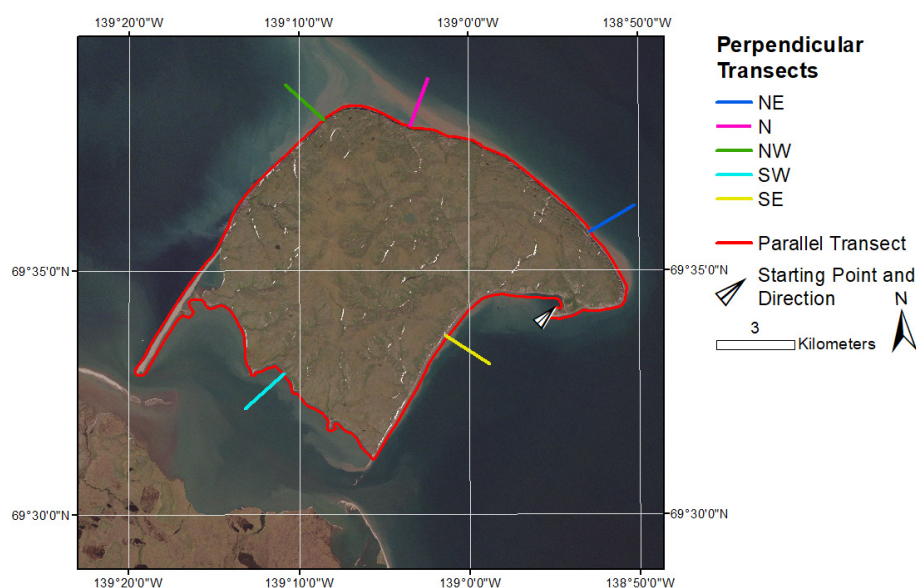


Figure 2-4 Transects in the nearshore zone of HIQ that were used to facilitate the interpretation of gradients of water turbidity, R_s (red), and water temperature. The black arrow indicates the starting point and the direction of the alongshore transect. Background image shows a Landsat 5 (TM) true color (band composition 321) image.

In order to facilitate the interpretation of the BT, R_s (red) and turbidity images, five transects were designed perpendicular to the coast of HIQ. They cover different coastal orientations and range from 0 m to 2000 m distance to the coastline, with 0 m referring to the first water pixel. Each transect was made of 68 points with a spacing of 30 m to cover every Landsat pixel. The pixel values at each of these points were extracted using the extract multi values to point function in the spatial analyst toolbox in ArcMap 10.4.1. The attribute tables were then exported as .txt and processed using Python.

2.3.5 Wind Data

Wind data were collected for the weather stations HIQ and Komakuk Beach from the climate archive of Environment Canada (Government of Canada, 2018). Data from Komakuk Beach were used before the HIQ station was set up in 1994 and whenever the weather recording at the HIQ station failed. To receive consistent data over the whole investigation period, only measurements from 00:00, 06:00, 12:00 and 18:00 were extracted from all datasets, even though hourly data from both stations is available since 1994 (Burn and Zhang, 2009).

Wind speed and direction observations were acquired for the date of each Landsat scene and the two previous days in order to extract representative dispersal patterns, in total 12 measurements per scene. When six out of the last eight six-hourly measurements (date of the scene plus the previous day) or nine out of twelve had comparable wind directions, the conditions were assumed to be steady and the scene was used for this study.

The wind data was used to reconstruct the general wind direction patterns over several days so that an acquisition of wind data each six hours was sufficient and the only way to provide consistent and comparable data over the whole observation period. Manually controlled random samples in the hourly dataset showed no significant anomalies compared to the six hours interval used per day.

In total, 18 scenes showed continuous ESE wind conditions (TM: 13, ETM+: 4, OLI: 1), 8 continuous NW wind conditions (TM: 4, ETM+: 3, OLI: 1) and 9 showed changing wind conditions (TM: 8, ETM+:1), which refers to unsteady wind conditions during the twelve observations.

2.4 RESULTS

2.4.1 Brightness Temperature

The highest BT values were detected during steady ESE wind conditions along the SE coast of HIQ ($> 10\text{ }^{\circ}\text{C}$), and the lowest values near the NW coast ($< 3\text{ }^{\circ}\text{C}$, Figure 2-5 c). Changing wind conditions also resulted in high BT at the SE coast as observed during steady ESE wind

conditions ($\sim 9\text{ }^{\circ}\text{C}$, Figure 2-5 a). Similar low BT values as the ones detected during steady ESE wind conditions were detected along the NW coast during steady NW wind conditions ($\sim 4\text{ }^{\circ}\text{C}$, Figure 2-5 b). However, both wind regimes (changing wind conditions, and steady NW wind conditions) did not generate a range in BT as large as generated during steady ESE wind conditions (Figure 2-5 c). In short, the highest temperatures were observed during steady ESE wind conditions, except for an area at the NW coast of HIQ, which is shielded from the warm Mackenzie River plume by the island.

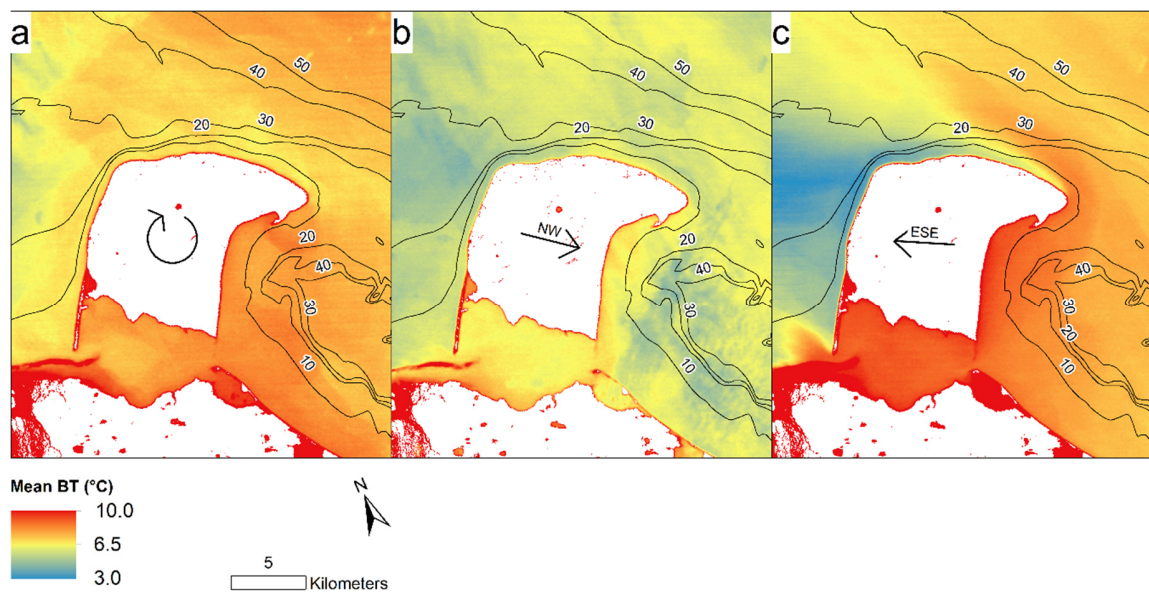


Figure 2-5 Mean BT from Landsat thermal infrared channels, for (a) changing wind conditions, (b) steady NW wind conditions and (c) steady ESE wind conditions. Prevailing wind conditions are indicated with arrows in the center of each picture. The number of used scenes per wind condition are listed in Table 2-1. Red areas indicate areas of high BT, white areas indicate land surface areas. Mean BT is highest in (c) and lowest in (b). Bathymetry is indicated by black lines (Federal publications Inc: Nautical charts of the Beaufort Sea, 1998-2016). Note the very cold BT in (c) at the NW coast of HIQ and the large contrast to the SE coast and Workboat Passage. The calculated standard deviation for each image is given in Appendix A.

During steady ESE conditions (Figure 5 c), very cold BT values occur at the NW coast of HIQ and there is a large contrast to the SE coast and Workboat Passage. The spatial BT pattern outline that the cold surface water appears in a wake form at the Western part of HIQ. The mean BT values are lowest during steady NW wind conditions (Figure 2-5 b), which is partly caused by a larger number of late summer satellite acquisitions. The influence of bathymetry on BT is

limited under all three conditions. The calculated standard deviation for each image is given in Appendix A.

The BT spatial distribution shows similar spatial patterns during changing and steady NW wind conditions, but absolute values are higher during changing wind conditions (~ 4 °C). During steady NW and changing wind conditions, BT decreases with increasing distance from the coast. This can be seen at the SE and NW coasts, as well as NE of Collinson Head. In contrast under steady ESE wind conditions, BT values rise with increasing distance from the coast along the NE coast.

The Workboat Passage shows comparatively uniform BT for all three wind conditions (Figure 2-5). The BT between the barrier islands and the Canadian mainland were higher than in the Workboat Passage for all three wind conditions. In the Workboat Passage, the BT were highest during steady ESE wind conditions (~ 10 °C) and lowest during steady NW wind conditions (~ 5 °C).

2.4.2 Surface Reflectance and Turbidity Mapping

The mean R_s (red) values, which were used as proxy to estimate long-term average spatial patterns in water turbidity, showed the highest values during steady ESE wind conditions (mean reflectance value of 0.0323) and lowest values during steady NW wind conditions (mean value of 0.0241, Figure 2-6). An area of high turbidity was consistently present at the NE coast of HIQ, an area that is characterized by high cliffs (R_s (red) > 0.055). Another area along the SE coast was also characterized consistently by high turbidity (R_s (red) > 0.055). This area is characterized by multiple retrogressive thaw slumps. During steady ESE wind conditions, dispersal patterns at the NE coast indicate longshore drift extending towards the West. This results in a broad area of high turbidity at the NW coast, which does not exist during changing or steady NW wind conditions. In contrast to the temperature dispersal patterns (Figure 2-5), the reflectance values decreased with increasing distance from the coastline under all three conditions.

Bathymetry is a large influencing factor on turbidity, especially along the NE and the NW coast of HIQ. During changing and steady NW wind conditions, high turbidity is limited to shallow

water depths (below 10 m, Figure 2-6 a and b). During steady ESE wind conditions, high turbidity extends up to water depths of 30 m along the NE coast and depths of 20 m along the NW coast (Figure 2-6 c). Along the SE coast, high turbidity is limited to the immediate vicinity of the coastline under all three wind conditions.

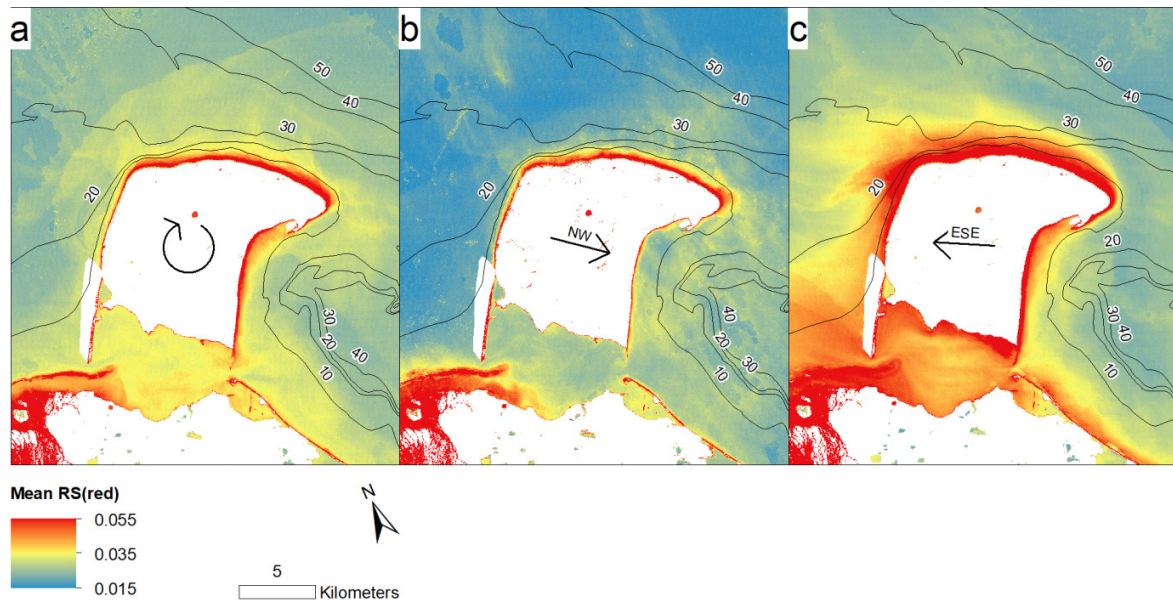


Figure 2-6 Mean R_S (red), that was used as proxy for turbidity, for (a) changing wind conditions, (b) steady NW wind conditions and (c) steady ESE wind conditions. Prevailing wind conditions are indicated with arrows in the center of each picture. The number of used scenes per wind condition are listed in Table 2-1. Red areas indicate areas of high turbidity, white areas indicate land surfaces or areas of failed atmospheric correction. Bathymetry is indicated by black lines (Federal publications Inc: Nautical charts of the Beaufort Sea, 1998-2016). Turbidity is highest in (c) and lowest in (b). Note the similar dispersal patterns in (a) and (b) compared to (c). The calculated standard deviation for each image is given in Appendix A.

The Workboat Passage was, under all three conditions, an area of high water turbidity and showed clear sediment pathways, especially close to the inlets (Figure 2-6 c). A thin band of high turbidity (R_S (red) > 0.055) could be observed around the whole island. This band showed high turbidity values under all conditions and can be attributed to coastal erosion and resuspension due to waves.

Figure 2-6 a and b, displaying changing wind directions and steady NW winds, respectively, showed rather similar dispersal patterns with a comparable fringe of high turbidity and a strong

gradient towards lower values from the coast towards the offshore. Both configurations differ substantially from the sediment dispersal observed under steady ESE winds (Figure 2-6 c).

The Landsat derived turbidity values reveal similar sediment dispersal patterns compared to the Rs (red) data, even though the differences between the wind regimes are larger (Figure 2-7). The gradient from high turbidity in the nearshore (> 50 FNU) to lower values offshore (< 5 FNU) is larger when applying the (Dogliotti et al., 2015) turbidity algorithm compared to the RS results (Figure 2-6). This can be observed along the NW, NE and along parts of the SE coast of the Island.

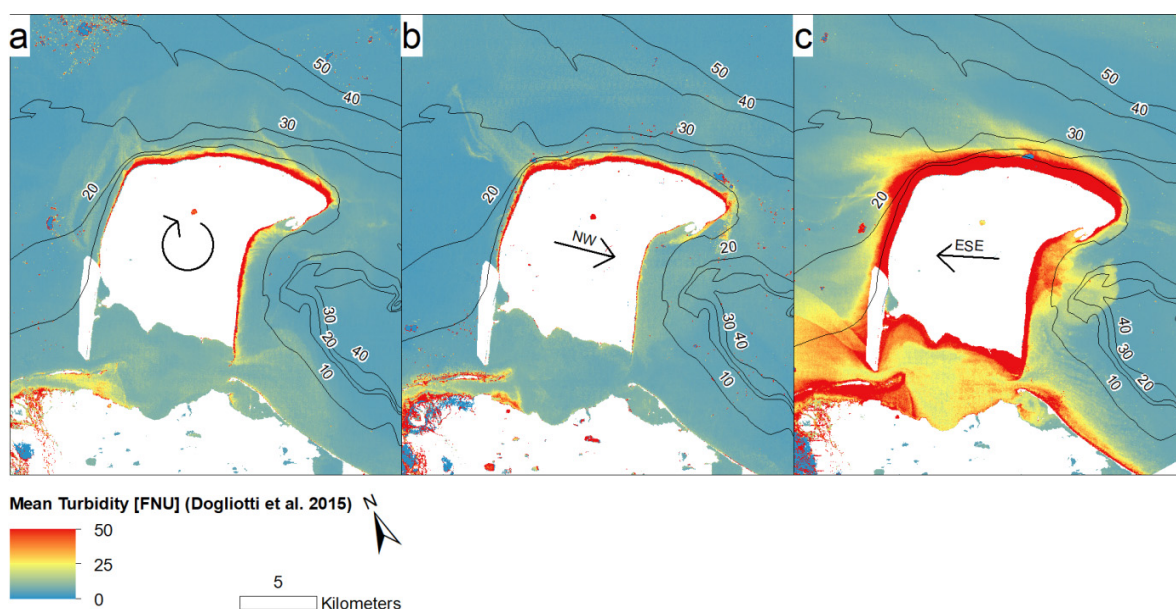


Figure 2-7 Mean Landsat retrieved turbidity after (Dogliotti et al., 2015) for (a) changing wind conditions, (b) steady NW wind conditions and (c) steady ESE wind conditions. Prevailing wind conditions are indicated with arrows in the center of each picture. The number of used scenes per wind condition are listed in Table 2-1. Red areas indicate areas of high turbidity, white areas indicate land surfaces or areas of failed atmospheric correction. Bathymetry is indicated by black lines (Federal publications Inc: Nautical charts of the Beaufort Sea, 1998-2016). Turbidity is highest in (c) and similar in (a) and (b).

During steady ESE wind conditions, a larger filament structure is resolved at the SE coast of the island, where suspended material gets transported towards Herschel Basin (Figure 2-7 c). Several of these filament features were also resolved at the NW coast under all three wind conditions, albeit to a smaller scale. Bathymetry has a comparable influence on turbidity as revealed in Figure 2-6, especially during steady ESE wind conditions (Figure 2-7 c). During

changing and steady NW wind conditions (Figure 2-7 a and b), high turbidity (> 50 FNU) is limited to water depths shallower than 10 m.

2.4.3 Gradients in the nearshore zone

Figure 2-8 a shows turbidity and R_s (red) values along the coastline of HIQ. In the R_s (red) dataset, the highest values were observed in Thetis Bay, along the N coast of the Island, and around Collinson Head (R_s (red) ~ 0.08). This indicates that the sediment supply along the SE coast, which is dominated by retrogressive thaw slumps, is comparable to the one along the NE coast, which is dominated by steep cliffs. Lower values were detected in Pauline Cove and west of Avadlek Spit (R_s (red) 0.04 - 0.05), which are the areas, where the cf-mask did not perform adequately. Thus, these lower values might not reflect reality. The overall variation of R_s values is low, except in the two aforementioned regions.

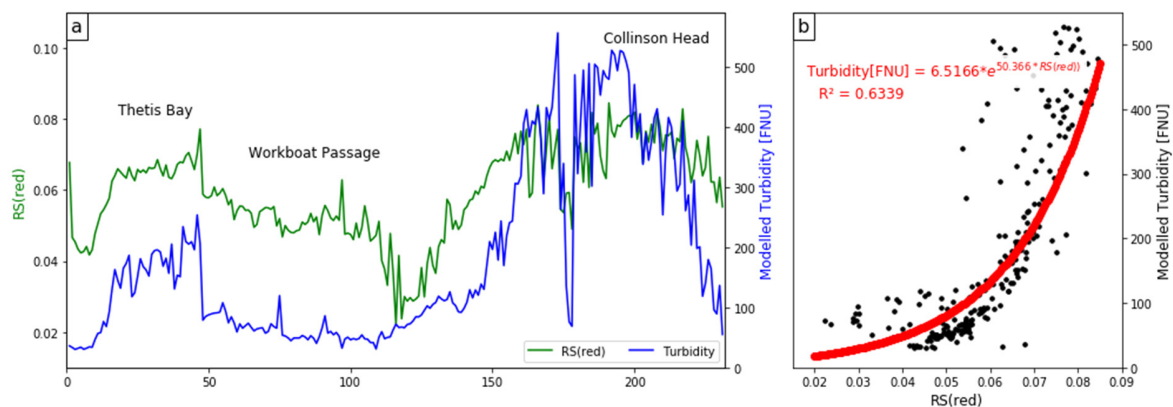


Figure 2-8 (a) Comparison between the maximum turbidity and R_s (red) values observed along the coast of HIQ. The blue line represents the Dogliotti et al. (2015) (Dogliotti et al., 2015) turbidity model, the green line the corresponding R_s (red) value. (b) Correlation between the R_s (red) and turbidity values in the nearshore zone. The red line represents the best exponential fitting function. The values were extracted at points along a transect starting at Simpson Point and moving clockwise (Figure 2-4).

In the turbidity dataset modelled according to (Dogliotti et al., 2015), the turbidity values along the N coast (up to 500 FNU) are remarkably higher than in Thetis Bay (up to 200 FNU) or in the Workboat Passage (up to 100 FNU). The turbidity values also decrease considerably from 400 FNU at Collinson Head to 50 FNU at Simpson Point. This indicates, in contrast to the R_s dataset that the eroding permafrost cliffs along the NE coast provide higher sediment supply to the nearshore zone than retrogressive thaw slumps along the SE coast. The variation of turbidity

values around the island is larger compared to the variation of the corresponding R_s (red) value, which is due to the exponential design of the turbidity algorithm (Figure 2-8 b).

Figure 2-8 b shows the correlation of the turbidity value with the corresponding R_s (red) value displayed in Figure 2-8 a. The correlation of both values is decent, especially for turbidity values below 250 FNU. As previously reported in the literature, the red band saturates at higher turbidity values, which results in a stronger noise (Dogliotti et al., 2015).

The analysis of the five transects perpendicular to the coastline of HIQ show the aforementioned gradients from the nearshore towards the offshore. Figure 2-9 a and b show the BT gradients during steady NW and steady ESE wind conditions, respectively. Each transect shows BT decrease within the first 100 m off the coastline, with BT values dropping between 1 °C and 4 °C. The only exception is the NW oriented transect during steady NW wind conditions, which does not show a large variation close to the coastline. During steady ESE wind conditions, the BT values along the NE and N coast rise with increasing distance to the coastline and reach similar values in 2000 m distance as they were direct at the coastline. All other transects do not show a remarkable variation beyond the dropping of BT close to the coast. During steady ESE wind conditions, BT values are remarkably higher at the SE and SW coast than during NW wind conditions (~10 °C compared to ~6 °C). Along the NW coast, the BT are higher during steady NW wind conditions (~5 °C compared to ~3 °C during steady ESE wind conditions). Along the N coast, BT do not differ remarkably during the two wind conditions.

Figure 2-9 c and d show the R_s (red) gradients during steady NW and steady ESE wind conditions, respectively. Every transect but one shows a decline of R_s (red) with increasing distance from the coastline. The only exception is the SW coast during steady NW wind conditions, where the R_s (red) does not change significantly with increasing distance from the coastline. The largest gradient was detected along the NE coast, where the R_s (red) value decreases from ~0.075 close to the coast to less than 0.03 in 2000 m distance off the coastline. The R_s (red) values during steady ESE wind conditions are higher than the ones during steady NW conditions and roughly twice as much in 2000 m distance off the coast. During steady ESE wind conditions, the R_s (red) values do not drop to a background value which does not change

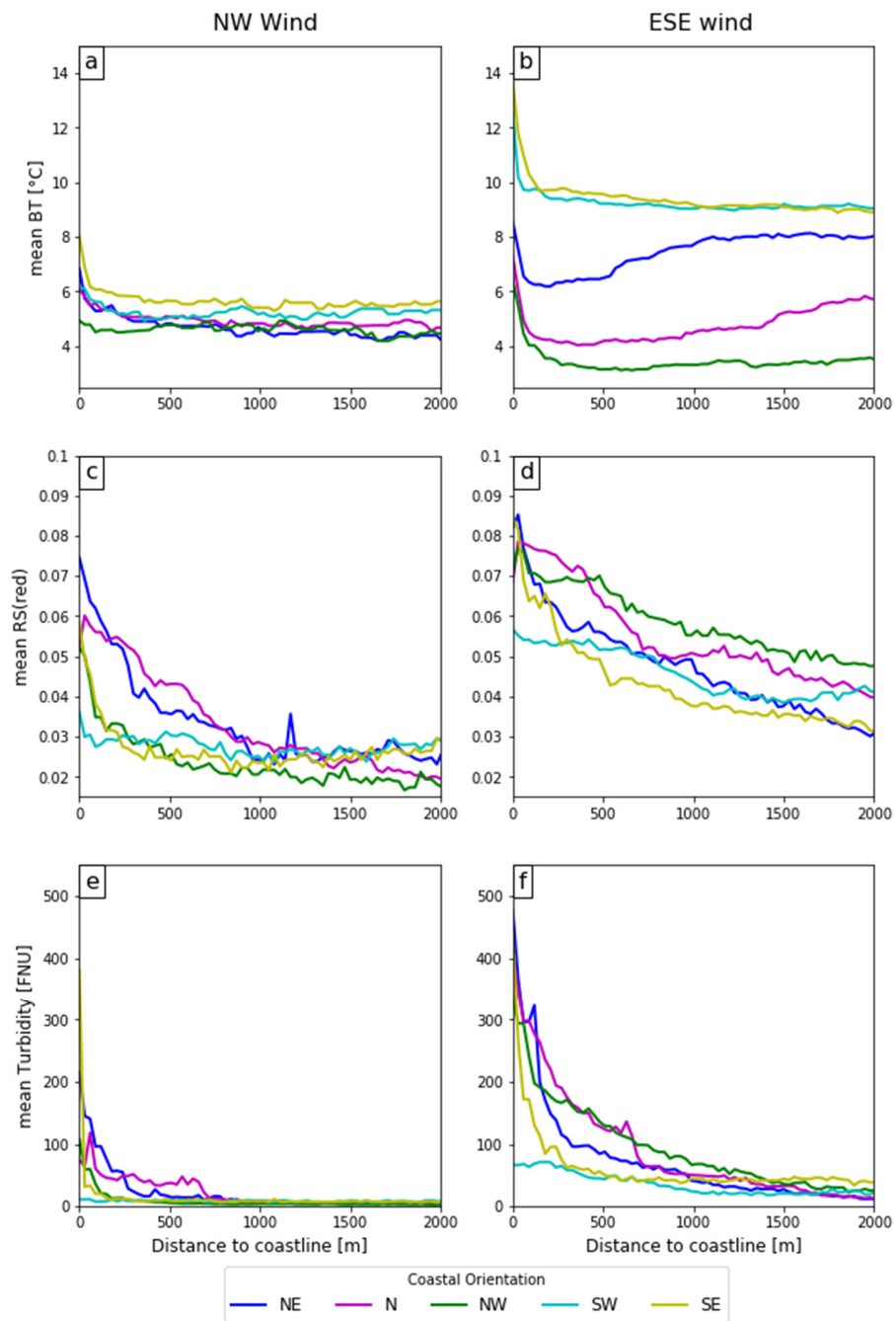


Figure 2-9. Transects perpendicular to the coastline of HIQ to quantify the gradients from the nearshore to the offshore. (a) Mean BT during NW wind conditions. (b) Mean BT during ESE wind conditions. (c) Mean RS (red) during NW wind conditions. (d) Mean RS (red) during ESE wind conditions. (e) Mean turbidity during NW wind conditions. (f) Mean turbidity during ESE wind conditions. Different coastal orientations are indicated by different colors. The position of each transect line is displayed in Figure 2-4.

significantly with increasing distance off the coastline, while this seem to be the case during steady NW wind conditions at a distance of 1000 m off the coastline (R_s (red) ~ 0.025).

Figure 2-9 e and f show the turbidity gradients during steady NW and steady ESE wind conditions, respectively. Each transect shows a decline of turbidity with increasing distance off the coastline. The only exception is the SW during steady NW wind conditions, where the turbidity does not decline remarkably. In close distance to the coastline, the slope of the declining transect lines is steeper compared to the R_s (red) dataset. During steady NW wind conditions, turbidity reaches a background level in 750 m distance off the coast (~ 5 FNU). During steady ESE wind conditions, turbidity reaches a background level in 1500 m distance off the coast (10 -20 FNU). High turbidity values (> 400 FNU) were detected very close to the N, NE, NW and SE coast during steady ESE wind conditions. During steady NW wind conditions, turbidity values exceed 200 FNU only at the NE and SE coast.

2.5 DISCUSSION

The strong turbidity gradients observed around HIQ from the nearshore to offshore zone demonstrate that Landsat imagery is a powerful instrument to resolve features otherwise not seen in coarser scale imagery as indicated by (Vanhellemont and Ruddick, 2014). This study is one of the first applications of Landsat archive imagery to resolve small-scale sediment dispersal patterns and surface water temperature patterns in Arctic nearshore environments. Figure 2-8 and Figure 2-9 reveal high turbidity values, which were not reported in Arctic nearshore environments in the literature yet and highlight the importance of the nearshore zone in the mobilization and transport of sediment and organic matter.

Our results suggest that most of the suspended material in the nearshore zone of HIQ remains in the alongshore surface waters and that offshore transport through surface waters is limited. The material observed close to the coast is likely to be transported alongshore, to quickly settle in the water column or to be exported offshore by bottom currents. The mean R_s (red) declines from > 0.06 directly at the coast to less than 0.02 within a few hundreds of meters, independently of wind conditions and show the presence of a thin yet sediment-rich band of water along the coast. This highly turbid water, potentially holding large amounts of organic matter, cannot be

resolved by the usual applied medium resolution ocean color remote sensing platforms such as MODIS. We show that even the older Landsat sensors (TM, ETM+) are powerful tools for ocean color applications and allow the investigation of Arctic nearshore environments by providing high spatial resolution optical imagery spanning over nearly 35 years.

Our results show that turbidity and R_s (red) are well correlated for turbidity values < 250 FNU. This covers most data points in our study area, making the R_s (red) a good proxy to map turbidity in Arctic nearshore zones at low to medium sediment loads. However, it is also shown that R_s (red) becomes saturated when mapping higher turbidity values, so the turbidity model designed by Dogliotti et al., 2015 is most appropriate to map the strong gradients in the nearshore zone. In our images, sediment pathways from the nearshore to the offshore were visible at the NW coast of HIQ and at the SE coast towards Herschel Basin during steady ESE wind conditions. These pathways were not resolved in the averaged R_s (red) results which highlights the superior performance of the turbidity model designed by Dogliotti et al., 2015 to detect gradients in the nearshore zone. These pathways show that offshore transport of sediment might be observed at the water surface, especially in locations characterized by a large supply of sediment (i.e. retrogressive thaw slums and relatively sheltered shore morphology such as the SE coast of HIQ). Yet, these features were isolated along the coastline and do not reflect the dominant mechanism for sediment transport under the observed conditions.

Coastal erosion rates are large in the area (Obu et al., 2016) and contribute large amounts of sediment to the nearshore zone (Figure 2-10). Figure 2-10 shows that coastal erosion rates are highest at the NW, N, and NE coasts of HIQ. These coastal sections all showed the highest turbidity in our results, which indicate the supply of significant amount of material to the nearshore zone, albeit in a narrow band located along the coast. Along the SE coast of HIQ, the coastal erosion rates are considerably lower than along the NE coast. Yet, the same relation was detected for turbidity, which supports the hypothesis that coastal erosion is the main contributor of suspended sediment in this area. Generally, the high turbidity gradients observed in our results indicate that most of the eroded material from the coast remains alongshore, rapidly settles at the seafloor or is transported by bottom currents.

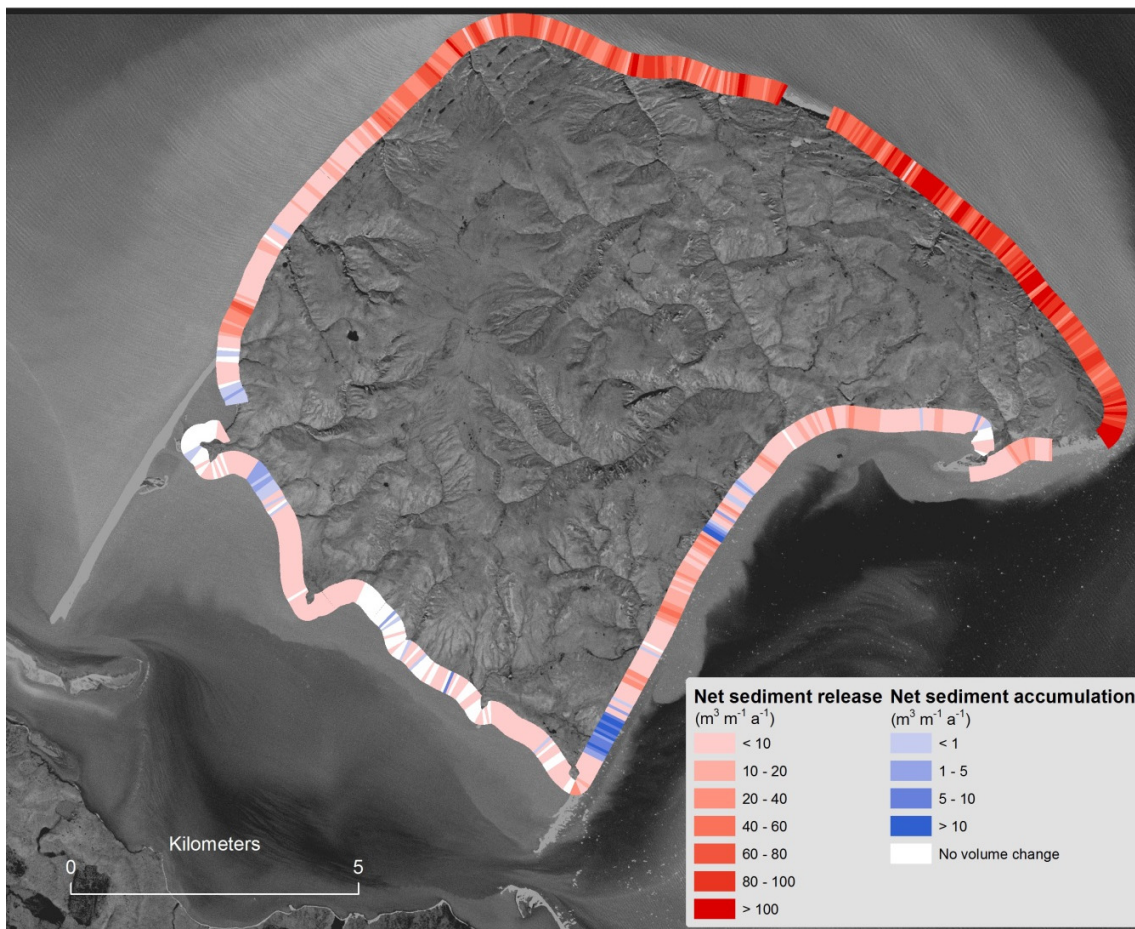


Figure 2-10. Volumetric coastal erosion at HIQ based on DEM elevation changes from 2000-2011 (Obu et al., 2016).

Bailard, 1982 suggests that the distinction between onshore and offshore sedimentation of suspended sediment is a function of wave height. These results indicate that a significant wave height threshold of 1.0 m or above is required to transport suspended sediment offshore. According to Hill and Nadeau, 1989, significant wave height in the Beaufort Sea exceeds 1.2 m only during strong storm events. In our study area, the majority of waves have a significant wave height of less than 0.8 m (Hill and Nadeau, 1989). This indicates a limited potential for offshore transport and the potential important role of alongshore transport in mobilizing sediment in this area. Estimations of the amount of suspended sediment transported away from the coast are rare; Pfalz, 2017 estimated that approximately 20 % of the eroded material by the mainland rivers (Mackenzie River excluded) and coastal erosion is stored in Herschel Basin, a major sedimentary sink at the Canadian Beaufort Shelf. This would imply that an important part of the

sediments remains close to the coast and contributes to the growth of sedimentary landforms such as spits and barrier islands.

Riedel, 2017 analyzed the origin of the sediment in the western part of Herschel Basin. Using biomarker endmember modeling, the author showed that HIQ is the predominant sedimentary origin at the western edge of Herschel Basin. This shows that offshore transport of sediment is taking place, albeit not at the water surface, a process that is not captured by our satellite images. This also indicates the paramount role of coastal erosion for sediment mobilization from HIQ for the sedimentary budget of Herschel Basin and the adjacent nearshore zone in contrast to the Mackenzie River sedimentary input. The Mackenzie River sedimentary load (125 Tg/a) (Holmes et al., 2002) is much higher than the sediment released by coastal erosion along the Yukon Coast (1.8 Tg/a) (Couture et al., 2018), yet this load is confined to the immediate vicinity of the delta and does not reach the shore of HIQ in significant amounts. Our results show that the ratio between the sediment amounts exported from coastal erosion and the Mackenzie River is greater during NW wind conditions.

The large turbidity values observed in the nearshore zone (Figure 2-6, Figure 2-7 and Figure 2-8) are not only associated with fresh material eroded from the coast. Vertical mixing keeps the sediment in suspension. Hill et al., 1991 pointed out that bottom currents are driving resuspension in the nearshore zone during storm events, while the influence of waves is higher during normal weather conditions (Bloesch, 1982). Héquette and Hill, 1993 detected storm related bottom currents in the Canadian Beaufort Sea three to five times stronger than the mean currents (up to 0.5 m/s). This shows that the high turbidity values observed along the nearshore zone are not necessarily entirely related to coastal erosion, but also to resuspension. It also shows that bottom currents have the potential to contribute to the offshore transport of sediment, which cannot be resolved by our satellite imagery. Another possible trigger for resuspension is upwelling. Williams et al., 2006 reported on bottom currents developing beyond the shelf break, moving westwards through the Mackenzie Trough and surfacing NW of HIQ. These currents might add to the high turbidity and low BT values observed during steady ESE wind conditions (Figure 2-5, Figure 2-6, and Figure 2-7). This also shows that temperature differences are not entirely related to the Mackenzie River plume extent, but also to water masses originating beyond the shelf break.

Doxaran et al., 2015 suggested an increased occurrence of resuspension due to the rising discharge and sedimentary load of Arctic Rivers at shallow water depths close to their deltas. Assuming that rivers along the Yukon coast experienced similar changes in their discharge regime (Van Vliet et al., 2013), resuspension along the whole Yukon coast should have been increasing. This would be particularly visible in the Workboat Passage. Our data can not determine whether the resuspension has increased over time, but it supports the fact that the Workboat Passage is characterized by very high turbidity values, which is likely linked to the inputs from creeks and rivers draining into it.

2.6 CONCLUSION

The aim of this study was to investigate the dynamics of water temperature and turbidity in the coastal and innershelf waters of the Canadian Beaufort Sea around HIQ. Thirty years of Landsat satellite imagery were analyzed under seasonal changing meteorological forcing. The results showed clear spatial differences for both observed parameters under the two prevailing wind conditions (ESE and NW). During steady ESE wind conditions, turbidity and water temperature values showed significantly higher values in the nearshore zone. The differences in water temperature are mainly caused by the changing extent of the Mackenzie River Plume. Turbidity is mainly driven by local coastal and nearshore processes such as erosion and resuspension. Our results also show that water turbidity is highest close to the north coast of HIQ, which experiences the highest coastal erosion rates, indicating that coastal erosion is the main contributor of sediment to the nearshore zone.

The strong gradient of turbidity from the nearshore to the offshore zone under both steady ESE and steady NW wind conditions indicates that the bulk part of eroded sediment does not remain at the water surface and gets transported alongshore or rapidly settles at the seafloor. The only stable pathway of sediment that get transported to the offshore was identified NNW of HIQ. During steady ESE wind conditions, another pathway was identified SE of the island towards Herschel Basin.

In this study, we showed that Landsat satellite imagery provides coastal observations (e.g. temperature and turbidity within surface waters) at a high spatial resolution in contrast to the

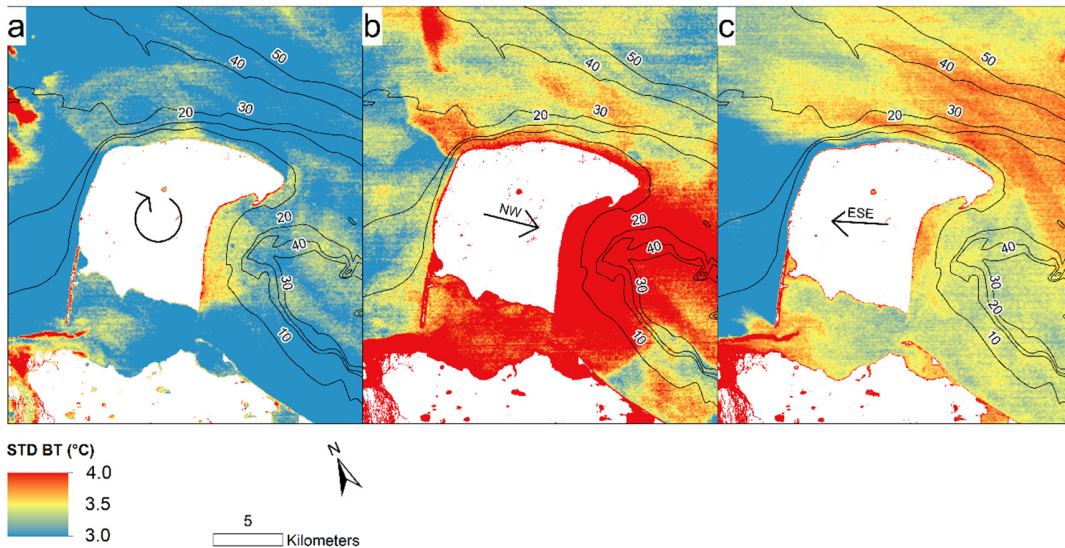
coarser spatial resolution of ocean color satellite sensors. Its high spatial resolution and the long time series of spatially consistent data (since 1982) are unique to resolve hydrodynamic processes close to the shoreline and to compare data ranging over more than three decades.

To improve the results of this study and of Landsat based ocean color remote sensing in the area, *in-situ* measurements from the study area are needed to establish an optical model especially tuned to the conditions encountered in the southern Beaufort Sea and the nearshore zone of HIQ. Higher spatial resolution imagery would also enable the resolution of smaller scale sediment dispersal patterns such as resuspension. This could be eventually coupled with geochemical sampling to calculate small-scale sediment and organic matter budget in coastal zones of the Arctic Ocean, which are highly impacted by climate change. Ultimately, our approach bears great potential to resolve processes not covered by other sensors and could be extrapolated to other coastal areas. This will conclusively foster our knowledge of the reaction of Arctic nearshore environments to global climate change.

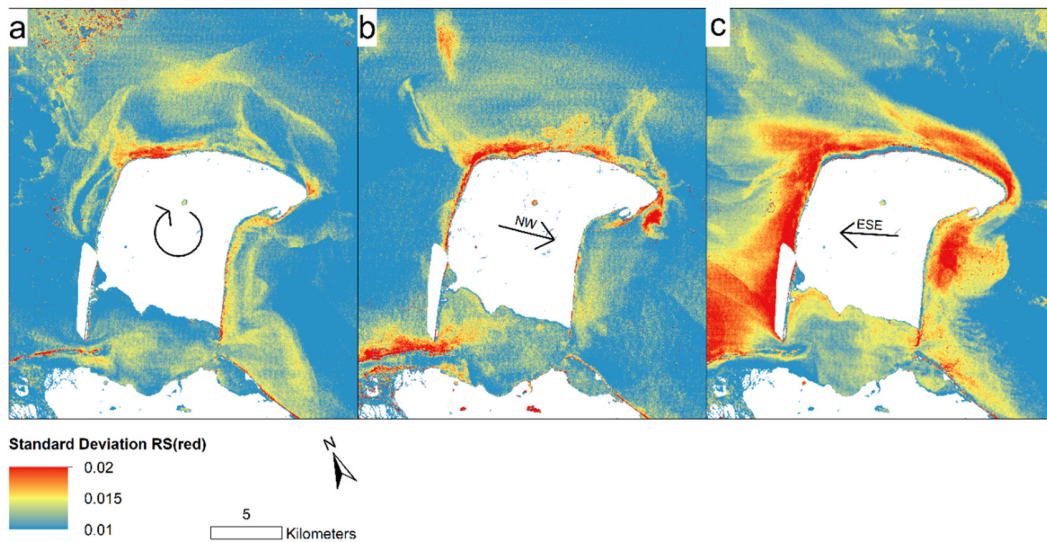
Acknowledgments

This publication is part of the Nunataryuk project. The project has received funding under the European Union's Horizon 2020 Research and Innovation Programme under grant agreement no. 773421. Konstantin P. Klein was financially supported by a Ph.D. stipend by the University of Potsdam (PoGS Potsdam Graduate School). USGS and NASA are acknowledged for Landsat imagery. We also would like to thank three anonymous reviewers for their many constructive comments significantly contributing to improve the quality of this manuscript.

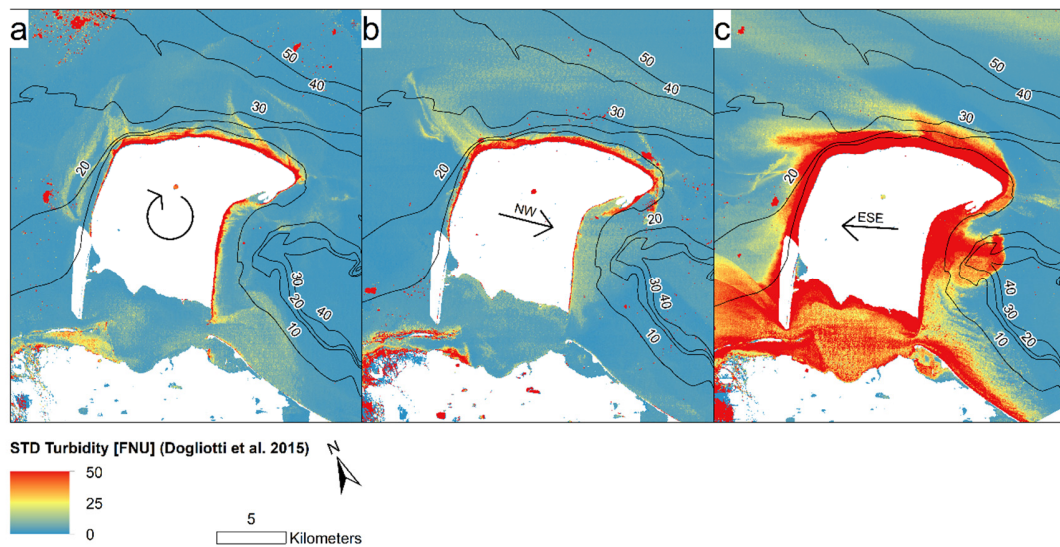
APPENDIX A



Standard Deviation (STD) of BT from thermal infrared channels, for (a) changing wind conditions, (b) steady NW wind conditions and (c) steady ESE wind conditions. Prevailing wind conditions are mentioned with arrows in the center of each picture. The number of used scenes per wind condition can be seen in Table 2-1. Red areas indicate areas of high STD, white areas indicate land surface areas.



Standard Deviation (STD) of R_s (red), that was used as proxy for turbidity, for (a) changing wind conditions, (b) steady NW wind conditions and (c) steady ESE wind conditions. Prevailing wind conditions are mentioned with arrows in the center of each picture. The number of used scenes per wind condition can be seen in Table 2-1. Red areas indicate areas of high STD, white areas indicate land surfaces or areas of failed atmospheric correction.



Standard Deviation (STD) of turbidity calculated after (Dogliotti et al., 2015), for (a) changing wind conditions, (b) steady NW wind conditions and (c) steady ESE wind conditions. Prevailling wind conditions are mentioned with arrows in the center of each picture. The number of used scenes per wind condition can be seen in Table 2-1. Red areas indicate areas of high STD, white areas indicate land surfaces or areas of failed atmospheric correction.

3 THE ARCTIC NEARSHORE TURBIDITY ALGORITHM (ANTA) - A MULTI SENSOR TURBIDITY ALGORITHM FOR ARCTIC NEARSHORE ENVIRONMENTS

3.1 ABSTRACT

The Arctic is greatly impacted by climate change. The increase in air temperature drives the thawing of permafrost and an increase in coastal erosion and river discharge. This leads to a greater input of sediment and organic matter into coastal waters, which substantially impacts the ecosystems by reducing light transmission through the water column and altering the biogeochemistry, but also the subsistence economy of local people, and changes in climate because of the transformation of organic matter into greenhouse gases. Yet, the quantification of suspended sediment in Arctic coastal and nearshore waters remains unsatisfactory due to the absence of dedicated algorithms to resolve the high loads occurring in the close vicinity of the shoreline. In this study we present the Arctic Nearshore Turbidity Algorithm (ANTA), the first reflectance- turbidity relationship specifically targeted towards Arctic nearshore waters that is tuned with *in-situ* measurements from the nearshore waters of Herschel Island Qikiqtaruk in the western Canadian Arctic. A semi- empirical model was calibrated for several relevant sensors in ocean color remote sensing, including MODIS, Sentinel 3 (OLCI), Landsat 8 (OLI), and Sentinel 2 (MSI), as well as the older Landsat sensors TM and ETM+. The ANTA performed better with Landsat 8 than with Sentinel 2 and Sentinel 3. The application of the ANTA to Sentinel 2 imagery that matches *in-situ* turbidity samples taken in Adventfjorden, Svalbard, shows transferability to nearshore areas beyond Herschel Island Qikiqtaruk.

3.2 INTRODUCTION

Climate change is stronger in the Arctic than anywhere else on Earth (Serreze and Barry, 2011): intensified permafrost thaw (Biskaborn et al., 2019), increased river discharge (McClelland et al., 2016) and stronger coastal erosion (Fritz et al., 2017) have significant impacts on the

biophysical system. Permafrost coasts are particularly vulnerable to warming air temperatures, as frozen sediments thaw and become vulnerable to wave erosion (Lantuit and Pollard, 2008; McGillivray et al., 1993). Recent studies have shown that this has the potential to mobilize large carbon pools stored in permafrost (Tank et al., 2018), to release carbon and nutrients into nearshore areas (Fritz et al., 2017), or to release greenhouse gases directly into the atmosphere (Romanovsky et al., 2010; Tanski et al., 2019; Vonk et al., 2012).

Arctic nearshore and shelf areas have experienced increased sediment input due to increased river discharge, increased coastal erosion and increased glacial melting during the last decades (Déry et al., 2009; Jones et al., 2009; McClelland et al., 2006; World Glacier Monitoring Service, 2020). Arctic coasts are eroding at a mean annual rate of 0.5 m/a (Lantuit et al., 2013), leading to enhanced sediment input to nearshore areas. These sediments are likely to contain large amounts of carbon given the high organic matter content of coastal permafrost (Fritz et al., 2017). While the riverine influx of sediments to the Arctic Ocean has been quantified using *in-situ* and remote sensing data in several studies (Holmes et al., 2002), the sediment fluxes associated with coastal erosion are not well known. Recent research suggested that coastal erosion can be the main sediment contributor to Arctic nearshore areas outside large river deltas (Klein et al., 2019; Terhaar et al., 2021; Wegner et al., 2015).

Nearshore areas, defined as sea water shallower than 20 m along the coast (Fritz et al., 2017), remain understudied in Arctic Oceanography. This is mostly due to the traditional division of disciplines between terrestrial and marine science and the logistical challenges associated with measurements in shallow waters close to the shoreline. Yet, these areas play a crucial role in the carbon cycle: coastal erosion and resuspension cause a steady supply of carbon-rich material in surface waters, where they could be transformed to and released as greenhouse gases (Jong et al., 2020). Recent research indicated that Carbon burial in nearshore waters is rare due to constant wave induced resuspension (Jong et al., 2020). Little research has been conducted on the effects of coastal erosion on turbidity in Arctic coastal waters. Increases in turbidity are likely to impact primary production through reduced solar light penetration in the water column (Carmack and Wassmann, 2006), which could impact local food webs and eventually the subsistence economy of local people (Dunton et al., 2006).

Remote sensing has the potential to provide important insight into Arctic surface water geochemistry since it overcomes the problem of difficult accessibility of most field sites and is capable of covering large regions at a high frequency. Recent studies have shown the capability of ocean color remote sensing to study coastal waters (Groom et al., 2019), however, most studies focus on large river deltas (Constantin et al., 2017; Manzo et al., 2018) or use low spatial resolution imagery exclusively (Doxaran et al., 2012; Tang et al., 2013). Nearshore sediment flux analyses are less common, particularly in the Arctic.

Recent improvements in satellite borne optical instruments such as OLI onboard Landsat 8 and MSI onboard Sentinel 2 (Vanhellemont and Ruddick, 2014) and progress in atmospheric correction algorithms (Pahlevan et al., 2021; Vanhellemont and Ruddick, 2021, 2018) have opened new opportunities to resolve nearshore water characteristics at high spectral and spatial resolution. Nearshore waters are optically complex, as they are influenced by colored dissolved organic matter (cDOM), phytoplankton pigments, and suspended sediments, which makes remote sensing applications more error-prone.

Turbidity caused by suspended sediments is generally well correlated to the reflectance in the red to near-infrared (NIR) part of the electromagnetic spectrum (Munday and Alföldi, 1979), with the reflectance in the red part of the spectrum being more sensitive to low to intermediate turbidity values and the NIR reflectance being more sensitive to high turbidity values. Satellite based turbidity retrieval improved drastically with the introduction of semi-empirical relationships (Nechad et al., 2009). The most widely used semi-empirical turbidity algorithm was published by Dogliotti et al., 2015, where both red and NIR reflectances are used to cover a wide range of turbidity values. Validation data from multiple coastal sites located in the temperate to tropical parts of the Earth were used, with a strong focus on estuarine environments. Validation data from permafrost coasts is missing in this algorithm, even though permafrost coasts represent one third of the world's coastlines (Lantuit et al., 2013).

In this study, we calibrate and test the Arctic Nearshore Turbidity Algorithm (ANTA), an ocean color algorithm that directly relates water leaving reflectance to turbidity in Arctic surface nearshore waters. The goal of this study is to establish a robust turbidity-reflectance relationship which can adequately represent the complex nature of Arctic nearshore environments. *In-situ*

measurements of water leaving reflectance, turbidity, and suspended particulate matter (SPM) concentration were used to calibrate an algorithm for multiple satellite sensors that are currently used for nearshore turbidity retrieving (Landsat 8, Sentinel 2, and Sentinel 3). Match-up scenes of Sentinel 2 with *in-situ* samples from a separate test area were used to test the performance of the ANTA. This algorithm should serve as a multi-sensor turbidity algorithm that is specifically calibrated for an Arctic nearshore environment with the high potential to transfer it to other Arctic coastal waters for larger-scale applications.

3.3 METHODS

3.3.1 Regional setting

The tuning of the ANTA is based on *in-situ* measurements from the nearshore waters around Herschel Island Qikiqtaruk (HIQ), located at the Yukon coast in the western Canadian Arctic. *In-situ* samples taken at Adventfjorden in the western part of the Svalbard Archipelago were used as a test dataset to assess the transferability to other nearshore areas in the Arctic.

HIQ is surrounded by the Yukon Coast nearshore waters, which are part of the Canadian Beaufort Shelf (Figure 3-1). The Mackenzie River is the main freshwater source of the Canadian Beaufort Shelf (Hill et al., 1991). The Mackenzie freshet in May marks the beginning of the ice break-up at the shelf with a peak discharge of up to 35000 m³/s (O'Brien et al., 2006; Yang et al., 2015). Coastal erosion at HIQ occurs mostly during the open-water season, when the sea is not covered by ice, which typically spans from mid-June to late September (Solomon, 2005). However, single storm events can cause up to 43 % of annual coastal erosion in the area (Lim et al., 2020). Coastal permafrost along the Yukon Coast in this region is rich in buried organic material (total organic matter content: 4.7 wt%, Mackay, 1971; Tanski et al., 2017) and has high ice content, which occupies ~46 % of the ground volume, making it especially vulnerable to increasing air temperatures. Coastal morphology covers a wide range of features, from sandy beaches towards the South of the island, permafrost cliffs with heights up to 30 m towards the North and West of HIQ, and retrogressive thaw slumps, which are most common towards the SE (Obu et al., 2016). Sediments consist of mostly fine silt and clay particles, with varying amounts of sand (Fritz et al., 2012; Jong et al., 2020).

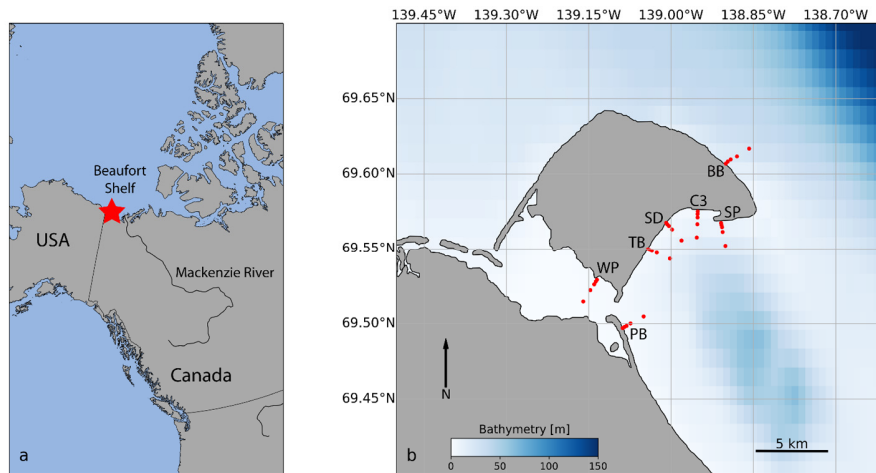


Figure 3-1 (a) Location of the study area on the Canadian Beaufort Shelf, near the northernmost border of Canada and the USA. (b) Close-up to Herschel Island Qikuqtaruk. Sampling transects during the 2019 field campaign are indicated by red dots.

The climate in the southern Beaufort Sea is characterized by long winters and short summers (Burn and Zhang, 2009). The predominant wind directions during the open water season are ESE and NW (Hill et al., 1991; Radosavljevic et al., 2015). During ESE wind conditions, the Mackenzie River plume has the potential to reach the nearshore waters of HIQ, which results in higher suspended sediment concentration and water temperatures (Klein et al., 2019). Wind direction and wind speed further influence hydrodynamics such as currents (Hill et al., 1991) and upwelling (Williams et al., 2006).

Adventfjorden is a small side-arm of Isfjorden in western Svalbard (Figure 3-2). This fjord has a partially glaciated catchment, and receives large inorganic sediment loads from several land-terminating glaciers during the melt season (from June-September), especially via the Longyearelva and Adventelva rivers (Nowak et al., 2019; Węśławski et al., 2011; Zajaczkowski and Włodarska-Kowalczyk, 2007). These river plumes, rich of inorganic sediment loads from a glacially-influenced catchment, provide a strong contrast from the organic-rich sediments and coastal erosion that are key features of the HIQ system. The climate at Svalbard is characterized by long, cold winters and short summers. The warm West Spitsbergen Current significantly increases air temperature in the western part of Svalbard, including Adventfjorden, enhancing

glacial melt during summer and thus sediment export to the fjord (Hanssen-Bauer et al., 2019; Nowak et al., 2019).

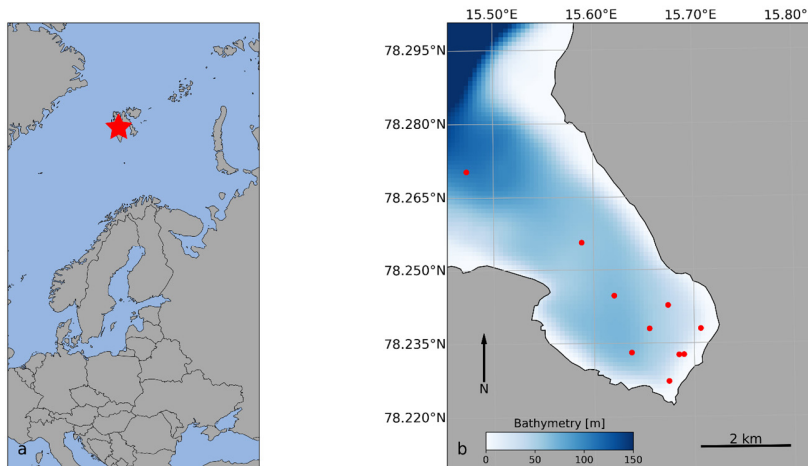


Figure 3-2 (a) Location of Adventfjorden, a small sidearm of the Isfjorden system on the west coast of Svalbard. (b) Close-up of Adventfjorden, with the sampling grid indicated by red dots.

3.3.2 *In-situ* sampling

In-situ samples of SPM concentration and turbidity measurements were collected around HIQ between July 29th and August 15th, 2018 and between July 30th and August 8th, 2019 (for detailed information, see supplementary information). Water leaving reflectance was only measured during summer season 2019. Samples were collected along transects perpendicular to the coastline of HIQ and the nearby Yukon coast (Figure 3-1). Each transect consisted of five individual sampling locations with distances of 50m, 250m, 500m, 1000m, and 2000m to the coastline, respectively. Samples were taken from onboard a Zodiac MKV HD. The transects were designed to resolve different types of nearshore morphologies and processes: transects PB and WP were influenced by longshore currents and adjacent lagoons; transects TB, SD, and C3 were located close to the outlets of retrogressive thaw slumps and creeks; and transects SP and BB were located in front of eroding permafrost cliffs (Figure 3-1).

SPM concentrations at each sampling location were calculated from three individual water samples, which were taken in 5 cm water depth in rinsed Nalgene 1L bottles. They were filtered

through pre-weighed Whatman GF/F 47 mm glass microfiber filters in field camp right after the sampling. The filters were dried at 50 °C in the laboratory for five days prior to re-weighing to calculate SPM concentrations. SPM concentrations were corrected for salt remnants based on the results presented by Neukermans et al., 2012. Turbidity was measured by taking a water sample in a 10 ml pre-rinsed glass vial at a water depth of 5 cm and analyzing it in a HACH 2100Qis turbidity meter. Duplicate samples were taken and measured at each sampling location and then averaged.

Water-leaving reflectance was measured above the water surface using two hyperspectral TriOS RAMSES radiometers, one of each measuring radiance (L , [$W/(m^2*sr)$]) and irradiance (E , [$W/(m^2)$]) in the spectral range of 350-950 nm at a spectral resolution of 4 nm. Each radiometric measurement sequence lasted for five minutes. While the downwelling sky-irradiance (E_D) was sampled throughout the complete five minutes pointing the zenith at the highest location of the coastal ship, the radiance was measured as total upwelling (L_U) and sky radiances (L_D), respectively, for 2 minutes each. Radiance measurements were taken in 135° relative to the solar zenith angle and in nadir/zenith angles of 40° (Mobley, 1999).

In-situ turbidity measurements in Adventfjorden were taken on June 14th, 2019, and August 8th, 2019, to match Sentinel 2 data acquisitions. 10 locations were sampled on both dates (Figure 3-2). Triplicate measurements were conducted using a Thermo-Eutech TN-100 turbidity meter.

3.3.3 Optical data processing

TriOS RAMSES measurements were analyzed according to Ruddick et al., 2006 and then used to calculate the remote sensing reflectance (R_{RS}) according to Mobley, 1999. Prior to the analysis, measurements were discarded if one of the following conditions was met: (i) the inclination in either x or y direction was larger than 5° ; (ii) either E_D , L_U or L_D differed by more than 25% at 550 nm to a neighboring scan; or (iii) spectra were incomplete due to a sensor malfunction (Ruddick et al., 2006). In total, measurements from 32 sampling locations met the quality requirements. Next, the first five consecutive scans of each E_D , L_U and L_D were used to calculate five separate instances of R_{RS} according to equation 6:

$$R_{RS}(\lambda) = \frac{L_U - \rho * L_D}{E_D} \quad (7)$$

The ρ value, which represents the sky radiance reflection, was set according to Mobley, 1999 depending on the cloud conditions during the sampling. The ρ value covers a range of 0.035 to 0.07, representing varying coverages of cumulus clouds at the horizon during the sampling. For one measurement, a ρ value of 0.13 was assigned due to the occurrence of a larger cloud band at the horizon. Additionally, a baseline correction was conducted for measurements that corresponded to low turbidity measurements as proposed in Knaeps et al., 2015, which was adopted to lower wavelengths. Briefly, the R_{RS} in wavelengths above 900 nm was assumed to be 0 if the turbidity measurement of the same location were below 10 FNU (Jain and Singh, 2003), and then used as baseline. The resulting five separate instances of R_{RS} were used to calculate means, medians, and standard deviations of R_{RS} . Hereafter, R_{RS} always refers to the mean value of the five separate instances of R_{RS} after skylight correction and baseline correction (if conducted). R_{RS} was converted to water leaving reflectance (R_w , $R_w = R_{RS} * \pi$) prior to relating it to surface turbidity (Figure 3-3).

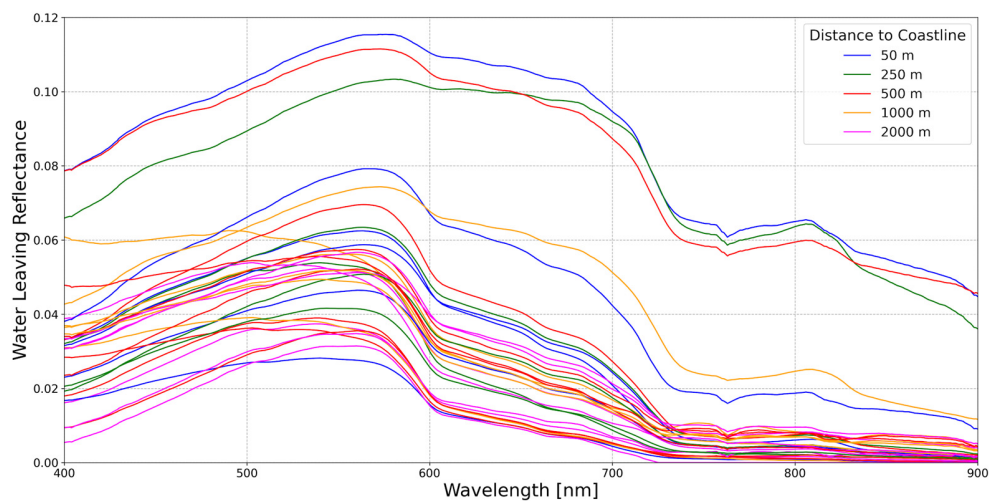


Figure 3-3 In-situ measured spectra of water leaving reflectance ($R_{RS} * \pi$) that were used for the calibration of the turbidity algorithm. Spectra were measured using two TriOS Ramses hyperspectral radiometers above the water surface.

3.3.4 Algorithm tuning

To create the ANTA based on multiple operating and historical satellite sensors, relative spectral response functions of Landsat 4/5 TM, 7 ETM+ and 8 OLI, Sentinel 2 MSI, MODIS Aqua, and Sentinel 3 OLCI were used as relative means to calculate a single R_{RS} value for each satellite sensor spectral band.

32 measurements of R_{RS} and turbidity from summer 2019 at HIQ were used to calibrate a reflectance-turbidity relationship based on Nechad et al., 2009 and Dogliotti et al., 2015. The general semi-empirical relationship in order to retrieve the turbidity ($T(\lambda)$) can be written as expressed in equation 5:

$$T(\text{red or NIR}) = \frac{A_T^\lambda \rho_W(\lambda)}{(1 - \rho_W(\lambda)/C_T^\lambda)} \quad [FNU] \quad (5)$$

where ρ_W is the water leaving reflectance (R_W) at wavelength λ , and A_T [FNU] and C_T being wavelength dependent constants. According to Dogliotti et al., 2015, $T(\text{red})$ was used if $R_W(\text{red}) < 0.05$ and $T(\text{NIR})$ if $R_W(\text{red}) > 0.07$, with a linear blending in the transition. The A and C parameters were calculated for $R_W(\text{red})$ and $R_W(\text{NIR})$ using non-linear least-square regression for each of the above named sensors (Table 3-1).

The performance of the ANTA was compared to the original semi-empirical turbidity algorithm presented in Dogliotti et al., 2015 by applying both algorithms to the dataset presented in chapter 2 that consists of 35 Scenes of the HIQ nearshore zone recorded by Landsat TM, ETM+ and OLI between 1986 and 2016. The 35 scenes were grouped based on their prevailing wind conditions (changing winds, NW, and ESE, Klein et al., 2019) to calculate mean turbidity per used algorithm and wind condition.

3.3.5 Satellite imagery processing

In this study, four scenes recorded on June 21, 2019 within 76 minutes, one of each taken by Landsat 8, Sentinel 2A, Sentinel 3A, and Sentinel 3B were compared to analyze the performance of the turbidity-reflectance relationship applied to the different satellite sensors. These scenes

were chosen because this was the only time during the 2019 summer season when all 4 sensors recorded a scene of HIQ within this short time difference.

Table 3-1 Calibration coefficients A [FNU] and C for multiple operative and historical satellite sensors to be used in their respective red and NIR wavelength spectral bands. Coefficients published by Dogliotti et al., 2015 and Nechad et al., 2016 are given as reference

Sensor	Wavelength	Center Wavelength [nm]	A [FNU]	C
Landsat 4/5 TM	red	660	283.43	0.1395
	NIR	839	1528.7	0.2124
Landsat 7 (ETM+)	red	661	282.54	0.1395
	NIR	835	1546.7	0.2119
Landsat 8 (OLI)	red	655	268.61	0.1401
	NIR	865	2159.3	0.2093
Sentinel 2 (MSI)	red	665	288.95	0.1395
	NIR	865	1830.7	0.2033
Sentinel 3 (OLCI)	red	665	221.03	0.1233
	NIR	865	1613.0	0.1638
MODIS Aqua	red	659	260.15	0.1396
	NIR	865	1760.1	0.205
MODIS (Dogliotti et al. 2015)	red		228.1	0.1641
	NIR		3078.9	0.2112
Landsat 8 (Nechad et al. 2016)	red		526.82	0.2365
	NIR		3031.7	0.2114

To test the ANTA, two scenes were used which correspond to match-up *in-situ* measurements of turbidity in Adventfjorden, Svalbard. One scene was recorded on June 14 by Sentinel 2A and one on August 8, 2019 by Sentinel 2B. Match-up scenes for Landsat 8 are not available, and the spatial resolution of Sentinel 3 is not sufficient to resolve the small-scale sampling grid (Figure 3-2).

Landsat imagery was downloaded from the United States Geological Service (USGS) Earth Explorer as L1T product, which means with georeferencing but without atmospheric correction. Sentinel 2 and Sentinel 3 imagery was downloaded from the European Space Agency (ESA) Copernicus Hub as Level1C product. Atmospheric correction towards water leaving reflectance (R_w) was performed using the ACOLITE software version 20210114.0 (Landsat 8 and Sentinel

2, Vanhellemont, 2019; Vanhellemont and Ruddick, 2018) and the ACOLITE software version 20210421.0 (Sentinel 3, Generic Public Beta, Vanhellemont and Ruddick, 2021) applying the dark spectrum fitting algorithm, which was found to perform best in coastal environments (Renosh et al., 2020; Vanhellemont and Ruddick, 2021).

Table 3-2 Specifications of the used satellite imagery

Satellite	Date	Time (UTC)	Identifier
Sentinel 3B	June 21st, 2019	19:59	0179_026_356_1800_MAR_O_NT
Sentinel 3A	June 21st, 2019	20:39	0179_046_114_1800_MAR_O_NT
Landsat 8	June 21st, 2019	20:58	LC80670112019172LGN00
Sentinel 2A	June 21st, 2019	21:15	N0207_R143_T07WET

3.4 RESULTS AND DISCUSSION

3.4.1 Turbidity and SPM

The values of *in-situ* turbidity in the nearshore area varied from 0.83 FNU to 176 FNU, with a mean value of 15.95 FNU and a median of 5.02 FNU. SPM values taken at the same location varied from 6.2 g/m³ to 190.2 g/m³, with a mean value of 26.1 g/m³ and a median of 16.61 g/m³. The strong relation between turbidity and SPM concentration is linear ($R^2 = 0.93$, Figure 3-4). Each of the measured transects (Figure 3-1) showed highest turbidity and SPM close to the coast, where the influence of coastal erosion and resuspension is highest. Figure 3-4 reveals that SPM concentrations below 10 g/m³ are only rarely measured, as well as turbidity being higher than the SPM measurement from the same location.

The linearity of this relationship was expected, as turbidity is defined as the measurement of light scattering, which is caused by suspended material (ISO 7027), and is similar to recently reported results from various regions on earth (Jafar-Sidik et al., 2017; Sent, 2020; Xue et al., 2019) that show the almost linear relationship between backscatter measurements and sediment. The offset towards SPM concentrations, however, has only rarely been reported in the literature. Bhargava and Mariam, 1990 reproduced a similar result during a lab experiment. It is shown that the turbidity of suspended clay samples stays relatively low with increasing SPM

concentrations. The authors identify organic content as the main damping factor for turbidity, which also darkens the sediment. This matches recent field observations: water that is strongly affected by release of particulate organic matter (POC) and dissolved organic matter (DOC) from permafrost are brown-yellowish. This is caused by the dominance of light absorption by non-algal-particles (aNAP) and colored dissolved organic matter (aCDOM). The fraction of organic matter (OC) that is released in its particulate fraction (POC) is substantially higher from coastal erosion compared to riverine transport, where most of the OC is released as dissolved organic carbon (Gordeev and Kravchishina, 2009; McClelland et al., 2016).

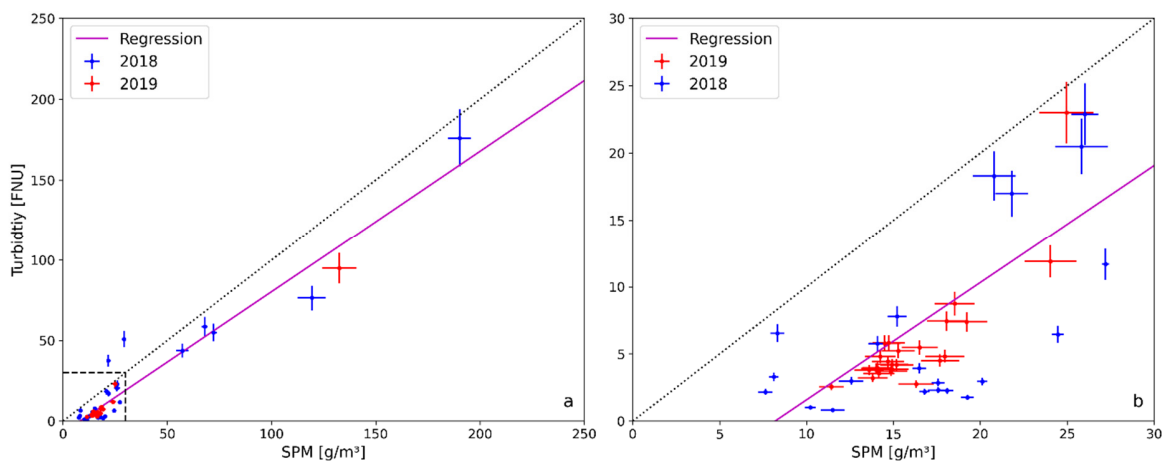


Figure 3-4 (a) Turbidity and SPM measurements from 2018 and 2019 including error bars and (b) zoom into the lower value range. The turbidity error was assigned to 10 % of the measurement, which is the margin of error of the turbidity meter as provided by the manufacturer. SPM error was calculated as the standard deviation of triplicate samples.

3.4.2 ANTA performance

The application of the ANTA reveals both a high sensitivity towards low and high turbidity features for all tested sensors (Figure 3-5). Generally, the retrieved values using the Landsat 8 (Figure 3-5 a) and Sentinel 2 (Figure 3-5 b) imagery are higher than for using the Sentinel 3 imagery (Figure 3-5 c and Figure 3-5 d), which is mainly caused by the differences in spatial resolution (30m, 20m, and 300m, respectively). All sensors resolve the highest turbidity values close to the shoreline of HIQ in their respective result image, with values above 150 FNU modelled at the NE coast of HIQ for Landsat 8 and Sentinel 2.

Both Landsat 8 and Sentinel 2 are able to resolve a narrow band of high turbidity in the direct vicinity of the HIQ coastline, especially along the NE and NW coast. This band of high turbidity is caused by high erosional input from the adjacent permafrost cliffs, which are exposed to the maximum wave energy, as well as longshore sediment transport during ESE wind conditions. Recent research (Klein et al., 2019) has identified a broad band of high turbidity around the whole island, independent from the wind forcing. The high turbidity band is narrower than reported in chapter 2, which might be due to an earlier recording of the imagery in this study; most data used in chapter 2 was recorded in July and August, when temperatures and thus thermo-erosion are usually higher. This is in line with recent modelling approaches (Nielsen et al., 2020; Rolph et al., 2021), which identify thermal forcing through increasing air and water temperature as the main driver of coastal erosion along permafrost coasts. This in turn has the potential to release large amounts of greenhouse gases to the atmosphere (Tanski et al., 2021), further enhancing climate warming.

For turbidity values below 10 FNU, turbidity values retrieved by Landsat 8 satellite imagery are lower than the Sentinel 2 retrieved turbidity (Figure 3-6), which gets closer to the collected field data. However, even Landsat 8 is unable to reflect the lowest *in-situ* turbidity, which were between 2 and 4 FNU during the whole summer season (see supplementary data for more information). As a result, Landsat 8 retrieved turbidity has a higher contrast for higher turbidity values (above 10 FNU), which is an asset when it comes to the identification of sediment ejections towards the offshore, sediment pathways, and filaments.

Sediment ejections towards offshore waters are most prominent along the NE and SE coasts of the island. The feature along the NE coast is most likely caused by upwelling, which is very common in this area (Williams et al., 2006). Colder and nutrient rich water from outside the Canadian Beaufort Shelf rises to the ocean surface N of HIQ, and the Coriolis Force directs the sediment rich longshore current towards the offshore. The observation of sediment ejection along the SE coast of HIQ is in line with the occurrence of high sediment producing erosional features, such as the largest creek of the island, and retrogressive thaw slumps (Lantuit and Pollard, 2008; Obu et al., 2016). These features are not permanent, but are caused by extreme events, when increased air temperatures lead to higher thermo-erosion of the coastal permafrost

(Weege, 2016). Turbid filaments are also resolved along the Yukon coast, best visible SE of HIQ.

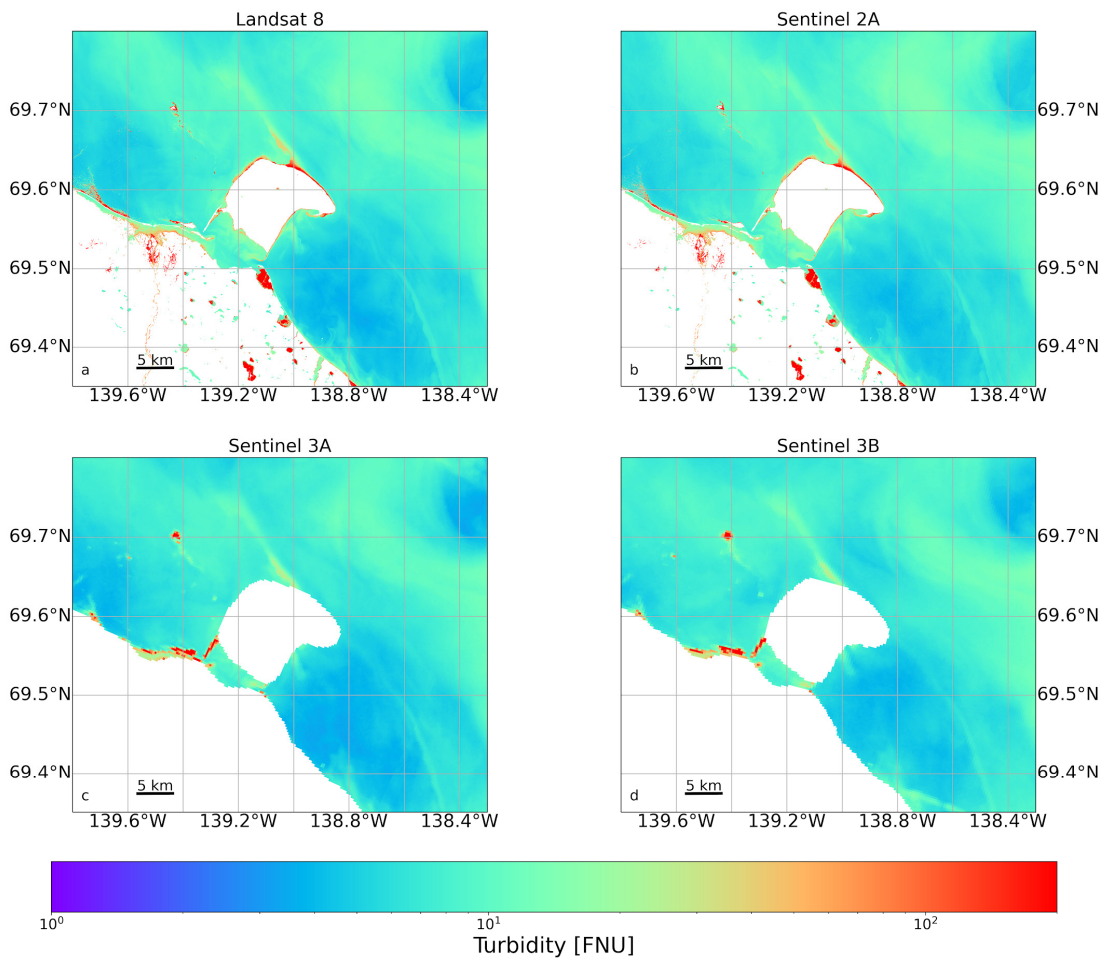


Figure 3-5 Application of the ANTA to different satellite data recorded at June 19th, 2019 (Table 3-2): (a) Landsat 8, (b) Sentinel 2A, (c) Sentinel 3A, (d) Sentinel 3B.

Sentinel 3A and Sentinel 3B retrieved turbidity values differ from those retrieved using Landsat 8 and Sentinel 2 data substantially due to their lower spatial but higher spectral and temporal resolution. Due to their high spatial resolution, Sentinel 2 and Landsat 8 were able to resolve small scale features of turbid filaments in the nearshore zone around Herschel Island. The spatial resolution of Sentinel 3 (300m) is not sufficient to resolve these features (Figure 3-5 c and Figure 3-5 d). However, this is not true for the sediment ejection features along the NE and SE coast of

HIQ. Besides the turbulent nearshore waters in direct vicinity of the coastline, both Sentinel 3A and 3B derived turbidity resolves a similar range of turbidity as Landsat 8.

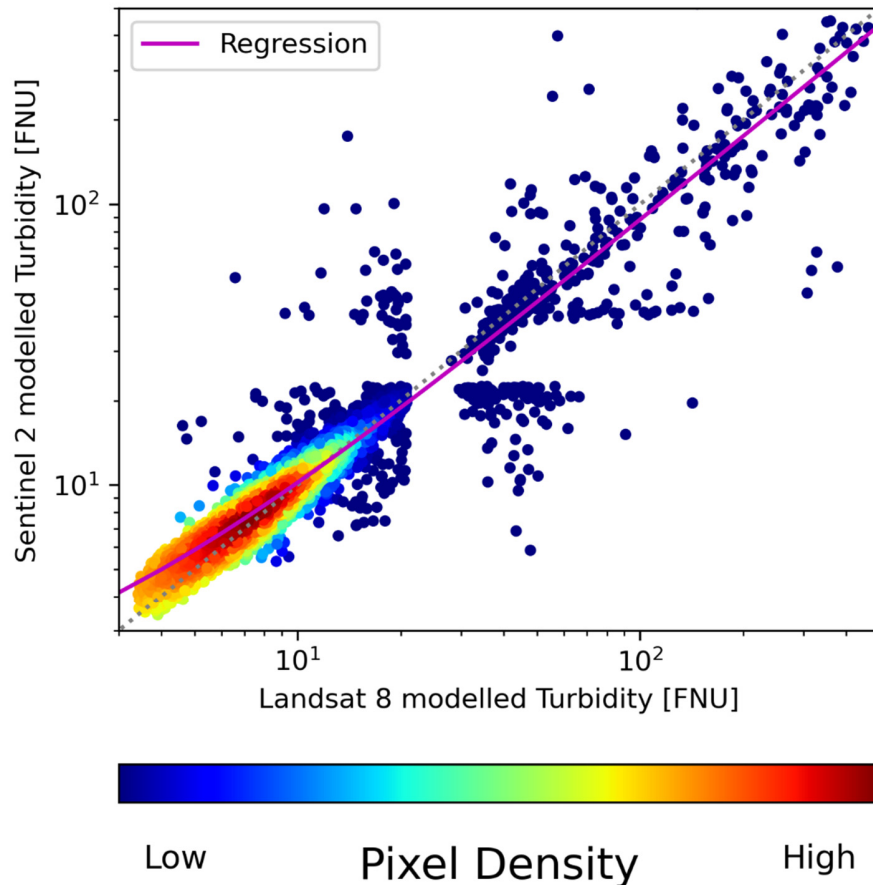


Figure 3-6 Scatterplot between Landsat 8 and Sentinel 2 derived turbidity. 3000 randomly generated points in the extent of Figures 5 a and b (excluding land areas) were used for the comparison. The regression line is linear ($R^2=0.89$, $y=0.87x + 1.94$) and shows the overestimation of Sentinel 2 derived turbidity below 10 FNU.

3.4.3 Comparison with the Dogliotti et al., 2015 algorithm

The performance of the ANTA was compared to the widely applied semi-empirical relationship presented in Dogliotti et al., 2015 (Figure 3-7). A general comparison reveals substantial differences, which includes higher sensitivity towards low turbidity values (best visible in Figure 3-7 e), and an overestimation of intermediate turbidity values (20-50 FNU, best visible in Figure 3-7 f). The largest differences are resolved in the comparison of the NW wind situation

(Figure 3-7 b and Figure 3-7 e). The ANTA is able to resolve turbidity values below 2 FNU towards the N and W of HIQ, which the Dogliotti et al., 2015 algorithm is not able to (Figure 3-8 b). Additionally, longshore drift features towards the SE, which are well resolved in Figure 3-7 e, are not resolved at all in Figure 3-7 b. The scatterplot comparing both images (Figure 3-8 b) supports these observations. The lowest turbidity values are overestimated by the Dogliotti et al., 2015 algorithm. In the current study, the majority of data points fall within the range of 5 - 8 FNU, which both algorithms resolve similarly.

During ESE wind conditions, the general patterns of longshore drift towards NW is resolved by both algorithms (Figure 3-7 c and Figure 3-7 f). In the Dogliotti et al., 2015 algorithm (Figure 3-7 c), turbidity values are higher in the immediate vicinity of the coastline, but decrease more rapidly to values of approximately 10 FNU compared to the ANTA (Figure 3-7 f). Along the NE coast of HIQ, the ANTA resolves sediment pathways towards the offshore, which are not resolved in the Dogliotti et al., 2015 algorithm. The ANTA resolves a filament of increased turbidity NE of HIQ, which indicates external influences, most likely by the Mackenzie River. Sediment ejections due to larger erosional events along the SE coast of HIQ are resolved by both models. The Dogliotti et al., 2015 algorithm indicates longshore drift through the Workboat Passage between HIQ and the Yukon main land towards the NW, which is not resolved in the ANTA (Figure 3-7 f). The scatterplot in Figure 3-8c shows similar patterns as in figure 8b: lowest turbidity values are modeled higher in the Dogliotti et al., 2015 algorithm, which changes with increasing turbidity. Turbidity values between 10 - 40 FNU are modeled higher by the ANTA, while values around 100 FNU and above are modeled similarly by both algorithms.

During changing wind conditions (Figure 3-7 a and Figure 3-7 d), both algorithms resolve a mixture of the features which are also well- captured during NW and ESE wind conditions. The ANTA resolves a near-circular filament feature ranging from the W to the NE coast of HIQ, as well as two sediment pathways offshore along the NE coast (Figure 3-7 d), both of which tend to disappear in Figure 3-7 a. The ANTA also resolves an eddy-like feature S of HIQ. The scatterplot comparing the two algorithms (Figure 3-8 a) reveals remarkably higher turbidity values modeled by the Dogliotti et al., 2015 algorithm when the ANTA modeled values ~ 3 - 5 FNU. Turbidity values between 10 - 30 FNU modeled by the ANTA are nearly exclusively

modeled below 10 FNU by the Dogliotti et al., 2015 algorithm, showing similar patterns like in Figure 3-8 c.

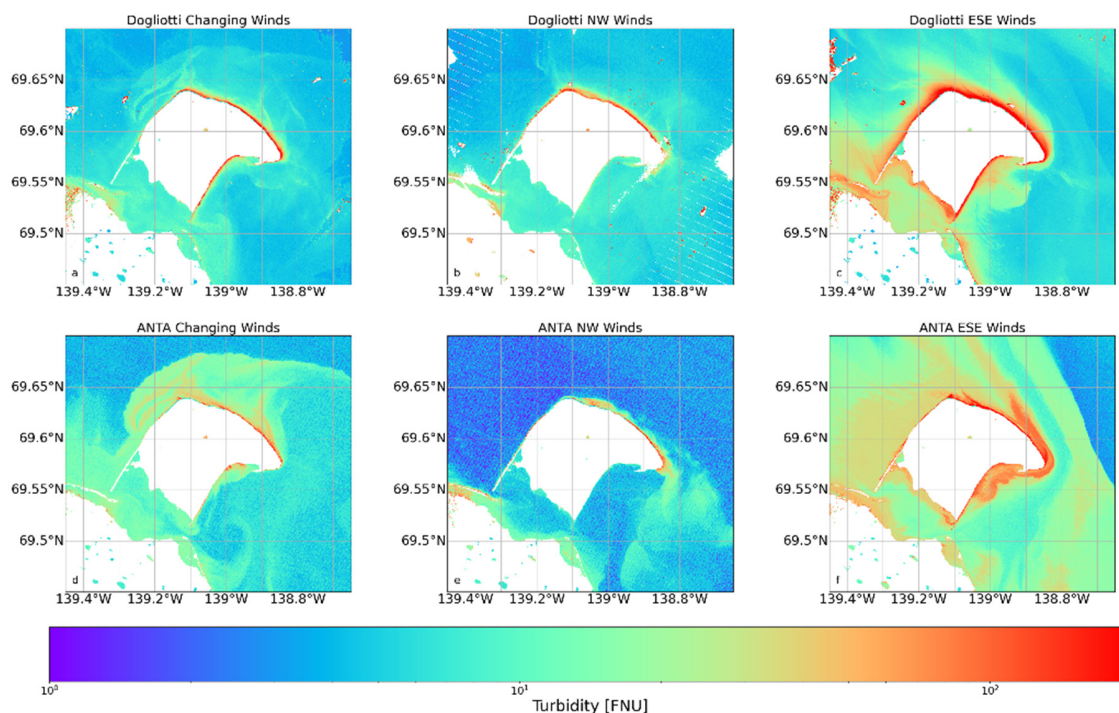


Figure 3-7 Comparison of the ANTA to the results presented in Klein et al., (2019) applying the Dogliotti et al., (2015) algorithm

Comparing the data to field observations from 2018 and 2019, where turbidity values were frequently below 5 FNU, the ANTA has a superior performance in resolving turbidity values this low. The Dogliotti et al., 2015 algorithm models higher turbidity values above 200 FNU compared to the ANTA, which is remarkably higher than each measurement taken during the two summer seasons. Based on this comparison, the ANTA shows the best performance in the low- to intermediate turbidity values (below 50 FNU), when identifying filaments of higher turbidity and sediment pathways along- or offshore.

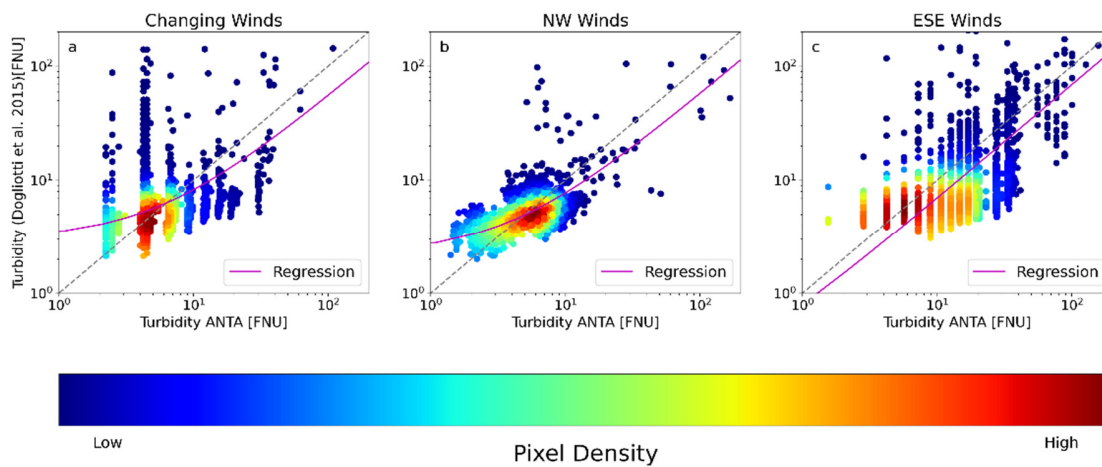


Figure 3-8 Scatterplot comparing the different turbidity algorithms shown in Figure 7.

3.4.4 Test and transfer of the ANTA

In-situ surface turbidity data from Adventfjorden were used as test data to evaluate the performance of the ANTA developed for the HIQ nearshore area for another nearshore Arctic coastal area. Figure 3-9 shows that the ANTA is capable of resolving both low and high turbidity values. Sediment pathways and filaments of high turbidity are well resolved close to the river outlet in the SE part of Adventfjorden, as well as in the NW towards Isfjorden. The results reveal that lowest turbidity values (up to ~ 10 FNU) are typically overestimated (Figure 3-10), which is similar to the results obtained from the HIQ imagery. This feature is related to the Sentinel 2 sensor design: it was designed to focus on land applications and the reflectance over low-turbidity waters are much lower than over land. Values between 10 and 50 FNU are accurately retrieved, while higher values are overestimated, which may reflect the much higher inorganic contribution to the SPM in Adventfjorden compared to HIQ. The ANTA performs reasonably well considering the strong differences in sediment composition between HIQ and Adventfjorden. During the summer melt season, suspended sediments in Adventfjorden are primarily delivered by rivers fed by land-terminating glaciers, leading to a high inorganic contribution to the SPM, and distinct river plumes extending into the fjord (Zajaczkowski and Włodarska-Kowalczyk, 2007). The good performance of the ANTA at this contrasting site may in part reflect the fact that the test data were collected in early and late summer, outside of the

period of highest glacial melt, and where SPM often includes a higher contribution of organic matter (Walch, 2021, Poste *unpublished data*).

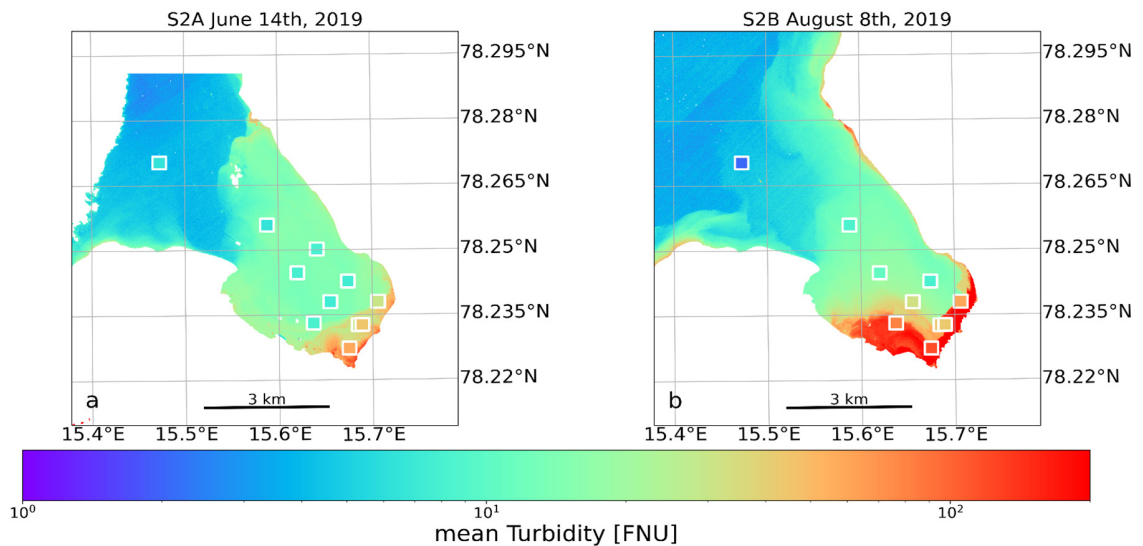


Figure 3-9 Application of the ANTA to Sentinel 2 imagery in Adventfjorden with in-situ turbidity measurements from the FreshFate sampling plotted in squares

Given that the environmental conditions in Adventfjorden differ strongly from those at HIQ, the algorithm performs reasonably well. As Adventfjorden is influenced by glacial discharge, the fjord receives larger freshwater input than the HIQ nearshore waters (Nowak et al., 2019). Together with the different optical properties of inorganic suspended material in contrast to the organic rich material at HIQ (Gould et al., 2002), the ANTA proved to be robust and transferable. This suggests at least some degree of applicability of the ANTA algorithm for Arctic nearshore environments beyond HIQ. However, it is noted that the ANTA should be used with caution in environments with high freshwater input such as river deltas or glacial influenced areas during maximum melt season in summer, as they might add a higher level of optical complexity (Aurin and Dierssen, 2012), which the ANTA might not reflect accurately. The best performance is expected close to strongly eroding permafrost coasts with high organic carbon content, where conditions are likely to be more similar to those at HIQ.

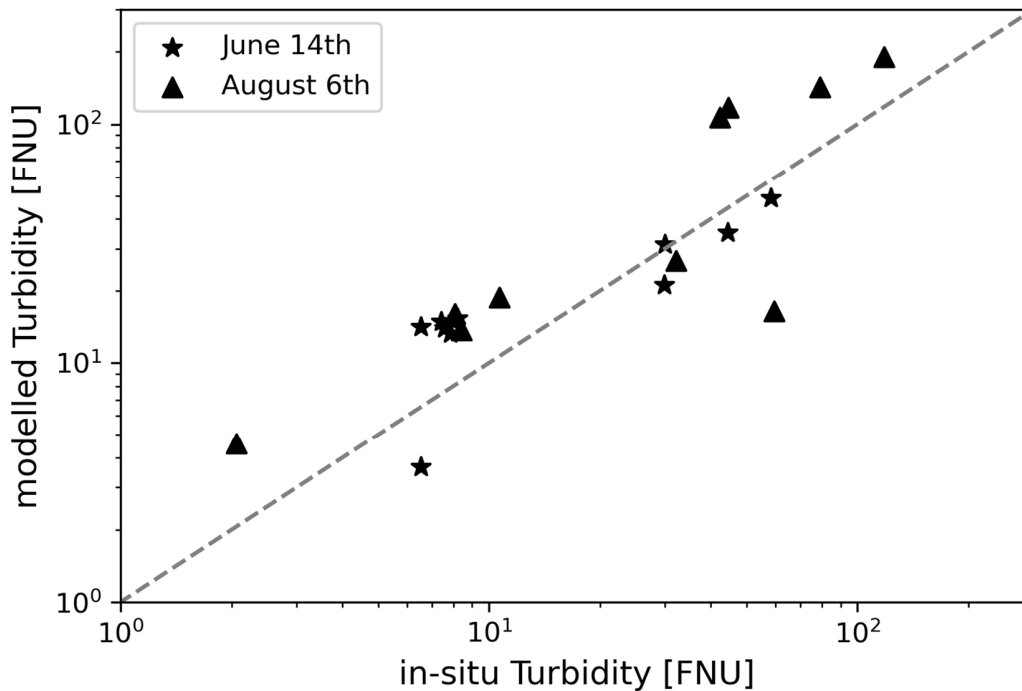


Figure 3-10 Scatterplot comparing *in-situ* turbidity sampled in Adventfjord and Sentinel 2 derived turbidity values (ANTA)

3.5 CONCLUSION

The aim of this study was to improve nearshore satellite-based turbidity retrieval in Arctic nearshore environments. Therefore, *in-situ* measurements of turbidity, SPM concentration and water-leaving reflectance, collected in summer seasons 2018 and 2019 around Herschel Island Qikiqtaruk were used to calibrate the Arctic Nearshore Turbidity Algorithm (ANTA), a multi-sensor turbidity-reflectance relationship. The application of the ANTA to multiple operating sensors showed satisfactory results, improving on the Dogliotti et al., 2015 general algorithm for Arctic nearshore waters. Improvements included high sensitivity towards both low and high turbidity values, as well as resolving sediment pathways and filaments. Landsat 8 showed best capability to resolve turbid filaments and sediment pathways due to its higher sensitivity towards low turbidity values compared to Sentinel 2 and higher spatial resolution compared to Sentinel 3.

The ANTA was applied to Sentinel 2 imagery from Adventfjorden in Svalbard to assess its performance outside the Canadian Beaufort Sea, where the calibration data was collected. Despite strong differences in sources and distribution of suspended sediments between these sites, with Adventfjord being impacted by higher freshwater and inorganic sediment inputs from land-terminating glaciers, the ANTA proved to be robust and transferable. However, future research has to focus on the influence of the SPM particle size distribution and composition on the ANTA, and on the influence of organic content. Since high cDOM concentrations generally correlate with high freshwater input, it is recommended to use the turbidity algorithm with caution in the vicinity of large river deltas. The best performance is expected close to strongly eroding coasts with high organic matter content, where conditions are likely to be comparable to Herschel Island Qikiqtaruk, where the calibration data was collected. Comparing the ANTA to the widely used algorithm published by Dogliotti et al., 2015, higher detail was resolved in the nearshore area of Herschel Island Qikiqtaruk and shows the potential of this tuned algorithm for arctic nearshore waters.

In this study, the first turbidity-reflectance relationship specifically calibrated to Arctic nearshore environments is presented. It can be applied to a series of operating and historic satellite sensors. It is shown that improvements were made for identifying turbid filaments and sediment pathways along- and offshore when comparing it to globally used turbidity algorithms. The applicability of the ANTA in other Arctic nearshore environments was also clearly demonstrated, however, careful verification of the results is recommended due to scarce validation dataset availability.

As the Arctic will continue to be impacted by global climate change, coastal erosion and river sediment input to the nearshore zone will rise, too. Future implementations of chlorophyll or particulate organic carbon measurements will help to estimate the Carbon and nutrient supply of coastal erosion to Arctic nearshore waters. The implementation of machine-learning based data analysis will improve the efficiency of the algorithm. Additional pan-Arctic sampling campaigns and comparative studies could help strengthen the algorithm by increasing its accuracy in a variety of different settings.

Funding

This publication is part of the Nunataryuk project. The project has received funding under the European Union’s Horizon 2020 Research and Innovation Program under grant agreement no. 773421. K.P.K. was financially supported by a Ph.D. stipend by the University of Potsdam (PoGS Potsdam Graduate School) and a short-term stipend by the German Academic Exchange Service (DAAD). I.N. was funded by the HGF AI-CORE, ESA CCI+ Permafrost, and NSF Permafrost Discovery Gateway (NSF Grants #2052107 and #1927872) projects. BJ was funded by the European Space Agency (ESA) as part of the Climate Change Initiative (CCI) fellowship (ESA ESRIN/Contract No. 4000133761/21/I-NB). The work in Adventfjord was supported by the Research Council of Norway (‘TerrACE’ project; project number 268458), and the Fram Center for High North Research “Fjord and Coast” flagship (‘FreshFate’ project; project number 132019).

Acknowledgments

USGS and NASA are acknowledged for Landsat imagery. ESA is acknowledged for Sentinel 2 and 3 imagery. We thank Bernard Gentili for his help when processing TriOS RAMSES data and Maeve McGovern for his involvement in field and lab work in Adventfjord. We acknowledge the support of Deutsche Forschungsgemeinschaft (German Research Foundation) and Open Access Publication Fund of University of Potsdam.

4 DRIVERS OF TURBIDITY AND ITS SEASONAL VARIABILITY IN THE NEARSHORE ZONE OF HERSCHEL ISLAND QIKIQTARUK (WESTERN CANADIAN ARCTIC)

4.1 ABSTRACT

The Arctic is greatly affected by climate change. The increase in air temperature drives permafrost thaw and an increase in coastal erosion and river discharge. This leads to a greater input of sediment and organic matter into coastal waters, substantially impacting the ecosystems by reducing light transmission through the water column and altering biogeochemistry. This potentially results in impacts on the subsistence economy of local people as well as the climate due to the transformation of suspended organic matter into greenhouse gases. Even though the impacts of increased suspended sediment concentrations and turbidity in the Arctic nearshore zone are well studied, the mechanisms underpinning this increase are largely unknown. Wave energy and tides drive the level of turbidity in the temperate and tropical parts of the world, and this is generally assumed to also be the case in the Arctic. However, the tidal range is considerably lower in the Arctic, and processes related to the occurrence of permafrost have the potential to greatly contribute to nearshore turbidity. In this study, we use high resolution satellite imagery alongside *in-situ* and ERA5 reanalysis data of ocean and climate variables in order to identify the drivers of nearshore turbidity, along with its seasonal variability in the nearshore waters of Herschel Island Qikiqtaruk, in the western Canadian Arctic. Nearshore turbidity correlates well to wind direction, wind speed, significant wave height, and wave period. Nearshore turbidity is superiorly correlated to wind speed at the Beaufort Shelf compared to *in-situ* measurements at Herschel Island Qikiqtaruk, showing that nearshore turbidity, albeit being of limited spatial extent, gets influenced by large-scale weather and ocean phenomenon's. We show that, in contrast to the temperate and tropical ocean, freshly eroded

material is the predominant driver of nearshore turbidity in the Arctic, rather than resuspension, which is caused by the vulnerability of permafrost coasts to thermo-erosion.

4.2 INTRODUCTION

Climate change is stronger in the Arctic than anywhere else on Earth (Box et al., 2019; Serreze and Barry, 2011). It affects the biophysical system in multiple ways: intensified permafrost thaw (Biskaborn et al., 2019), increased river discharge (McClelland et al., 2016), and intensified coastal erosion (Fritz et al., 2017). Permafrost coasts are especially vulnerable to increasing air temperatures, as frozen sediments can thaw and provide lower resistance against physical erosion such as wave erosion (Lantuit and Pollard, 2008; McGillivray et al., 1993). This has the potential to release the vast pools of organic matter, which are stored in permafrost (Tank et al., 2018), to release carbon and nutrients to nearshore waters (Fritz et al., 2017), or to directly emit greenhouse gases into the atmosphere (Romanovsky et al., 2010; Tanski et al., 2019; Vonk et al., 2012).

Arctic nearshore areas, defined as sea water shallower than 20 m along coastlines (Fritz et al., 2017), have witnessed increased sediment input from river discharge and coastal erosion over the past decades (Déry et al., 2009; Jones et al., 2009; McClelland et al., 2006). Permafrost coasts in the Arctic are eroding at a mean annual rate of 0.5 m/a (Lantuit et al., 2013). This leads to high sediment loads in the nearshore zone, which likely contain large amounts of carbon given the high organic matter content of coastal permafrost (Fritz et al., 2017). Sediment fluxes from coastal erosion in the Arctic are not well known due to limited accessibility of most Arctic study sites. The few studies attempting to calculate sediment and carbon fluxes from coastal erosion to the Arctic Ocean report fluxes of ~430 Tg sediment per year and 4.9 - 46.54 Tg carbon per year (Lantuit et al., 2013; Terhaar et al., 2021; Wegner et al., 2015).

Upon entering the nearshore waters, sediment and organic matter get exposed to a multitude of processes. Carbon rich suspended sediments could be transformed to greenhouse gases and transferred to the atmosphere (Jong et al., 2020). Coastal erosion, resuspension, and longshore sediment transport cause a regular supply of carbon-rich sediments in surface waters. Despite this relevance, nearshore zones remain understudied in Arctic Oceanography (Fritz et al., 2017).

High suspended sediment loads increase water turbidity, which reduces light penetration in the water column (Carmack and Wassmann, 2006). This, in turn, will likely reduce primary production, which impacts local food webs and eventually the subsistence economy of local people (Mangan et al., 2020). All these processes have been considered in isolation, but there is limited understanding of their interplay in nearshore waters, which is detrimental to the compilation of comprehensive biogeochemical budgets for the nearshore zone.

The drivers of nearshore turbidity are generally assumed to be wave energy and tides, which cause resuspension of sediments (Cartwright et al., 2021). However, these assumptions were made in the temperate and tropical oceans. Tidal range in the Arctic is generally lower than in most parts of the world's ocean (Kulikov et al., 2018), and wave heights are also generally lower in the Arctic Ocean due to reduced fetch lengths caused by sea-ice (Lantuit et al., 2013; Thomson and Rogers, 2014). Despite those factors, sediment load is extraordinarily high in Arctic coastal and nearshore waters (Klein et al., 2019), because of low water depths of the Arctic shelves and high terrestrial sediment supply. We therefore hypothesize that the drivers of nearshore turbidity in the Arctic nearshore zone go beyond waves and tides.

The absence of infrastructure to document the potential multitude of processes driving turbidity has hampered the ability to provide an Arctic-specific quantitative understanding of the link between processes other than tides and waves with turbidity. Remote sensing plays a crucial role for regional turbidity observations because it provides the spatial and temporal coverage needed to link turbidity to a wide range of environmental drivers. Turbidity caused by suspended sediments generally shows a high correlation to the water-leaving reflectance in the red and near-infrared (NIR) parts of the electromagnetic spectrum (Munday and Alföldi, 1979). Semi-empirical algorithms to relate turbidity from water-leaving reflectance have been widely used during the past decade (Dogliotti et al., 2015; Nechad et al., 2009), and were even validated for the Arctic nearshore zone recently (Klein et al., 2021). Remotely sensed turbidity retrieval is still limited by the availability of cloud free images, especially in the Arctic, where the Ocean is covered by ice for 8 months of the year.

In this study, we use high resolution satellite imagery, which covers most parts of the 2019 summer season at Herschel Island Qikiqtaruk in the western Canadian Arctic, to identify and

analyze seasonal variations of nearshore turbidity. ERA5 ocean and climate variables were used together with *in-situ* measurements to identify drivers and influences on nearshore turbidity.

4.3 METHODS

4.3.1 Study Area

The focus regions of this study are the coastal and nearshore waters around Herschel Island Qikiqtaruk (HIQ) on the Canadian Beaufort Shelf (Figure 4-1). The Mackenzie River is the main freshwater source of the shelf with a maximum discharge of 35000 m³/s during its freshet in May (Hill et al., 1991; O'Brien et al., 2006; Yang et al., 2015). Coastal erosion and the associated sediment supply to the nearshore zone is limited to the open water season, the part of the year when the ocean is not covered by ice, which generally spans from mid-June to the end of September (Solomon, 2005). Permafrost along the Yukon Coast has a high ice content (Mackay, 1971), making it especially vulnerable to increasing air temperatures, and is rich in buried organic material (Tanski et al., 2017). Climate in the southern Beaufort Sea is characterized by long, cold winters, and short summers (Burn and Zhang, 2009). Winds predominantly blow from ESE and NW directions (Radosavljevic et al., 2015). Wind direction and wind speed have the potential to influence hydrodynamics such as currents (Hill et al., 1991) and upwelling (Williams et al., 2006).

4.3.2 Satellite Imagery

In this study, satellite images recorded by Landsat 7, Landsat 8 and Sentinel 2 during the open-water season 2019 were used to map turbidity in space and time. Landsat imagery was downloaded from the United States Geological Survey (USGS) Earth Explorer as level 1T product. Sentinel 2 imagery was downloaded as level 1C product from the European Space Agency (ESA) SciHub. Atmospheric correction towards water-leaving reflectance was performed using the ACOLITE software version 20210114.0 (Vanhellemont, 2019; Vanhellemont and Ruddick, 2021), and the dark spectrum fitting algorithm was applied. To relate turbidity from water-leaving reflectance, the Arctic Nearshore Turbidity Algorithm (ANTA, Klein et al., 2021) was applied to each scene.

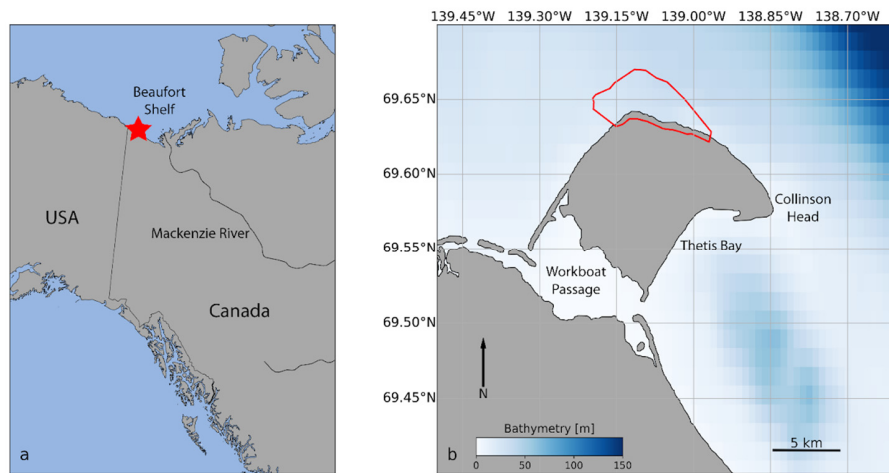


Figure 4-1 (a) Location of the study area close to the northernmost border of Canada and the USA. (b) Herschel Island Qikiqtaruk, located on the Canadian Beaufort Shelf. The area of interest is highlighted in red.

Based on the results presented in chapter 3, an area of increased turbidity along the N and NW coast of HIQ was identified (red area in Figure 4-1 b). These areas are expected to contain large amounts of eroded sediment, potentially holding large amounts of organic matter. This makes these areas especially important to monitor, as they have the largest impact regarding climate warming. For each scene, the average turbidity within this area of interest was calculated and related to the daily averages of the external influences.

4.3.3 *In-situ* data

In-situ measurements from the weather station on HIQ (69.5 °N, 139.25 °W) were downloaded from Environment Canada weather archive (<https://climate.weather.gc.ca>). Downloaded parameters were air temperature, wind speed, and wind direction for the time period between June 1 and September 30, 2019. Data at the weather station was recorded in hourly intervals. Mean values were assigned to each satellite image using the 24 measurements prior to 15:00, in order to correspond with the satellite imagery, which was also recorded at 15:00. Daily discharge data from the Mackenzie River at Arctic Red River was acquired as preliminary data from Environment and Climate Change Canada (ECCC).

4.3.4 Reanalysis data

ERA5 is the fifth generation of reanalysis datasets from ECMWF, using an advanced 4D-var data assimilation scheme (Hersbach et al., 2018). The variables used are air temperature, wind speed, wind direction, sea ice concentration, and sea surface temperature, which are all at an hourly temporal resolution and a spatial resolution of approximately 0.25 degrees. Significant height of combined wind waves and swell, as well as peak wave period are at a 0.5 degree spatial resolution. All variables were extracted from the domain bounds of 68.5 - 70 N, and 136 - 142 W, and the area-weighted averages over all the latitudes and longitude grid cells within this bounding box were calculated. The hourly timesteps were then averaged over the 24 hours prior to 15:00, in order to correspond with the satellite imagery recording. ERA5 (Hersbach et al., 2018) was downloaded from the Copernicus Climate Change Service (C3S) Climate Data Store.

4.4 RESULTS AND DISCUSSION

4.4.1 Time Series Analysis

Ice Break-up

The time series of high-resolution satellite imagery shows the period of the ice break-up between June 5 and June 21 in great detail. The landfast ice in Thetis Bay retreats from scene to scene (Figure 4-2 a-f). It covers Collinson Head completely on June 5 (Figure 4-2 a), which becomes ice-free by June 6 (Figure 4-2 b). Thetis Bay and the Workboat Passage are still covered by sea-ice, while the west side of HIQ is ice-free. This is a typical situation during the break-up period. Pack-ice generally gets transported northwards on the shelf and does not affect the HIQ nearshore zone. This situation seems to greatly affect turbidity dispersal at the W side of HIQ. During ESE wind conditions, this is the lee side of the island, which causes the high turbidity there due to longshore sediment transport. However, this feature faces SW direction, which is not visible on any other scene from 2019 (arrow in Figure 4-2 b). Williams et al., 2006 suggested that upwelling, which typically occurs N of HIQ during ESE wind direction, gets affected by the occurrence of sea ice and its movement. This has the potential to move the main upwelling area slightly towards the west, and partially 'block' the longshore current towards the NW. This

might only happen during very limited times of the year, when the sea ice on the shelf is melting and transported towards the W due to wind forcing. However, there is no existing *in-situ* dataset to validate this hypothesis. This SW facing longshore drift feature was not identified in recent studies (Klein et al., 2019), where satellite imagery from late June until mid-September was analyzed over three decades, showing that it is either confined to this small time per year, or may even be a 2019 exclusive feature.

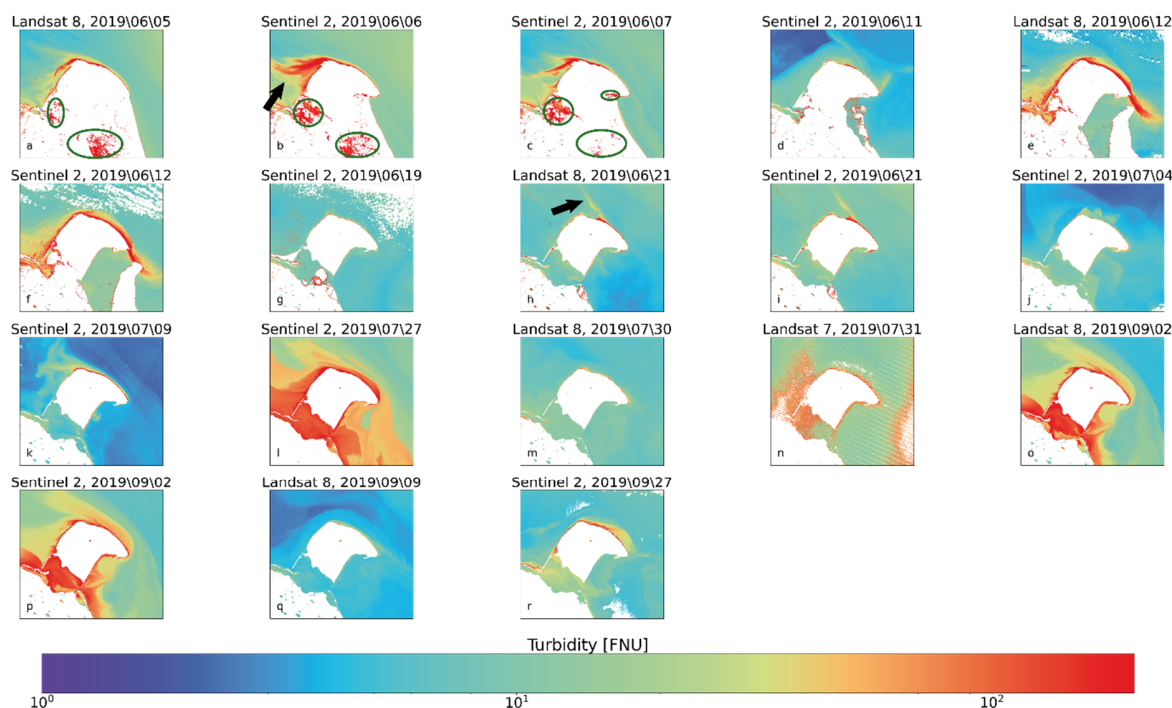


Figure 4-2 Time series of satellite imagery from the summer season 2019. Red areas represent areas of high turbidity, and white areas represent sea ice, clouds, or areas of failed atmospheric correction.

Images with high ice content in Thetis Bay (Figure 4-2 a-c) show areas, where water was identified by the atmospheric correction algorithm within the landfast ice area (green circles). These water areas can be caused by either thawing or flooding. Hill et al., 1991 reported that flooding of landfast ice is widespread during the break-up period, when rivers have their freshets, and that substantial amounts of sediment are likely to be deposited. Another possibility are misclassifications of the atmospheric correction, however, RGB composites (not shown) indicate shallow water areas. Thus, the high modeled turbidity values (above 100 FNU) do not necessarily reflect a high sediment load, but might be contaminated by the reflection of ice beneath the water.

During a period of NW winds in mid-June, the landfast ice gets detached from the Yukon Coast (Figure 4-2 d-f). By June 19, sea ice subsisted only in the Workboat passage and all large chunks of pack ice had vanished from the study area. The formerly ice-covered area in Thetis Bay has relatively high and uniform turbidity (Figure 4-2 e, f), which is caused by increased primary production and the suspended load, which was stored in the ice (Macdonald et al., 2015). The high turbidity feature caused by longshore drift towards the SE on June 12th is considerably larger than identified in chapter 2 and is the largest feature of this kind identified in the whole summer season. Wind speed was very high during the recording of the scene, which has likely caused the high suspended sediment concentration due to stronger wave induced erosion. This is also visible along the NW coast of HIQ, where turbidity is remarkably higher compared to every other NW wind situation captured in 2019. Due to the wind direction, this cannot be caused by the Mackenzie River plume (Klein et al., 2019).

Mid-summer

Sea ice disappears in the nearshore zone of HIQ until June 21. Only small chunks remain in lagoons at the Canadian mainland, which ultimately thaw until July 4. After the sea ice disappeared, turbidity decreased remarkably compared to the storm situation on June 12 (Figure 4-3). Areas of high turbidity are confined to the nearshore waters very close to the coast. A longshore current of higher turbidity is resolved on June 21st along the NE coast towards the NW (Figure 4-2 h, i), which is guided offshore due upwelling N of HIQ and the Coriolis force (arrow in Figure 4-2 h). On July 4, features characteristic of changing wind conditions identified in chapters 2 and 3 are resolved, most prominent a circular feature of increased turbidity NW of HIQ (Figure 4-2 j). This changes July 9, when ESE winds cause longshore drift towards the W (Figure 4-2 k).

July 27 marks a day of exceptionally high turbidity in the whole nearshore zone of HIQ (Figure 4-2, Figure 4-3). High, uniform turbidity values are resolved in the Workboat Passage, the area between HIQ and the Yukon mainland, which is only rarely visible on the 2019 imagery. Longshore drift towards the NW is well resolved along the NE coast of HIQ. High turbidity values are also resolved in Herschel Basin east of the island, which indicates external sediment sources being transported into the nearshore waters of HIQ. This high suspended sediment load

does not correspond to typical drivers, such as wind speed or the Mackenzie discharge. The listed features are not long lasting, as turbidity on July 30 decreased significantly (Figure 4-2 m, n). Turbidity values close to the shoreline are among the lowest during the whole summer season, but remain higher than average a few kilometers off the coast. On the one hand, this shows the quickly changing conditions in the nearshore area, but on the other hand, highlights the need to further investigate external influences on turbidity and suspended sediment concentration in nearshore waters.

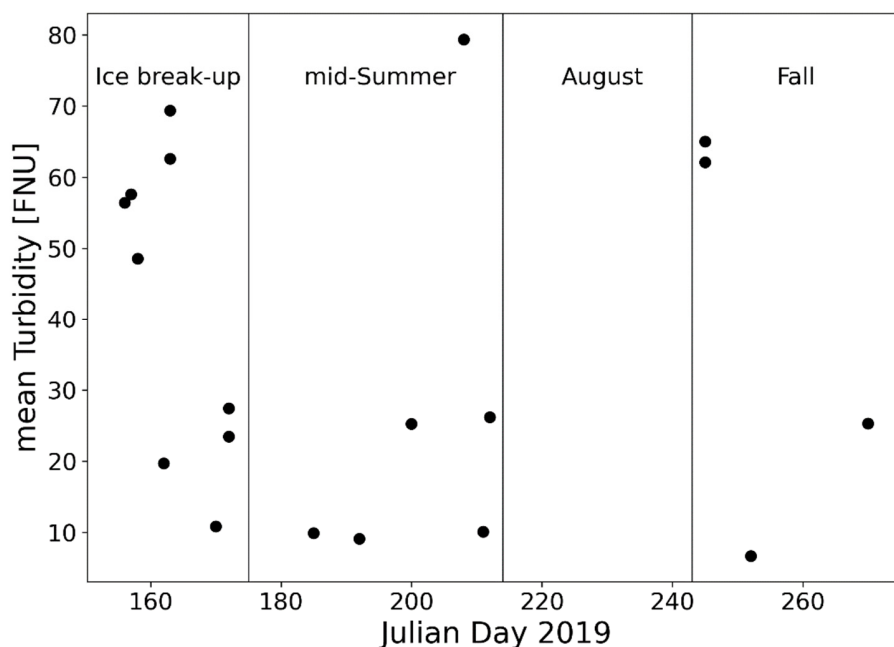


Figure 4-3 Overview of mean turbidity in the area of interest over the summer season 2019.

August, unfortunately, was very cloudy and no cloud-free high-resolution satellite images were recorded by either Landsat 7, Landsat 8 or Sentinel 2. *In-situ* weather data from the HIQ weather station reveals that August was very cold with a mean daily temperature of 5°C compared to the average temperature between 2001 and 2021 (6.8 °C, Environment Canada, Figure 4-4). The Mackenzie discharge did not show any substantial anomalies. The cold temperatures together with normal river discharge indicates that turbidity values in the nearshore waters of HIQ remained low in August. This suggests reduced thermo-erosion, which was identified as a main

mechanism for erosion along permafrost dominated coastlines (Nielsen et al., 2020; Rolph et al., 2021).

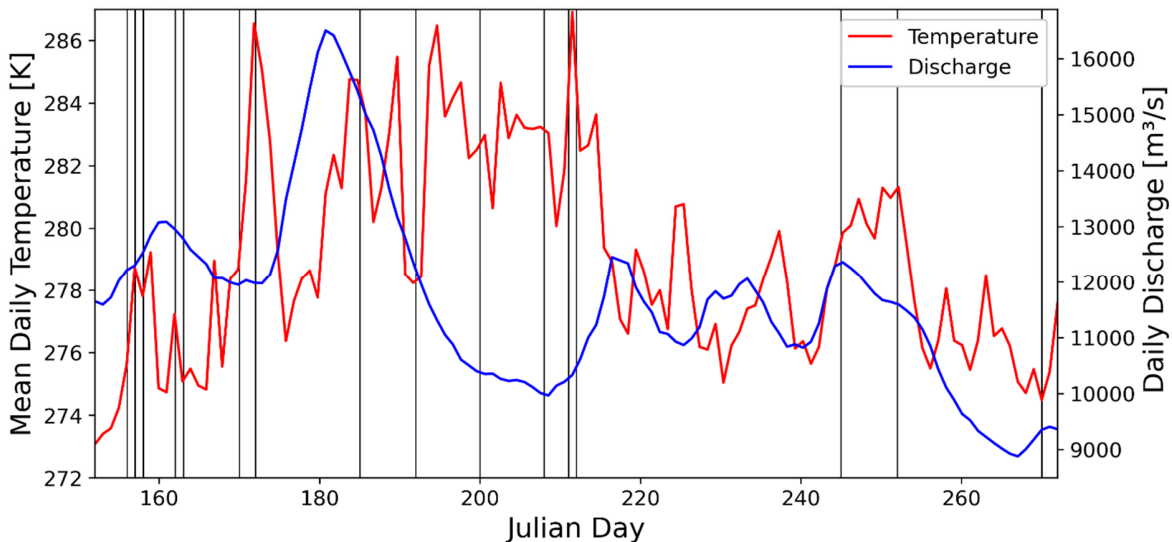


Figure 4-4 Mean daily temperature from the weather station at HIQ between June 1 and September 30 (red) and daily Mackenzie River discharge measured at Arctic Red Tsiigehtchic for the same time period (blue). Black lines indicate the dates of satellite image recordings.

Fall

In September, cloud conditions became more favorable for optical remote sensing. Imagery recorded September 2 reveal high turbidity values over large parts of the nearshore zone (Figure 4-2 o, p). This situation is comparable to that of July 27. Air temperatures on September 2nd were higher compared to the previous days (max. temperature 7°C compared to 4°C, Figure 4-4), enhancing thermo-erosion, and thus sediment supply, to the nearshore zone. Turbidity is especially high in Workboat Passage, where longshore currents cause resuspension in shallow waters. Longshore drift is also well resolved along the NE coast of HIQ towards the west, and turbidity features along the SE coast indicate a larger erosional event, probably related to retrogressive thaw slumps, which are common erosional features there.

Until September 9 (Figure 4-2 q), turbidity decreased to the lowest values throughout the whole summer season (Figure 4-3), both very close and further away from the coastline, even though air temperatures exceed 10 °C on that day, which is exceptionally high for that time of the year (Figure 4-4). Wind directions are changing, but longshore drift towards the SE is resolved.

Similar features are resolved in the last image from the season, recorded on September 27, but with higher turbidity values throughout the whole nearshore zone, even though air temperatures do not exceed 3°C (Figure 4-2 r).

The analysis of the time series reveals multiple erosion events throughout the summer season, which contribute substantial amounts of sediment to the nearshore zone. One erosion event was triggered by a major storm on June 12, with strong longshore sediment transport towards the SE. This was the only major storm detected on satellite imagery, which is in part due to generally high cloud coverage during storms. Longshore drift conditions towards the NW were detected throughout the whole summer season (June, July, and September). This feature was not limited to a specific part of the summer season. The same is true for the low turbidity situations, which were also detected in June, July, and September. Generally, turbidity was increased during the ice break-up, which was not related to high wind speed, but high air temperature (up to 10°C). On the other hand, the imagery from September shows that air temperature is not the predominant driver of nearshore turbidity.

4.4.2 Drivers of turbidity

The combination of *in-situ* measurements from the weather station at HIQ, the daily Mackenzie River discharge data from Arctic Red River, and ERA5 reanalysis data were used to identify drivers of nearshore sediment dispersal and to evaluate the results presented in Klein et al. 2019. The highest correlation was identified between turbidity and mean wind speed from the reanalysis data set ($R^2 = 0.49$, Figure 4-5 a), turbidity and significant wave height ($R^2 = 0.46$, Figure 4-5 b), and turbidity and wave period ($R^2 = 0.27$, Figure 4-5 c). Interestingly, in contrast to the reanalysis wind speed, the *in-situ* wind speed from the HIQ weather station does not show any correlation to turbidity (Figure 4-5 i). This might be due to the location of the weather station on the island: located at Simpson Point, it is slightly shielded from wind from westerly directions. During westerly and northwesterly wind conditions, highest turbidity values were detected around HIQ (Figure 4-6), which largely contrasts the findings made by Klein et al. 2019.

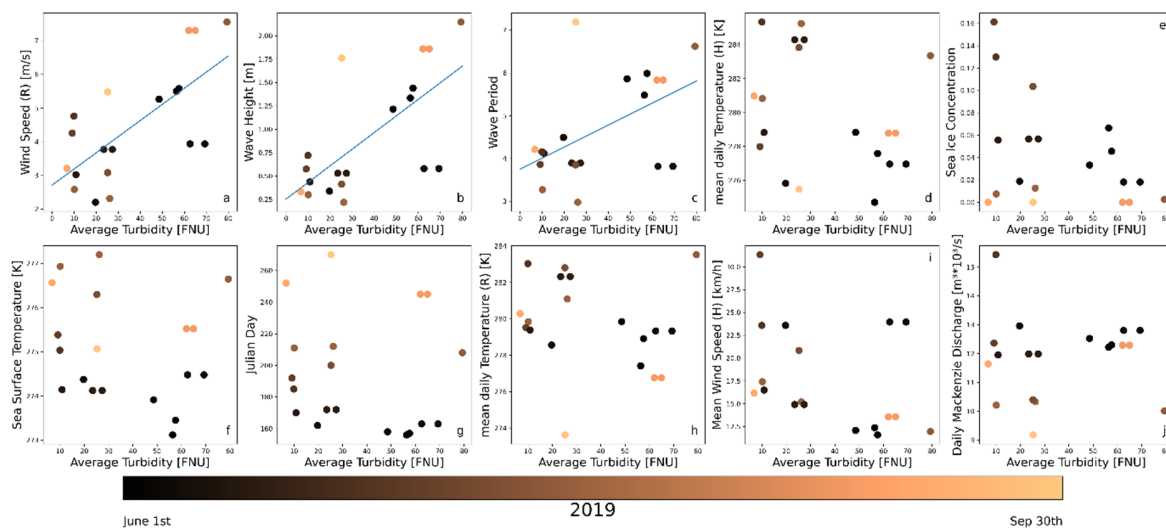


Figure 4-5 Correlation of possible drivers and nearshore turbidity. For parameters which were both measured by the HIQ weather station and downloaded in the ERA5 reanalysis dataset, (H) relates to the HIQ measurement and (R) to the ERA5 reanalysis dataset.

In contrast to the results presented in chapter 2, no correlation was identified between the Mackenzie River discharge and turbidity at HIQ (Figure 4-5 j). It is noted, though, that the discharge data used is preliminary, and thus did not pass through the complete quality checks at Environment Canada. It is also shown that the daily discharge did not necessarily follow expected seasonal patterns in 2019 (Figure 4-4), as daily discharge values between 12,000 m³/s and 13,000 m³/s were detected both early and late during the summer season (Yang et al., 2015). For example, the Mackenzie discharge around June 9 (Julian day 160) 2019 hit a maximum during the ice break-up period with ~13000 m³/s, which is more than 50 % lower than the 1973-2011 average of ~21000 m³/s (Yang et al., 2015).

The data from 2019 indicates that nearshore turbidity is related to wave energy (Figure 4-5 b, c). This is due to erosion-inducing wave action on permafrost coastlines, supplying sediment to the nearshore waters, and resuspension of formerly deposited sediment. The rate of which resuspension affects surface turbidity has not been quantified yet. Resuspension, however, depends on wave period. Higher wave period causes a higher depth, up to which a wave interacts with the seafloor (Dean and Dalrymple, 1991) and thus increases the area affected by resuspension.

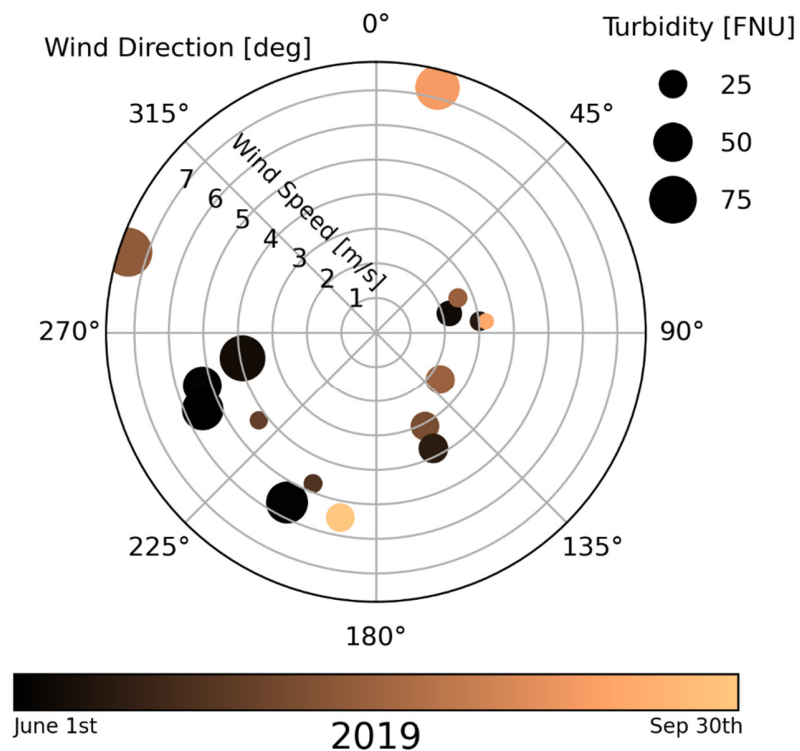


Figure 4-6 Rose diagram showing the dependence of nearshore turbidity on wind speed (reanalysis data from the shelf) and wind direction (in-situ data from HIQ).

The data further clarifies that nearshore turbidity is not driven by air temperature, sea surface temperature, or sea ice concentration on the shelf. A general comparison indicates that *in-situ* data from HIQ does not correlate to nearshore turbidity in most cases, but the reanalysis data from the shelf does. This shows that nearshore turbidity, albeit being of very limited spatial extent, is strongly affected by the weather conditions several hundreds of kilometers offshore, while weather conditions in close vicinity have very limited impact on it.

4.5 CONCLUSION

The aim of this study was to identify seasonal patterns of nearshore turbidity and its drivers in the nearshore zone of Herschel Island Qikiqtaruk in the western Canadian Arctic. A time series of high-resolution satellite imagery from the summer season 2019, as well as *in-situ* measurements and ERA5 reanalysis data of atmospheric and oceanic climate variables, and Mackenzie River discharge data, were used. It is shown that nearshore turbidity is driven by

wind speed and wind direction, as well as wave height and wave period. Seasonal variations could not be identified; however, it is shown that turbidity was higher during the period of ice break-up compared to the rest of the open water season.

Nearshore turbidity did not show spatial patterns that were expected based on the results presented in chapter 2. This is due to the weak correlation of nearshore turbidity and the Mackenzie discharge. It is noted, however, that the Mackenzie discharge did not necessarily follow its usual seasonal cycle during Summer 2019. Nearshore turbidity shows higher correlation to ERA5 wind speed rather than *in-situ* wind speed from Herschel Island Qikiqtaruk, showing that nearshore turbidity, despite being of regional spatial extent, gets driven by weather conditions several kilometers away from the nearshore zone. Remote sensing has shown to be a powerful tool to detect nearshore turbidity, especially in areas that are difficult to access such as the Arctic.

To further facilitate the drivers of nearshore turbidity in the Arctic, longer time series are needed to eliminate yearly anomalies. However, time series of high-resolution satellite images, like the one presented in this study, are rare due to low temporal resolution of appropriate satellite sensors and challenging weather conditions. This might improve with the recent launch of OLI2 onboard Landsat 9, essentially doubling the potential amount of available Landsat imagery. Including multiple study sites will validate the results on a pan-Arctic scale, and will help to foster our understanding of suspended sediment dynamics in Arctic nearshore zones.

Funding

This publication is part of the Nunataryuk project. The project has received funding under the European Union's Horizon 2020 Research and Innovation Program under grant agreement no. 773421. K.P.K. was financially supported by a Ph.D. stipend by the University of Potsdam (PoGS Potsdam Graduate School). R.J.R. was financially supported by the GeoX research network for Geosciences in Berlin and Potsdam under grant number SO_087.

Acknowledgements

USGS and NASA are acknowledged for Landsat imagery. ESA is acknowledged for Sentinel 2 and 3 imagery. We thank Justus Gimsa for his help during the statistical analysis.

5 SYNTHESIS

Turbidity in Arctic coastal waters and its detection in time and space using remote sensing are the main foci of this thesis. This rather narrow focus is justified by the important role that turbidity plays for the coastal ecosystem and the lack of studies addressing it in the coastal Arctic. Turbidity caused by suspended sediments is indeed a widespread phenomenon in the Arctic nearshore zone. It can be caused by coastal erosion, river discharge, or resuspension. It has multiple impacts on the biophysical system, including decreased primary production due to reduced light transmission through the water column (Mangan et al., 2020), and the potential transformation of organic rich sediment into greenhouse gases at the water surface (Tanski et al., 2019; Vonk et al., 2012). Due to climate change, coastal erosion is expected to increase, as thermo-erosion is the main erosional process along permafrost affected coastlines (Nielsen et al., 2020; Rolph et al., 2021). River discharge is expected to rise due to the intensification of the water cycle (Van Vliet et al., 2013). Ultimately, turbidity is likely to increase, resulting in greater impacts in the coastal zone.

The overall aim of this dissertation was to expand the knowledge on suspended sediment dynamics in the Arctic nearshore zone using remotely sensed imagery. Therefore, a semi-empirical algorithm, which relates water-leaving reflectance to surface water turbidity, was recalibrated using field data from the optically complex nearshore waters in the Arctic. Its application to high-resolution satellite imagery from the summer season 2019, together with ocean and climate variables, was used to identify drivers of nearshore turbidity and its seasonal variations. This chapter will discuss how the results stemming from the thesis advance the current knowledge on the Arctic nearshore zone and which challenges may be encountered in future studies.

5.1 APPLICABILITY OF REMOTE SENSING ALGORITHMS IN THE ARCTIC NEARSHORE ZONE

Remote sensing has successfully been used to support oceanographic studies over the past decades. However, its usage in the nearshore zone is limited due to the lack of validation datasets (most oceanographic studies do not cover the nearshore, because of hazardous conditions for science vessels) and high optical complexity, which is caused by the interaction of colored dissolved organic matter (cDOM), phytoplankton pigments, and suspended sediment. Results presented in chapter 2 show that turbidity algorithms available in the literature and used in a wide range of settings world-wide do not capture the complexity of the Arctic nearshore zone. This might be caused by the high organic matter content of coastal permafrost, which colors the sediment dark brown, due to the dominance of light absorption of non-algal particles. This affects the way sediment reflects radiation (Bhargava and Mariam, 1990) and causes the offset in the linear relationship between turbidity and SPM concentration observed in chapter 3 (Figure 3-4).

The results presented in chapter 3 show that the inclusion of permafrost-affected water in the algorithm used to retrieve turbidity information clearly improves the performance compared to the general turbidity algorithm published by Dogliotti et al., 2015. The ANTA is capable to better resolve smaller turbidity values (below 10 FNU) and to better match *in-situ* measurements, even though it still overestimates observed values. While the algorithm by Dogliotti et al. 2015 overestimates higher turbidity values (above 100 FNU), the ANTA accurately resolves those values and provides higher accuracy in very turbid waters.

The application of the ANTA to satellite imagery that matches *in-situ* turbidity samples in Adventfjorden, Svalbard, demonstrates the transferability of the ANTA to nearshore zones beyond HIQ. The sediment composition in Adventfjorden differs substantially to the Beaufort Sea due to the heavily glaciated catchments (Węśławski et al., 2011). The glaciers provide a larger amount of inorganic matter to the nearshore waters (Zajaczkowski and Włodarska-Kowalczyk, 2007), which has different optical properties (Gould et al., 2002), together with higher freshwater input (Aurin and Dierssen, 2012). The good performance of the ANTA might

in part be in part due to the timing of the sampling outside the main melting season in July, when the suspended sediment has higher contribution of inorganic matter (Walch, 2021; Poste, unpublished data). Yet, it showed that an algorithm dedicated to nearshore waters performs better than algorithms conceived for offshore or estuarine areas.

The satellite imagery presented in chapter 2 and processed using our ANTA algorithm showed a high sediment load in the very vicinity of the coastline of HIQ. This sediment load, potentially holding large amounts of organic matter, was not resolved yet by medium resolution satellite imagery such as MODIS or Sentinel 3 OLCI (Vanhellemont and Ruddick, 2014). The results from chapter 3 support this, as it is shown that Sentinel 3 OLCI imagery is not capable to resolve high sediment loads close to the coastline, which is resolved by both Sentinel 2 and Landsat 8. Strong turbidity gradients from nearshore to offshore indicate that most of the suspended sediment is transported alongshore rather than offshore. This is supported by recent field observations (Jong et al., 2020), which show that sediment is primarily deposited at shallow water depth (below 5 m), where it is subject to constant resuspension due to wave energy, and that sediment export offshore at the seafloor is limited. Clearly, the use of medium resolution imagery to resolve nearshore turbidity is not sufficient and the presented approach demonstrates the potential of new algorithms based on higher resolution imagery results.

5.2 DRIVERS OF NEARSHORE TURBIDITY

The drivers of nearshore turbidity in the Arctic differ from the ones identified outside the Arctic. This is due to the lower tidal range in the Arctic (Kulikov et al., 2018), which is a major driver of nearshore turbidity in the temperate and tropical oceans (Cartwright et al., 2021). Coastal erosion plays a significant role in nearshore turbidity in the Arctic, as identified in chapters 2 and 4. Waves are a major driver of permafrost coastal erosion, and the results from chapter 4 show a linear relationship between significant wave-height on the Canadian Beaufort Shelf and nearshore turbidity. Comparing the ERA5 reanalysis data with historical reports of significant wave-height (Hill and Nadeau, 1989) showed that significant wave height has increased over the past 30 years, which concurs with observations of intensified coastal erosion in the area (Obu et al., 2016).

The Mackenzie River discharge was assumed to be the main influencing factor of nearshore turbidity around HIQ, as its plume has the ability to cover large parts of the Canadian Beaufort Shelf under ESE wind conditions (Doxaran et al., 2012; Hill et al., 1991). However, at least for the 2019 summer season, nearshore turbidity does not show any correlation to the Mackenzie River discharge, as shown in chapter 4. In chapter 2, however, it is shown that nearshore turbidity depends on the predominant wind direction, which greatly affects the Mackenzie River plume. It is possible that this is a result of decreased summer discharge but increased spring discharge of the major Arctic rivers (Ahmed et al., 2020), including the Mackenzie River, since 1980. The oldest used imagery, recorded prior to 2000, would have captured higher Mackenzie discharges in summer, which would have led to higher suspended sediment loads. Most of the satellite imagery used in chapter 2 was recorded in July and August and is thus affected by the decline of summer discharge, while half of the imagery used in chapter 4 was recorded in June, while the nearshore zone of HIQ was still affected by the occurrence of sea ice. Another factor is that the Mackenzie River discharge from 2019 shows an uncommon behavior, with lower discharge over the whole ice-free season compared to the mean discharge (Yang et al., 2015).

The results from chapter 4 show that nearshore turbidity is well correlated to wind speed on the Canadian Beaufort Shelf, but not correlated to *in-situ* wind speed from the weather station at HIQ. This supports the hypothesis that nearshore turbidity is primarily driven by erosion and resuspension due to wave energy, as high wind speed on the Beaufort Shelf causes shear stress on the water surface and thus increases wave energy. Nearshore turbidity also depends on upwelling, as discussed in chapters 2 and 4, which causes resuspension N of HIQ. Upwelling depends on wind forcing on the shelf (Williams et al., 2006), but also ice movement. During ESE winds, cold but nutrient rich water from the Canada Basin gets transported onto the Beaufort Shelf through Mackenzie Through, where it travels westwards, until it surfaces N of HIQ. This all combined shows that nearshore turbidity around HIQ heavily depends on the weather conditions at the Beaufort Shelf, as they influence hydrodynamics such as waves and upwelling, while the weather conditions in the direct vicinity of the nearshore zone have little to no influence on it.

5.3 SPATIAL VARIATIONS OF NEARSHORE TURBIDITY

Chapters 2 and 4 investigated the spatial variability of surface turbidity around HIQ during the open-water season. As previously discussed, turbidity has multiple drivers, which are characterized by seasonal variations. Chapter 2 identified substantially larger turbidity extent during steady ESE wind conditions, which was assumed to be related to the Mackenzie River plume extent. This spatial feature was also detected in chapter 4. However, in chapter 4, the Mackenzie River discharge was not detected as driver of high turbidity in the nearshore zone of HIQ. In chapter 2, very high turbidity values were detected during steady ESE wind conditions directly at the coastline using the Dogliotti et al. 2015 algorithm. These turbidity values were much higher than each turbidity sample taken over the field seasons 2018 and 2019. The ANTA, a recalibration of this general turbidity algorithm, results in a more accurate estimation.

During steady ESE wind conditions, high turbidity areas extend to water depths where surface waves do not cause resuspension. Suspended sediment observed on satellite imagery is thus more likely to be freshly eroded from the coast. This also means that the area where organic matter from carbon rich sediments could be directly transferred to greenhouse gases is potentially larger. Suspended sediment outside the resuspension zone has the same ratio of organic matter as the suspended sediment directly at the coastline (Jong et al., 2020), which shows that these extended zones of turbidity could result in greater greenhouse gas release and thus in a greater impact on the global climate. The larger high turbidity extent also affects primary production (Mangan et al., 2020) and thus the whole food chain, however, the interactions of those processes are not well understood yet.

It is challenging to identify the reason for the high turbidity during steady ESE wind conditions. The results from chapter 4 show that wind speed and wave energy are not the primary drivers, and, in contrast to chapter 2, that it is not directly linked to the Mackenzie River discharge. It is possible that the discharge of smaller rivers along the Yukon Coast, such as the Babbage River, provide a large amount of suspended sediments. However, the Babbage River discharge is mostly driven by extreme rainfall events in its catchment (Forbes, 1979), and therefore its suspended sediment load is limited. One possible driver is upwelling, however, this is confined to a small area N of HIQ and does not affect the whole nearshore zone (Williams et al., 2006).

The state-of-the-art knowledge of the interaction between coastal erosion, upwelling, resuspension, and river discharge is not sufficient to identify the reason of high nearshore turbidity during steady ESE wind conditions. In other words, the scarcity of data from the field limits the potential to clearly identify and discriminate the processes and mechanisms driving turbidity in the nearshore zone.

5.4 CHALLENGES AND OUTLOOK

One major challenge encountered over the time frame of this PhD project was the general availability of validation data in the Arctic nearshore zone. Sampling campaigns have to overcome major logistical challenges due to the remoteness of most parts of the Arctic. Nearshore sampling requires coastal ships with small draft and are therefore vulnerable towards waves and currents. Even though turbidity sampling does not require laboratory work and can be performed on site, biogeochemical samples often require fast analysis to secure high quality results, which is often not available in the field. This, however, will not change in the near future, even though the scientific benefits of greater analytical capacity would be very substantial.

Remote Sensing has the potential to overcome many of these challenges. Imagery can be provided on a daily basis with moderate spatial resolution (e.g. MODIS, Sentinel 3), and higher spatial resolution imagery on a weekly to bi-weekly basis (e.g. Landsat 8, Sentinel 2). The temporal resolution is likely to increase in the near future with newer satellites such as Landsat 9 and other polar orbiting satellites being launched. *In-situ* samples will still be needed for validation of satellite imagery, though (Loisel et al., 2013). Optical remote sensing also heavily depends on weather conditions, since clouds cover all information beneath them.

Atmospheric correction algorithms have greatly improved over the past decade, but they are still the largest source of uncertainty for ocean color applications. The ACOLITE dark spectrum fitting has proven to be the most robust atmospheric correction over coastal waters (Renosh et al., 2020), but its error range versus *in-situ* measurements still ranges from 30-70 % (Vanhellemont, 2019). This is likely to improve in the future due to more sophisticated atmospheric correction algorithms and higher spectral accuracy of future satellite sensors.

A logical next step to enhance the results obtained during this PhD-thesis will be the estimation of greenhouse gas emissions from suspended sediment in permafrost affected nearshore zones. This could be done with a stationary pCO₂ sensor, or by laboratory experiments, which simulate the conditions in the Arctic nearshore zone. This will foster the understanding of the role of the Arctic nearshore zone in the global climate context and help to create a carbon budget for the Arctic coastal zone that could inform our efforts to understand the role of turbidity. The specific measurement of particulate organic matter (POC) within the suspended sediment will further support these estimations.

Another important step will be the collection of ancillary data around the Arctic. Validation data is particularly sparse there, which is due to the logistical challenges for field campaigns. Buoys could be used over the ice-free season, which would result in a large quantity of data. Buoys, however, are endangered by ice and storms, which makes the deployment difficult without supervision and limits the possibility to react quickly to potential hazards to the instruments. With the additional data available, the ANTA can be validated on a pan-Arctic scale, which would drastically expand the usability of the results put forward in this thesis and to open a new era for the resolution of nearshore processes.

LIST OF ACRONYMS

ANTA	Arctic Nearshore Turbidity Algorithm
AOI	Area of interest
BT	Brightness temperature
C3S	Copernicus Climate Change Service
cDOM	Colored dissolved organic matter
cf-mask	C-function of mask
DEM	Digital elevation model
DN	Digital number
DOC	Dissolved organic matter
E	Irradiance
E _D	Downwelling irradiance
ESA	European Space Agency
ETM+	Enhanced Thematic Mapper +
FNU	Formazin turbidity unit
HIQ	Herschel Island Qikiqtaruk
L	Radiance
L1T	Level 1T
L2	Level 2
L _A	Radiance add
L _D	Sky radiance
L _M	Radiance multiliert
L _U	Upwelling radiance
MERIS	Medium Resolution Imaging Spectromete
MODIS	Moderate-resolution Imaging Spectroradiometer
MSI	Multi-Spectral Imager
NAP	Non-algal particles
NIR	Near-infrared
OC	Organic matter
OLCI	Ocean and Land Color Imager
OLI	Operational Land Imager
POC	Pariculate organic matter
RGB	red, green and blue
R _{RS}	Remote sensing reflectance
R _w	Water leaving reflectance
SeaWiFs	Sea-viewing Wide Field-of-view Sensor
SLC	Scan line corrector
SPM	Suspended Particulate Matter
STD	Standard deviation

SWIR.....	<i>Short-wave infrared</i>
T	<i>Turbidity</i>
Tg	<i>Terragrams</i>
TIRS	<i>Thermal Infrared Sensor</i>
TM.....	<i>Thematic Mapper</i>
USGS	<i>United States Geological Survey</i>
wt%	<i>weight percentage</i>

BIBLIOGRAPHY

- Ahmed, R., Prowse, T., Dibike, Y., Bonsal, B., O'Neil, H., 2020. Recent trends in freshwater influx to the arctic ocean from four major arctic-draining rivers. *Water* 12. <https://doi.org/10.3390/W12041189>
- Arrhenius, S., 1896. On the Influence of Carbonic Acid in the Air upon the Temperature of the Ground. London, Edinburgh, Dublin *Philos. Mag. J. Sci.* 41, 237–276. <https://doi.org/10.1080/14786449608620846>
- Arrigo, K.R., van Dijken, G., Pabi, S., 2008. Impact of a shrinking Arctic ice cover on marine primary production. *Geophys. Res. Lett.* 35, 1–6. <https://doi.org/10.1029/2008GL035028>
- Atkinson, D.E., 2005. Observed storminess patterns and trends in the circum-Arctic coastal regime. *Geo-Marine Lett.* 25, 98–109. <https://doi.org/https://doi.org/10.1007/s00367-004-0191-0>
- Aurin, D.A., Dierssen, H.M., 2012. Advantages and limitations of ocean color remote sensing in CDOM-dominated, mineral-rich coastal and estuarine waters. *Remote Sens. Environ.* 125, 181–197. <https://doi.org/10.1016/j.rse.2012.07.001>
- Bailard, J.A., 1982. Modeling On-Offshore Sediment Transport in the Surfzone. *Coast. Eng.* 1419–1438. <https://doi.org/10.1061/9780872623736.087>
- Barsi, J.A., Schott, J.R., Hook, S.J., Raqueno, N.G., Markham, B.L., Radocinski, R.G., 2014. Landsat-8 Thermal Infrared Sensor (TIRS) Vicarious Radiometric Calibration. *Remote Sens.* 6, 11607–11626. <https://doi.org/10.3390/rs6111607>
- Baughman, C.A., Jones, B.M., Bartz, K.K., Young, D.B., Zimmerman, C.E., 2015. Reconstructing Turbidity in a Glacially Influenced Lake Using the Landsat TM and ETM+ Surface Reflectance Climate Data Record Archive, Lake Clark, Alaska. *Remote Sens.* 7, 13692–13710. <https://doi.org/10.3390/rs71013692>
- Bhargava, D.S., Mariam, D.W., 1990. Spectral reflectance relationships to turbidity generated by different clay materials. *Photogramm. Eng. Remote Sensing* 56, 225–229.
- Biskaborn, B.K., Smith, S.L., Noetzli, J., Matthes, H., Vieira, G., Streletskiy, D.A., Schoeneich, P., Romanovsky, V.E., Lewkowicz, A.G., Abramov, A., Allard, M., Boike, J., Cable, W.L., Christiansen, H.H., Delaloye, R., Diekmann, B., Drozdov, D., Etzelmüller, B., Grosse, G., Guglielmin, M., Ingeman-Nielsen, T., Isaksen, K., Ishikawa, M., Johansson, M., Johannsson, H., Joo, A., Kaverin, D., Kholodov, A., Konstantinov, P., Kröger, T., Lambiel, C., Lanckman, J.P., Luo, D., Malkova, G., Meiklejohn, I., Moskalenko, N., Oliva, M., Phillips, M., Ramos, M., Sannel, A.B.K., Sergeev, D., Seybold, C., Skryabin, P., Vasiliev, A., Wu, Q., Yoshikawa, K., Zheleznyak, M., Lantuit, H., 2019. Permafrost is warming at a global scale. *Nat. Commun.* 10, 1–11. <https://doi.org/10.1038/s41467-018-08240-4>
- Bloesch, J., 1982. Inshore-Offshore Sedimentation Differences Resulting from Resuspension in

the Eastern Basin of Lake Erie". *Can. J. Fish. Aquat. Sci* 39, 748–759.

- Box, J.E., Colgan, W.T., Christensen, T.R., Schmidt, N.M., Lund, M., Parmentier, F.J.W., Brown, R., Bhatt, U.S., Euskirchen, E.S., Romanovsky, V.E., Walsh, J.E., Overland, J.E., Wang, M., Corell, R.W., Meier, W.N., Wouters, B., Mernild, S., Mård, J., Pawlak, J., Olsen, M.S., 2019. Key indicators of Arctic climate change: 1971-2017. *Environ. Res. Lett.* 14. <https://doi.org/10.1088/1748-9326/aafc1b>
- Burn, C.R., Hattendorf, J.B., 2011. Toponymy of Herschel Island (Qikiqtaryuk), Western Arctic Coast , Canada. *Arctic* 64, 459–464.
- Burn, C.R., Zhang, Y., 2009. Permafrost and climate change at Herschel Island (Qikiqtaruq), Yukon Territory , Canada. *J. Geophys. Res.* 114, 1–16. <https://doi.org/10.1029/2008JF001087>
- Carmack, E., Wassmann, P., 2006. Food webs and physical-biological coupling on pan-Arctic shelves: Unifying concepts and comprehensive perspectives. *Prog. Oceanogr.* 71, 446–477. <https://doi.org/10.1016/j.pocean.2006.10.004>
- Cartwright, P.J., Fearn, P.R.C.S., Branson, P., Cutler, M.V.W., O’leary, M., Browne, N.K., Lowe, R.J., 2021. Identifying metocean drivers of turbidity using 18 years of modis satellite data: Implications for marine ecosystems under climate change. *Remote Sens.* 13. <https://doi.org/10.3390/rs13183616>
- Coch, C., Lamoureaux, S.F., Knoblauch, C., Eischeid, I., Fritz, M., Obu, J., Lantuit, H., 2018. Summer rainfall dissolved organic carbon, solute, and sediment fluxes in a small Arctic coastal catchment on Herschel Island (Yukon Territory, Canada). *Arct. Sci.* 4, 750–780. <https://doi.org/10.1139/as-2018-0010>
- Constantin, S., Constantinescu, Ş., Doxaran, D., 2017. Long-term analysis of turbidity patterns in Danube Delta coastal area based on MODIS satellite data. *J. Mar. Syst.* 170, 10–21. <https://doi.org/10.1016/j.jmarsys.2017.01.016>
- Couture, N.J., Irrgang, A., Pollard, W., Lantuit, H., Fritz, M., 2018. Coastal Erosion of Permafrost Soils Along the Yukon Coastal Plain and Fluxes of Organic Carbon to the Canadian Beaufort Sea. *J. Geophys. Res. Biogeosciences* 123, 406–422. <https://doi.org/10.1002/2017JG004166>
- Cunliffe, A., Tanski, G., Radosavljevic, B., Palmer, W., Sachs, T., Lantuit, H., Kerby, J., Myers-Smith, I., 2019. Rapid retreat of permafrost coastline observed with aerial drone photogrammetry. *Cryosphere* 13, 1513–1528. <https://doi.org/10.5194/tc-13-1513-2019>
- Dean, R.G., Dalrymple, R.A., 1991. *Water Wave Mechanics for Engineers and Scientists*. Advanced Series on Ocean Engineering, Volume 2. ed. World Scientific Publishing, Singapore. <https://doi.org/doi:10.1142/1232>
- Déry, S.J., Hernández-Henríquez, M.A., Burford, J.E., Wood, E.F., 2009. Observational evidence of an intensifying hydrological cycle in northern Canada. *Geophys. Res. Lett.* 36, 1–5. <https://doi.org/10.1029/2009GL038852>

- Doerffer, R., Fischer, J., Stössel, M., Brockmann, C., Grassl, H., 1989. Analysis of thematic mapper data for studying the suspended matter distribution in the coastal area of the German Bight (North Sea). *Remote Sens. Environ.* 28, 61–73. [https://doi.org/10.1016/0034-4257\(89\)90105-3](https://doi.org/10.1016/0034-4257(89)90105-3)
- Dogliotti, A.I., Ruddick, K.G., Nechad, B., Doxaran, D., Knaeps, E., 2015. A single algorithm to retrieve turbidity from remotely-sensed data in all coastal and estuarine waters. *Remote Sens. Environ.* 156, 157–168. <https://doi.org/10.1016/j.rse.2014.09.020>
- Doxaran, D., Devred, E., Babin, M., 2015. A 50 % increase in the mass of terrestrial particles delivered by the Mackenzie River into the Beaufort Sea (Canadian Arctic Ocean) over the last 10 years. *Biogeosciences* 12, 3551–3565. <https://doi.org/10.5194/bg-12-3551-2015>
- Doxaran, D., Ehn, J., Bélanger, S., Matsuoka, A., Hooker, S., Babin, M., 2012. Optical characterisation of suspended particles in the Mackenzie River plume (Canadian Arctic Ocean) and implications for ocean colour remote sensing. *Biogeosciences* 9, 3213–3229. <https://doi.org/10.5194/bg-9-3213-2012>
- Doxaran, D., Froidefond, J.M., Castaing, P., Babin, M., 2009. Dynamics of the turbidity maximum zone in a macrotidal estuary (the Gironde, France): Observations from field and MODIS satellite data. *Estuar. Coast. Shelf Sci.* 81, 321–332. <https://doi.org/10.1016/j.ecss.2008.11.013>
- Dunton, K.H., Weingartner, T., Carmack, E.C., 2006. The nearshore western Beaufort Sea ecosystem: Circulation and importance of terrestrial carbon in arctic coastal food webs. *Prog. Oceanogr.* 71, 362–378. <https://doi.org/10.1016/j.pocean.2006.09.011>
- Fischer, A.M., Pang, D., Kidd, I.M., Moreno-Madriñán, M.J., 2017. Spatio-Temporal Variability in a Turbid and Dynamic Tidal Estuarine Environment (Tasmania, Australia): An Assessment of MODIS Band 1 Reflectance. *Int. J. Geo-Information* 2, 1–15. <https://doi.org/doi:10.3390/ijgi6110320>
- Foga, S., Scaramuzza, P.L., Guo, S., Zhu, Z., Dilley, R.D., Beckmann, T., Schmidt, G.L., Dwyer, J.L., Hughes, M.J., Laue, B., 2017. Cloud detection algorithm comparison and validation for operational Landsat data products. *Remote Sens. Environ.* 194, 379–390. <https://doi.org/10.1016/j.rse.2017.03.026>
- Forbes, D.L., 1997. Coastal erosion and nearshore variability in the southern Beaufort Sea, Ivvavik National Park, Yukon Territory. Dartmouth, Canada. <https://doi.org/doi.org/10.4095/209275>
- Forbes, D.L., 1979. Bottomfast Ice in Northern Rivers: Hydraulic Effects and Hydrometric Implications, in: *Canadian Hydrology Symposium: 79 Proceedings*. pp. 175–184.
- Fritz, M., Vonk, J.E., Lantuit, H., 2017. Collapsing Arctic coastlines. *Nat. Clim. Chang.* 7, 6–7. <https://doi.org/10.1038/nclimate3188>
- Fritz, M., Wetterich, S., Schirrmeister, L., Meyer, H., Lantuit, H., Preusser, F., Pollard, W.H., 2012. Eastern Beringia and beyond: Late Wisconsinan and Holocene landscape dynamics along the Yukon Coastal Plain, Canada. *Palaeogeogr. Palaeoclimatol. Palaeoecol.* 319–

320, 28–45. <https://doi.org/10.1016/j.palaeo.2011.12.015>

- Giovando, L.F., Herlinveaux, R.H., 1981. A Discussion of Factors Influencing Dispersion of Pollutants in the Beaufort Sea. *Pacific Mar. Sci. Rep.* 81.
- Gippel, C.J., 1995. Potential of turbidity monitoring for measuring the transport of suspended solids in streams. *Hydrol. Process.* 9, 83–97.
- Gordeev, V. V., Kravchishina, M.D., 2009. River flux of dissolved organic carbon (DOC) and particulate organic carbon (POC) to the Arctic Ocean: what are the consequences of the global changes?, in: Nihoul, J.C.J., Kostianoy, A.G. (Eds.), *Influence of Climate Change on the Changing Arctic and Sub-Arctic Conditions*. Springer, Dordrecht, Dordrecht, The Netherlands, pp. 145–160. <https://doi.org/https://doi.org/10.1007/978-1-4020-9460-6>
- Gould, R.W., Stavn, R.H., Twardowski, M.S., Lamela, G., 2002. Partitioning optical properties into organic and inorganic components from ocean color imagery, in: Ackleson, S., Trees, C. (Eds.), *Proceedings of the Ocean Optics XVI*. Office of Naval Research CDROM, pp. 1–10.
- Groom, S.B., Sathyendranath, S., Ban, Y., Bernard, S., Brewin, B., Brotas, V., Brockmann, C., Chauhan, P., Choi, J.K., Chuprin, A., Ciavatta, S., Cipollini, P., Donlon, C., Franz, B.A., He, X., Hirata, T., Jackson, T., Kampel, M., Krasemann, H., Lavender, S.J., Pardo-Martinez, S., Melin, F., Platt, T., Santoleri, R., Skakala, J., Schaeffer, B., Smith, M., Steinmetz, F., Valente, A., Wang, M., 2019. Satellite ocean colour: Current status and future perspective. *Front. Mar. Sci.* 6. <https://doi.org/10.3389/fmars.2019.00485>
- Hanssen-Bauer, I., Førland, E.J., Hisdal, H., Mayer, S., Sandø, A.B., Sorteberg, A. (Eds.), 2019. *Climate in Svalbard 2100 – a knowledge base for climate adaptation*. Norwegian Centre of Climate Services (NCCS) for Norwegian Environment Agency (Miljødirektoratet).
- Héquette, A., Hill, P.R., 1993. Storm-generated currents and offshore sediment transport on a sandy shoreface, Tibjak Beach, Canadian Beaufort Sea. *Mar. Geol.* 113, 283–304.
- Hersbach, H., Bell, B., Berrisford, P., Biavati, G., Horanyi, A., Muñoz Sabater, J., Nicolas, J., Peubey, C., Radu, R., Rozum, I., Schepers, D., Simmons, A., Soci, C., Dee, D., Thépaut, J.-N., 2018. ERA5 hourly data on single levels from 1979 to present. <https://doi.org/10.24381/cds.adbb2d47>
- Hilker, T., Wulder, M.A., Coops, N.C., Linke, J., McDermid, G., Masek, J.G., Gao, F., White, J.C., 2009. A new data fusion model for high spatial- and temporal-resolution mapping of forest disturbance based on Landsat and MODIS. *Remote Sens. Environ.* 113, 1613–1627. <https://doi.org/10.1016/j.rse.2009.03.007>
- Hill, P.R., Blasco, S.M., Harper, J.R., Fissel, D.B., 1991. Sedimentation on the Canadian Beaufort Shelf. *Cont. Shelf Res.* 11, 821–842. [https://doi.org/10.1016/0278-4343\(91\)90081-G](https://doi.org/10.1016/0278-4343(91)90081-G)
- Hill, P.R., Nadeau, O.C., 1989. Storm-dominated sedimentation on the inner shelf of the Canadian Beaufort Sea. *J. Sediment. Res.* 59.

- Holmes, R.M., McClelland, J.W., Peterson, B.J., Shiklomanov, I.A., Shiklomanov, A.I., Zhulidov, A. V., Gordeev, V. V., Bobrovitskaya, N.N., 2002. A circumpolar perspective on fluvial sediment flux to the Arctic ocean. *Global Biogeochem. Cycles* 16. <https://doi.org/10.1029/2001GB001849>
- Hugelius, G., Strauss, J., Zubrzycki, S., Harden, J.W., Schuur, E.A.G., Ping, C., Schirmer, L., 2014. Estimated stocks of circumpolar permafrost carbon with quantified uncertainty ranges and identified data gaps. *Biogeoscience* 11, 6573–6593. <https://doi.org/10.5194/bg-11-6573-2014>
- Hussain, I., Ahamad, K., Nath, P., 2016. Water turbidity sensing using a smartphone. *RSC Adv.* 6, 22374–22382. <https://doi.org/10.1039/C6RA02483A>
- IPCC, 2021. *Climate Change 2021: The Physical Science Basis. Contribution of Working Group I to the Sixth Assessment Report of the Intergovernmental Panel on Climate Change.* Cambridge University Press. <https://doi.org/10.3724/sp.j.7103161536>
- IPCC, 2013. *Climate change 2013, The Physical Science Basis. Contribution of Working Group I to the Fifth Assessment Report of the Intergovernmental Panel on Climate Change.* Cambridge, UK and New York, NY, USA.
- Jafar-Sidik, M., Gohin, F., Bowers, D., Howarth, J., Hull, T., 2017. The relationship between suspended particulate matter and turbidity at a mooring station in a coastal environment: consequences for satellite-derived products. *Oceanologia* 59, 365–378. <https://doi.org/10.1016/j.oceano.2017.04.003>
- Jain, S.K., Singh, V.P., 2003. Emerging techniques for data acquisition and systems modeling, in: Jain, S.K., Singh, V.P. (Eds.), *Developments in Water Science - Water Resources Systems Planning and Management.* Elsevier, Amsterdam, The Netherlands, pp. 123–205. [https://doi.org/https://doi.org/10.1016/S0167-5648\(03\)80057-6](https://doi.org/https://doi.org/10.1016/S0167-5648(03)80057-6)
- Jones, B.M., Arp, C.D., Jorgenson, M.T., Hinkel, K.M., Schmutz, J.A., Flint, P.L., 2009. Increase in the rate and uniformity of coastline erosion in Arctic Alaska. *Geophys. Res. Lett.* 36, 1–5. <https://doi.org/10.1029/2008GL036205>
- Jones, B.M., Farquharson, L.M., Baughman, C.A., Buzard, R.M., Arp, C., Grosse, G., Bull, D.L., Guenther, F., Nitze, I., Urban, F.E., Kasper, J., Frederick, J., Thomas, M., Jones, C., Mota, A., Dallimore, S., Tweedie, C.E., Maio, C., Mann, D.H., Richmond, B., Gibs, A., Xiao, M., Sachs, T., Iwahana, G., Kanevskiy, M., Romanovsky, V., 2018. A decade of remotely sensed observations highlight complex processes linked to coastal permafrost bluff erosion in the Arctic. *Environ. Res. Lett.* 13. <https://doi.org/10.1088/1748-9326/aae471>
- Jong, D., Bröder, L., Tanski, G., Fritz, M., Lantuit, H., Tesi, T., Haghpor, N., Eglinton, T.I., Vonk, J.E., 2020. Nearshore zone dynamics determine pathway of organic carbon from eroding permafrost coasts. *Geophys. Res. Lett.* 47. <https://doi.org/10.1029/2020GL088561>
- Klein, K.P., Lantuit, H., Heim, B., Doxaran, D., Juhls, B., Nitze, I., Walch, D., Poste, A., Søreide, J.E., 2021. The Arctic Nearshore Turbidity Algorithm (ANTA) - A multi sensor turbidity algorithm for Arctic nearshore environments. *Sci. Remote Sens.* 4.

<https://doi.org/10.1016/j.srs.2021.100036>

- Klein, K.P., Lantuit, H., Heim, B., Fell, F., Doxaran, D., Irrgang, A.M., 2019. Long-term high-resolution sediment and sea surface temperature spatial patterns in Arctic nearshore waters retrieved using 30-year Landsat archive imagery. *Remote Sens.* 11. <https://doi.org/10.3390/rs11232791>
- Knaeps, E., Ruddick, K.G., Doxaran, D., Dogliotti, A.I., Nechad, B., Raymaekers, D., Sterckx, S., 2015. A SWIR based algorithm to retrieve total suspended matter in extremely turbid waters. *Remote Sens. Environ.* 168, 66–79. <https://doi.org/10.1016/j.rse.2015.06.022>
- Kulikov, M.E., Medvedev, I.P., Kondrin, A.T., 2018. Seasonal variability of tides in the Arctic Seas. *Russ. J. Earth Sci.* 18, 1–14. <https://doi.org/10.2205/2018ES000633>
- Lantuit, H., Overduin, P.P., Couture, N., Wetterich, S., Aré, F., Atkinson, D., Brown, J., Cherkashov, G., Drozdov, D., Donald Forbes, L., Graves-Gaylord, A., Grigoriev, M., Hubberten, H.W., Jordan, J., Jorgenson, T., Ødegård, R.S., Ogorodov, S., Pollard, W.H., Rachold, V., Sedenko, S., Solomon, S., Steenhuisen, F., Streletskaia, I., Vasiliev, A., 2012. The Arctic Coastal Dynamics Database: A New Classification Scheme and Statistics on Arctic Permafrost Coastlines. *Estuaries and Coasts* 35, 383–400. <https://doi.org/10.1007/s12237-010-9362-6>
- Lantuit, H., Overduin, P.P., Wetterich, S., 2013. Recent progress regarding permafrost coasts. *Permafr. Periglac. Process.* 24, 120–130. <https://doi.org/10.1002/ppp.1777>
- Lantuit, H., Pollard, W.H., 2008. Fifty years of coastal erosion and retrogressive thaw slump activity on Herschel Island, southern Beaufort Sea, Yukon Territory, Canada. *Geomorphology* 95, 84–102. <https://doi.org/10.1016/j.geomorph.2006.07.040>
- Lim, M., Whalen, D., J. Mann, P., Fraser, P., Berry, H.B., Irish, C., Cockney, K., Woodward, J., 2020. Effective monitoring of permafrost coast erosion: wide-scale storm impacts on outer islands in the Mackenzie delta area. *Front. Earth Sci.* 8, 1–17. <https://doi.org/10.3389/feart.2020.561322>
- Loisel, H., Vantrepotte, V., Jamet, C., Ngoc Dat, D., 2013. Challenges and New Advances in Ocean Color Remote Sensing of Coastal Waters, in: Zambianchi, E. (Ed.), *Topics in Oceanography*. IntechOpen, London, UK. <https://doi.org/10.5772/56414>
- Macdonald, R.W., ZouZou, K., Johannessen, S.C., 2015. The vulnerability of arctic shelf sediments to climate change. *Environ. Rev.* 23, 461–479. <https://doi.org/10.1139/er-2015-0040>
- MacFarlane, N., Robinson, I.S., 1984. Atmospheric correction of Landsat MSS data for a multiband suspended sediment algorithm. *Int. J. Remote Sens.* 5, 561–576. <https://doi.org/10.1080/01431168408948837>
- Mackay, J.R., 1971. The Origin of Massive Icy Beds in Permafrost, Western Arctic Coast, Canada. *Can. J. Earth Sci.* 8, 397–422.
- Mangan, S., Lohrer, A.M., Thrush, S.F., Pilditch, C.A., 2020. Water column turbidity not

- sediment nutrient enrichment moderates microphytobenthic primary production. *J. Mar. Sci. Eng.* 8. <https://doi.org/10.3390/JMSE8100732>
- Manzo, C., Braga, F., Zaggia, L., Brando, V.E., Giardino, C., Bresciani, M., Bassani, C., 2018. Spatio-temporal analysis of prodelta dynamics by means of new satellite generation: the case of Po river by Landsat-8 data. *Int. J. Appl. Earth Obs. Geoinf.* 66, 210–225. <https://doi.org/10.1016/j.jag.2017.11.012>
- Masek, J.G., Vermote, E.F., Saleous, N.E., Wolfe, R., Hall, F.G., Huemmrich, K.F., Gao, F., Kutler, J., Lim, T.K., 2006. A landsat surface reflectance dataset for North America, 1990–2000. *IEEE Geosci. Remote Sens. Lett.* 3, 68–72. <https://doi.org/10.1109/LGRS.2005.857030>
- McClelland, J.W., Déry, S.J., Peterson, B.J., Holmes, R.M., Wood, E.F., 2006. A pan-arctic evaluation of changes in river discharge during the latter half of the 20th century. *Geophys. Res. Lett.* 33, 2–5. <https://doi.org/10.1029/2006GL025753>
- McClelland, J.W., Holmes, R.M., Peterson, B.J., Raymond, P.A., Striegl, R.G., Zhulidov, A. V., Zimov, S.A., Zimov, N., Tank, S.E., Spencer, R.G.M., Staples, R., Gurtovays, T.Y., Griffin, C.G., 2016. Particulate organic carbon and nitrogen export from major Arctic rivers. *Global Biogeochem. Cycles* 30, 629–643. <https://doi.org/10.1111/1462-2920.13280>
- McGillivray, D.G., Agnew, T.A., McKay, G.A., Pilkington, G.R., Hill, M.C., 1993. Impacts of climatic change on the Beaufort sea-ice regime: implications for the Arctic petroleum industry, in: *Climate Change Digest CCD*, Vol. 93-01. Environment Canada, Downsview, Ontario.
- Mobley, C.D., 1999. Estimation of the remote-sensing reflectance from above-surface measurements. *Appl. Opt.* 38. <https://doi.org/10.1364/AO.38.007442>
- Mulligan, R.P., Perrie, W., Solomon, S., 2010. Dynamics of the Mackenzie River plume on the inner Beaufort shelf during an open water period in summer. *Estuar. Coast. Shelf Sci.* 89, 214–220. <https://doi.org/10.1016/j.ecss.2010.06.010>
- Munday, J.C., Alföldi, T.T., 1979. Landsat test of diffuse reflectance models for aquatic suspended solids measurement. *Remote Sens. Environ.* 8, 169–183. [https://doi.org/10.1016/0034-4257\(79\)90015-4](https://doi.org/10.1016/0034-4257(79)90015-4)
- Nechad, B., Dogliotti, A.I., Ruddick, K.G., Doxaran, D., 2016. Particulate backscattering and suspended matter concentration retrieval from remote-sensed turbidity in various coastal and riverine turbid waters, in: Ouweland, L. (Ed.), *Proceedings of ESA Living Planet Symposium*, Prague, May 9-13. ESA Communications.
- Nechad, B., Ruddick, K.G., Neukermans, G., 2009. Calibration and validation of a generic multisensor algorithm for mapping of turbidity in coastal waters, in: Bostater, C.R.J., Mertikas, S.P., Neyt, X., Velez-Reyes, M. (Eds.), *Proceedings of SPIE - The International Society for Optical Engineering*. pp. 1–11. <https://doi.org/10.1117/12.830700>
- Neukermans, G., Loisel, H., Me, X., Astoreca, R., Mckee, D., 2012. In situ variability of mass-specific beam attenuation and backscattering of marine particles with respect to particle

size , density , and composition. *Limnol. Oceanogr.* 57, 124–144.
<https://doi.org/10.4319/lo.2011.57.1.0124>

- Nielsen, D.M., Dobrynin, M., Baehr, J., Razumov, S., Grigoriev, M., 2020. Coastal erosion variability at the southern Laptev Sea linked to winter sea ice and the Arctic oscillation. *Geophys. Res. Lett.* 47, 1–11. <https://doi.org/10.1029/2019GL086876>
- Novoa, S., Doxaran, D., Ody, A., Vanhellefont, Q., Lafon, V., Lubac, B., Gernez, P., 2017. Atmospheric Corrections and Multi-Conditional Algorithm for Multi-Sensor Remote Sensing of Suspended Particulate Matter in Low-to-High Turbidity Levels Coastal Waters. *Remote Sens.* 9. <https://doi.org/10.3390/rs9010061>
- Nowak, A., Hodgkins, R., Nikulina, A., Osuch, M., Wawrzyniak, T., Kavan, J., Majerska, M., Romashova, K., Vasilevich, I., Sobota, I., Rachlewicz, G., Kingdom, U., Republic, C., Management, S., 2019. From land to fjords: The review of Svalbard hydrology from 1970 to 2019 (SvalHydro). Svalbard Integrated Arctic Earth Observing System, Svalbard Integrated Arctic Earth Observing System. Longyearbyen, Svalbard. <https://doi.org/https://doi.org/10.5281/zenodo.4294063> 176
- O'Brien, M.C., Macdonald, R.W., Melling, H., Iseki, K., 2006. Particle fluxes and geochemistry on the Canadian Beaufort Shelf: Implications for sediment transport and deposition. *Cont. Shelf Res.* 26, 41–81. <https://doi.org/10.1016/j.csr.2005.09.007>
- Obu, J., Lantuit, H., Fritz, M., Pollard, W.H., Sachs, T., Günther, F., 2016. Relation between planimetric and volumetric measurements of permafrost coast erosion: A case study from Herschel Island, western Canadian Arctic. *Polar Res.* 35, 1–13. <https://doi.org/10.3402/polar.v35.30313>
- Obu, J., Westermann, S., Bartsch, A., Berdnikov, N., Christiansen, H.H., Dashtseren, A., Delaloye, R., Elberling, B., Etzelmüller, B., Kholodov, A., Khomutov, A., Kääh, A., Leibman, M.O., Lewkowicz, A.G., Panda, S.K., Romanovsky, V., Way, R.G., Westergaard-Nielsen, A., Wu, T., Yamkhin, J., Zou, D., 2019. Northern Hemisphere permafrost map based on TTOP modelling for 2000–2016 at 1 km² scale. *Earth-Science Rev.* 193, 299–316. <https://doi.org/10.1016/j.earscirev.2019.04.023>
- Pahlevan, N., Mangin, A., Balasubramanian, S. V., Smith, B., Alikas, K., Arai, K., Barbosa, C., Bélanger, S., Binding, C., Bresciani, M., Giardino, C., Gurlin, D., Fan, Y., Harmel, T., Hunter, P., Ishikaza, J., Kratzer, S., Lehmann, M.K., Ligi, M., Ma, R., Martin-Lauzer, F.R., Olmanson, L., Oppelt, N., Pan, Y., Peters, S., Reynaud, N., Sander de Carvalho, L.A., Simis, S., Spyrakos, E., Steinmetz, F., Stelzer, K., Sterckx, S., Tormos, T., Tyler, A., Vanhellefont, Q., Warren, M., 2021. ACIX-Aqua: A global assessment of atmospheric correction methods for Landsat-8 and Sentinel-2 over lakes, rivers, and coastal waters. *Remote Sens. Environ.* 258. <https://doi.org/10.1016/j.rse.2021.112366>
- Pelletier, B.R., Medioli, B.E., 2014. Environmental atlas of the Beaufort Coastlands, Geological Survey of Canada, Open File 7619. <https://doi.org/10.4095/294601>
- Peterson, B.J., McClelland, J., Curry, R., Holmes, R.M., Walsh, J.E., Aagaard, K., 2006. Trajectory shifts in the arctic and subarctic freshwater cycle. *Science* 313, 1061–1066.

<https://doi.org/10.1126/science.1122593>

- Petus, C., Marieu, V., Novoa, S., Chust, G., Bruneau, N., Froidefond, J.M., 2014. Monitoring spatio-temporal variability of the Adour River turbid plume (Bay of Biscay, France) with MODIS 250-m imagery. *Cont. Shelf Res.* 74, 35–49. <https://doi.org/10.1016/j.csr.2013.11.011>
- Pfalz, G., 2017. Lateral transport of sediment and organic matter, derived from coastal erosion, into the nearshore zone of the southern Beaufort Sea, Canada. Technische Universität Dresden. <https://doi.org/hdl:10013/epic.50702.d001>
- Radosavljevic, B., Lantuit, H., Pollard, W., Overduin, P., Couture, N., Sachs, T., Helm, V., Fritz, M., 2015. Erosion and flooding—threats to coastal infrastructure in the Arctic: A case study from Herschel Island, Yukon Territory, Canada. *Estuaries and Coasts* 39, 900–915. <https://doi.org/10.1007/s12237-015-0046-0>
- Renosh, P.R., Doxaran, D., De Keukelaere, L., Gossn, J.I., 2020. Evaluation of atmospheric correction algorithms for sentinel-2-MSI and sentinel-3-OLCI in highly turbid estuarine waters. *Remote Sens.* 12. <https://doi.org/10.3390/RS12081285>
- Riedel, T., 2017. Assessing permafrost erosion in the Canadian Beaufort Sea, Herschel Island – a biomarker approach. Universität Bremen. <https://doi.org/hdl:10013/epic.51376>
- Ritchie, J.C., Cooper, C.M., Schiebe, F.R., 1990. The relationship of MSS and TM digital data with suspended sediments, chlorophyll, and temperature in Moon Lake, Mississippi. *Remote Sens. Environ.* 33, 137–148. [https://doi.org/10.1016/0034-4257\(90\)90039-O](https://doi.org/10.1016/0034-4257(90)90039-O)
- Rolph, R., Overduin, P.P., Ravens, T., Lantuit, H., Langer, M., 2021. ArcticBeach v1.0: A physics-based parameterization of pan-Arctic coastline erosion. *Geosci. Model Dev. Discuss.* 28, 1–26. <https://doi.org/10.5194/gmd-2021-28>
- Romanovsky, V.E., Smith, S.L., Christiansen, H.H., 2010. Permafrost thermal state in the polar northern hemisphere during the international polar year 2007-2009: A synthesis. *Permafr. Periglac. Process.* 21, 106–116. <https://doi.org/10.1002/ppp.689>
- Ruddick, K.G., Cauwer, V. De, Park, Y., Moore, G., 2006. Seaborne measurements of near infrared water-leaving reflectance: The similarity spectrum for turbid waters. *Limnol. Oceanogr.* 51, 1167–1179. <https://doi.org/https://doi.org/10.4319/lo.2006.51.2.1167>
- Sent, G., 2020. Remote sensing for water quality studies : test of suspended particulate matter and turbidity algorithms for Portuguese transitional and inland waters. University of Lisbon.
- Serreze, M.C., Barry, R.G., 2011. Processes and impacts of Arctic amplification: A research synthesis. *Glob. Planet. Change* 77, 85–96. <https://doi.org/10.1016/j.gloplacha.2011.03.004>
- Serreze, M.C., Holland, M.M., Stroeve, J., 2007. Perspectives on the Arctic’s Shrinking Sea-Ice Cover. *Science* 315. <https://doi.org/10.1126/science.1139426>
- Solomon, S.M., 2005. Spatial and temporal variability of shoreline change in the Beaufort-

- Mackenzie region, northwest territories, Canada. *Geo-Marine Lett.* 25, 127–137. <https://doi.org/10.1007/s00367-004-0194-x>
- Stein, R., MacDonald, R.W., 2014. *The Organic Carbon Cycle in the Arctic Ocean*, 1st edition. Springer-Verlag, Berlin, Heidelberg. <https://doi.org/10.1007/978-3-642-18912-8>
- Storey, J., Scaramuzza, P., Schmidt, G., Barsi, J., 2005. Landsat 7 Scan Line Corrector-Off Gap-Filled Product Gap-Filled Product Development Process, in: *Global Priorities in Land Remote Sensing*.
- Tang, S., Larouche, P., Niemi, A., Michel, C., 2013. Regional algorithms for remote-sensing estimates of total suspended matter in the Beaufort Sea. *Int. J. Remote Sens.* 34, 6562–6576. <https://doi.org/10.1080/01431161.2013.804222>
- Tank, S.E., Fellman, J.B., Hood, E., Kritzberg, E.S., 2018. Beyond respiration: Controls on lateral carbon fluxes across the terrestrial-aquatic interface. *Limnol. Oceanogr. Lett.* 3, 76–88. <https://doi.org/10.1002/lo12.10065>
- Tanski, G., Bröder, L., Wagner, D., Knoblauch, C., Lantuit, H., Beer, C., Sachs, T., Fritz, M., Tesi, T., Koch, B.P., Haghypour, N., Eglinton, T.I., Strauss, J., Vonk, J.E., 2021. Permafrost Carbon and CO₂ pathways differ at contrasting coastal erosion sites in the Canadian Arctic. *Front. Earth Sci.* 9, 1–20. <https://doi.org/10.3389/feart.2021.630493>
- Tanski, G., Lantuit, H., Ruttor, S., Knoblauch, C., Radosavljevic, B., Strauss, J., Wolter, J., Irrgang, A.M., Ramage, J., Fritz, M., 2017. Transformation of terrestrial organic matter along thermokarst-affected permafrost coasts in the Arctic. *Sci. Total Environ.* 581–582, 434–447. <https://doi.org/10.1016/j.scitotenv.2016.12.152>
- Tanski, G., Wagner, D., Knoblauch, C., Fritz, M., Sachs, T., Lantuit, H., 2019. Rapid CO₂ release from eroding permafrost in seawater. *Geophys. Res. Lett.* 46. <https://doi.org/10.1029/2019GL084303>
- Terhaar, J., Lauerwald, R., Regnier, P., Gruber, N., Bopp, L., 2021. Around one third of current Arctic Ocean primary production sustained by rivers and coastal erosion. *Nat. Commun.* 12, 1–10. <https://doi.org/10.1038/s41467-020-20470-z>
- Thomson, J., Rogers, W.E., 2014. Swell and sea in the emerging Arctic Ocean. *Geophys. Res. Lett.* 41, 3136–3140. <https://doi.org/10.1002/2014GL059983>
- USGS Earth Explorer [WWW Document], n.d. URL <https://earthexplorer.usgs.gov> (accessed 1.16.19).
- Van Everdingen, R.O., 2005. *Multi-language glossary of permafrost and related ground-ice terms (Rev. ed. 2005)*. Calgary, Canada.
- Van Vliet, M.T.H., Franssen, W.H.P., Yearsley, J.R., Ludwig, F., Haddeland, I., Lettenmaier, D.P., Kabat, P., 2013. Global river discharge and water temperature under climate change. *Glob. Environ. Chang.* 23, 450–464. <https://doi.org/10.1016/j.gloenvcha.2012.11.002>
- Vanhellemont, Q., 2019. Remote sensing of environment adaptation of the dark spectrum fitting atmospheric correction for aquatic applications of the Landsat and Sentinel-2 archives.

- Remote Sens. Environ. 225, 175–192. <https://doi.org/10.1016/j.rse.2019.03.010>
- Vanhellemont, Q., Ruddick, K., 2021. Atmospheric correction of Sentinel-3/OLCI data for mapping of suspended particulate matter and chlorophyll-a concentration in Belgian turbid coastal waters. Remote Sens. Environ. 256, 112284. <https://doi.org/10.1016/j.rse.2021.112284>
- Vanhellemont, Q., Ruddick, K., 2018. Atmospheric correction of metre-scale optical satellite data for inland and coastal water applications. Remote Sens. Environ. 216, 586–597. <https://doi.org/10.1016/j.rse.2018.07.015>
- Vanhellemont, Q., Ruddick, K., 2015. Remote Sensing of Environment Advantages of high quality SWIR bands for ocean colour processing : Examples from Landsat-8. Remote Sens. Environ. 161, 89–106. <https://doi.org/10.1016/j.rse.2015.02.007>
- Vanhellemont, Q., Ruddick, K., 2014. Turbid wakes associated with offshore wind turbines observed with Landsat 8. Remote Sens. Environ. 145, 105–115. <https://doi.org/10.1016/j.rse.2014.01.009>
- Vonk, J.E., Sánchez-García, L., van Dongen, B.E., Alling, V., Kosmach, D., Charkin, A., Semiletov, I.P., Dudarev, O. V., Shakhova, N., Roos, P., Eglinton, T.I., Andersson, A., Gustafsson, Ö., 2012. Activation of old carbon by erosion of coastal and subsea permafrost in Arctic Siberia. Nature 489, 137–140. <https://doi.org/10.1038/nature11392>
- Walch, D.M.R., 2021. Spatio-temporal variability in suspended particulate matter in a high Arctic estuary (Adventfjorden , Svalbard): A combined Field- and Remote Sensing approach. University of Potsdam.
- Walsh, J.E., Fetterer, F., Scott Stewart, J., Chapman, W.L., 2017. A database for depicting Arctic sea ice variations back to 1850. Geogr. Rev. 107, 89–107. <https://doi.org/10.1111/j.1931-0846.2016.12195.x>
- Weege, S., 2016. Climatic drivers of retrogressive thaw slump activity and resulting sediment and carbon release to the nearshore zone of Herschel Island, Yukon Territory, Canada. University of Potsdam.
- Wegner, C., Bennett, K.E., de Vernal, A., Forwick, M., Fritz, M., Heikkilä, M., Łacka, M., Lantuit, H., Laska, M., Moskalik, M., O'Regan, M., Pawłowska, J., Promińska, A., Rachold, V., Vonk, J.E., Werner, K., 2015. Variability in transport of terrigenous material on the shelves and the deep Arctic Ocean during the Holocene. Polar Res. 34, 24964. <https://doi.org/10.3402/polar.v34.24964>
- Węsławski, J.M., Gluchowska, M., Szczucinski, W., Tatarek, A., Wiktor, J., Włodarska-Kowalczyk, M., Zajaczkowski, M., 2011. Adventfjorden: Arctic sea in the backyard, 1st Editio. ed. Institute of Oceanology Polish Academy of Sciences, Sopot, Poland.
- Williams, W.J., Carmack, E.C., Shimada, K., Melling, H., Aagaard, K., Macdonald, R.W., Grant Ingram, R., 2006. Joint effects of wind and ice motion in forcing upwelling in Mackenzie Trough, Beaufort Sea. Cont. Shelf Res. 26, 2352–2366. <https://doi.org/10.1016/j.csr.2006.06.012>

- World Glacier Monitoring Service, 2020. World Glacier Monitoring Database. Zurich, Switzerland. <https://doi.org/10.5904/wgms-fog-2020-08>
- Wukelic, G.E., Gibbons, D.E., Martucci, L.M., Foote, H.P., 1989. Radiometric calibration of Landsat Thematic Mapper thermal band. *Remote Sens. Environ.* 28, 339–347. [https://doi.org/10.1016/0034-4257\(89\)90125-9](https://doi.org/10.1016/0034-4257(89)90125-9)
- Xue, C., Zhang, T., Chen, S., Wu, X., Yan, F., 2019. A novel estimation method for SPM in China eastern coastal waters based on conventional hydrological profile measurements. *Estuar. Coast. Shelf Sci.* 230, 106444. <https://doi.org/10.1016/j.ecss.2019.106444>
- Yang, D., Shi, X., Marsh, P., 2015. Variability and extreme of Mackenzie River daily discharge during 1973-2011. *Quat. Int.* 380–381, 159–168. <https://doi.org/10.1016/j.quaint.2014.09.023>
- Zajaczkowski, M., Włodarska-Kowalczyk, M., 2007. Dynamic sedimentary environments of an Arctic glacier-fed river estuary (Adventfjorden, Svalbard). I. Flux, deposition, and sediment dynamics. *Estuar. Coast. Shelf Sci.* 74, 285–296. <https://doi.org/10.1016/j.ecss.2007.04.015>

DANKSAGUNG

Vor fast fünf Jahren sagte ich, dass ich nach meiner Masterarbeit nicht promovieren wollen würde. Obwohl das damals mein vollkommener Ernst war, würde ich keinen Tag der letzten 3.5 Jahre missen wollen. Bereits während meiner Masterarbeit wurde meine Begeisterung für das wissenschaftliche Arbeiten geweckt, und bis zum heutigen Tage ist sie noch nicht erloschen. Ich bin sehr dankbar für die Möglichkeit, mein eigenes Projekt verwirklicht haben zu können und meine eigenen Ideen entwickelt zu haben, was diese Arbeit viel mehr zu meiner Arbeit gemacht hat als ich es für möglich gehalten hätte. Dies wäre nicht möglich gewesen ohne die finanzielle Unterstützung der Potsdam Graduate School (PoGS), dessen Promotionsstipendium mir all diese Freiheiten gelassen hat.

Obwohl auf dem Deckblatt dieser Arbeit nur mein Name steht, waren doch sehr viel mehr Personen daran beteiligt. Dies umfasst alle Bereiche, die man sich nur vorstellen kann. Hugues und Biggi haben bereits lange vor dem offiziellen Beginn des Promotionsstipendiums mit mir zusammen dieses Projekt entworfen und den Antrag für dieses Stipendium vorbereitet. Ihr beide habt erheblichen Anteil an dem erfolgreichen Abschluss dieses Projektes. Trotz eines abgeschlossenen Masterstudiums fühlt man sich zu Beginn der Promotion doch als totaler Anfänger in der Welt der Wissenschaft. Eure Hilfe hat dazu geführt, dass ich mich deutlich besser zurechtfinden konnte, und eure Expertise hat die fachliche Ausrichtung dieser Arbeit massiv beeinflusst. Während meiner Zeit in Nizza und Villefranche war David mein wichtigster Ansprechpartner. Du hast dafür gesorgt, dass diese fünf Monate wissenschaftlich ein voller Erfolg wurden. Doch auch persönlich möchte ich diese Zeit nicht missen, und die gesammelten Erfahrungen sind für mich unersetzlich. Und das tolle Wetter habe ich natürlich auch genossen.

Ich habe das Arbeiten am AWI in Potsdam immer genossen, vom ersten Tag im Januar 2017 an, als ich das Büro zum ersten Mal betrat. Jeder meiner aktuellen und früheren Kollegen hat seinen Anteil daran. Ihr konntet mir helfen, wenn ich alleine nicht weiterkam. Ihr habt mich abgelenkt, wenn mein Kopf kurz vorm platzen war. Ihr habt mich zum Mittag essen begleitet und mit mir zusammen Kaffee getrunken. Ihr habt die drei Expeditionen, an denen ich

teilgenommen habe, zu den verrücktesten Ereignissen meines bisherigen Lebens gemacht, und ich werde noch Jahrzehnte lang davon schwärmen.

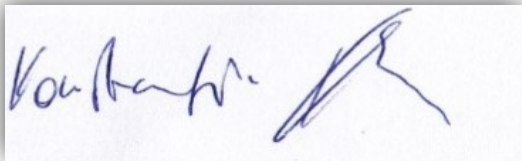
Ohne private Unterstützung wäre es meiner Meinung nach nicht möglich, solch eine Arbeit über diesen langen Zeitraum zu schreiben. Jedes einzelne Mitglied meiner Familie oder meines Freundeskreises hat mir über fast vier Jahre allen nur erdenklichen Beistand zukommen lassen. Ihr habt mich bekräftigt, egal wie ungewöhnlich meine Entscheidungen der letzten Jahre auch gewesen sein möchten. Ich konnte mich stets auf jeden von euch verlassen. Jedes Gespräch, wie belanglos es auch gewesen sein mochte, hat sich mit euch so viel bedeutender angefühlt. Jedes Bier, das ich in eurer Gesellschaft getrunken habe, war mir ein besonderer Genuss.

Anne. Keines der Worte, das ich hier niederschreiben könnte, würde auch nur ansatzweise ausdrücken, was du für mich bedeutest. Du hast es geschafft mir stets den Rücken freizuhalten, und ohne dich würde es keines der über 30 000 Wörter dieser Arbeit geben. Mein gesamtes Leben ergibt durch dich so viel mehr Sinn, und ich kann nur hoffen, dass sich das nie ändern wird.

Für mich endet nun ein Abschnitt meines Lebens, der mich geprägt hat wie wohl kein anderer seit meiner Kindheit. Jeder von euch hat seinen Anteil an meinem Werdegang, sei es beruflich oder privat. Auch wenn ich noch nicht weiß, wohin es mich in Zukunft verschlagen wird, hoffe ich doch weiterhin mit möglichst vielen von euch so schöne Erinnerungen teilen zu können.

EIDESSTATTLICHE ERKLÄRUNG

Hiermit versichere ich, dass ich die vorliegende Arbeit selbstständig verfasst und keine anderen als die angegebenen Quellen und Hilfsmittel verwendet habe. Ich habe diese kumulative Dissertation am Alfred-Wegener-Institut Helmholtz Zentrum für Polar und Meeresforschung in Potsdam erarbeitet und in englischer Sprache angefertigt. Diese Dissertation wird erstmalig und ausschließlich an der Universität Potsdam eingereicht. Die dem Promotionsverfahren zugrundeliegende Promotionsordnung vom 18.09.2013 ist mir bekannt.

A rectangular box containing a handwritten signature in blue ink. The signature appears to be 'Konstantin P. Klein' followed by a stylized flourish.

Konstantin P. Klein